Lucas Atila Bernardes Marçal

Retrieving chemical and structural properties of nanomaterials through synchrotron x-ray diffraction techniques

Tese apresentada ao Programa de Pós-Graduação em Física do Instituto de Ciências Exatas da Universidade Federal de Minas Gerais como requisito parcial para obtenção do título de Doutor em Ciências

Supervisor: Prof. Ângelo Malachias de Souza (UFMG)

Co-supervisor: Profª. Marie-Ingrid Richard (ESRF – Grenoble)

Belo Horizonte

2018

Dedico este trabalho à minha mãe.

Acknowledgements/Agradecimentos

Ao meu amigo professor Ângelo Malachias, que salvou uma alma que estava completamente perdida durante a graduação. Muito obrigado por apontar o caminho e me dar a oprtunidade de ser alguém na vida.

To Dr. Marie-Ingrid Richard and Dr. Tobias Schülli, for receiving me at the ESRF and helping me growing up as a scientist.

To all my collaborators: Prof. Rogério Paniago, Prof. Mario Mazzoni, Prof. Euclydes Marega, Dr. Christoph Deneke, Prof. Letícia Coelho, Dr. Gregory Salamo, Dr. Lucca Persichetti, Dr. Anna Sgarlata, Dr. H. Renevier, Dr. M. Fanfoni, Dra. Bárbara Rosa, Dr. Jèrome Carnis and Prof. Tomas Cornelius.

A todos os amigos do laboratório, os quais tiveram o prazer de me conhec... digo, os quais eu tive o prazer de conhecer: Prof. Gustavo Sáfar (Francisco Lemos), Ingrid, Muriel, Alejandro, Paula, Thaís, Lorena, Pedro, Éverton, Gilberto, Luan, Vitória e Eduardo.

To the ID01 staff, for supporting me during my stay in Grenoble: Gaitan Girard, Edoardo Zatterin, Prof. Paul Evans, Dr. Steven Leake, Peter Boesecke, Hamid Djazouli, Dr. Carsten Richter and Dr. Tao Zhao.

Ao Yuri, por me mostar como é possível levar a vida com bom humor, mesmo com um irmão burro.

À minha mãe e ao meu pai, porque sem vocês eu não teria forças pra me levantar nos dias difíceis.

Às minhas madrinhas Elma, Nilza e Inácia, que achavam que eu tinha cara de doutor quando eu ainda tinha cara de cliente da Pampers.

Aos meus amigos Egleidson Frederik e Carlos Gonçalves, que me ajudam a rir das minhas próprias desventuras.

Aos meus padrinhos Patrícia e Cássio, pelos bons conselhos e por todos os desejos de sucesso.

Às instituições que financiaram minhas pesquisas: UFMG, LNLS, ESRF, CNPq, CAPES e FAPEMIG.

Abstract

This thesis presents a study about crystalline semiconductor nanostructures using x-ray diffraction techniques, mainly resonant (anomalous) x-ray diffraction, in order to determine structural and chemical properties of these structures. Our first experimental result is a study about In(Mn)As islands grown under controlled Mn flux on the top of GaAs(001) substrates. Adding distinct amounts of Mn on the growth process makes the In(Mn)As islands allocate the metallic atoms in different sites, which can be substitutional or interstitial. Performing x-ray diffraction measurements on these nanostructures, using photons with energy near the Mn-K absorption edge, it is possible to verify quantitatively their chemical concentration, and also which site is being occupied. Each possible site has its own signature on different reflections and, with the right choice of reflections, one can determine, unambiguously, the percentage of occupied sites. The second study applies resonant x-ray diffraction on nanostructures of Ge grown on Si (substrate) with different *miscut* angles with respect to the (001) direction. It is well known from the literature that Ge can grown on Si as domes or superdomes, depending on the amount of Ge content. It is also known that a miscut angle can affect the growth dynamics, as it changes the internal composition of the structures. The quantitative study of the domes/superdomes composition carried out there connects its chemical properties with the effects observed by x-ray diffraction due to the miscut. Finally, we also present a study of InGaAs islands on top of an ultrathin GaAs(001) membrane. Nano-focused x-ray diffraction measurements allows the determination of the strain status on isolated islands, helping to understand the structural changes on the membrane after releasing it from the substrate where it was originally grown.

Resumo

Esta tese apresenta um estudo sobre nanoestruturas cristalinas semicondutoras utilizando técnicas de difração de raios-X, principalmente difração ressonante (anômala) de raios-X, para determinar as propriedades estruturais e químicas de tais estruturas. Nosso primeiro resultado experimental apresenta um estudo de ilhas de In(Mn)As crescidas sob fluxo controlado de Mn, no topo de substratos de GaAs(001). Adicionar quantidades distintas de Mn no processo de crescimento faz com que as ilhas de In(Mn)As aloquem os átomos metálicos em diferentes sítios, que podem ser substitucionais ou intersticiais. Realizando medidas de difração de raios-X nestas nanoestruturas, utilizando fótons com energia em torno da borda de absorção K do Mn, é possível verificar quantitativamente sua concentração química, e também determinar o sítio que está sendo preenchido. Cada possível sítio tem sua própria assinatura em diferentes reflexões e, com a escolha correta das reflexões, pode-se determinar, de forma não ambígua, a porcentagem dos sítios ocupados. O segundo estudo aplica difração ressonante de raios-X em nanoestruturas de Ge crescido em Si (substrato), com diferentes ângulos de *misuct* em relação à direção(001). É bem conhecido da literatura que Ge pode crescer em Si como domos ou superdomos, dependendo da quantidade de Ge utilizado. Sabe-se também que um ângulo de *miscut* pode afetar a dinâmica de crescimento, pois altera a composição interna das estruturas. O estudo quantitativo da composição de domos/superdomos realizados relacionam suas propriedades químicas com os efeitos observados pela difração de raios-X em função do *miscut*. Finalmente, também apresentamos um estudo sobre ilhas de InGaAs em cima de uma membrana de GaAs(001) ultrafina. Medidas de difração de raios-X com nano-foco permitem a determinação do estado de tensão em ilhas isoladas, ajudando a entender as mudanças estruturais na membrana após liberá-la do substrato onde foi crescida.

Index

Resume

Abstract

Introduction

Semiconductor materials have attracted a great interest from the scientific community and from industry in the last few decades, all due to their properties and potential for important innovations in devices and nanotechnology. Semiconductors doped with atoms that present magnetic properties have particularly interesting physical properties, which can be of great value for applications in optoelectronic and spintronic-based components. Much effort has been made to combine electronic charge and spin degree of freedom in a single magnetoelectronic device. In particular, nanostructures of InAs and GaAs doped Mn are strong candidates to play a substantial role in these next generation of devices.

Additionaly, to control optoelectronic properties due to elastic tensor constraints in semiconductor nanostructures also plays an important role for modern nanoscale engineering. The study of islands grown on substrates with miscut can help on the understanding of surface configurations and energies of the vastly studied heteroepitaxial growth of Ge on vicinal Si(001). Finally, but not less important, nanomembranes based on semiconductor materials with quantum dots are strong candidates to be used on flexible nanodevices. The possibility to transfer a nanometer thick membrane to a new support opened up substantial potential applications in flexible electronics.

This thesis shows how X-ray diffraction techniques can be used to determine important physical and chemical properties of semiconductor nanostructures.

Chapter 1

Semiconductor nanostructures

1.1 Epitaxy and strain

A film or nanostructure is said to be epitaxial if its atoms are able to grow with certain periodic organization dictated by the atoms of the substrate (also crystalline) in which it is deposited. For a given direction, after each spacing **a**, that will be called from now on as the lattice parameter, a repetition in the position of the atoms can be noticed. When this pattern repeats throughout all the epitaxially deposited layer, it is said to be monocrystalline. The positions of each atom in these repeating intervals define the unit cell, which can be characterized by a structure factor, discussed in more details in chapter 2. Sometimes the lattice parameter of a given material is the same for all three directions in the space, and its lattice is said to be cubic, a condition found on all materials studied in this work.

A monocrystalline material can also grow over another one with different lattice parameter. The material that is being grown must then adjust its lattice with the substrate, since epitaxial crystalline materials tend to match their lattice parameters at the interface. Such procedure results in a biaxial in-plane strain on the interface, which will be responsible to conform the newly deposited layer [1]. In order to preserve the volume of the unit cell, the strained material unit cell can expand or contract in the growth direction, leading to three possible scenarios: (a) If the deposited material has a lattice parameter that is equal to the substrate, no strain occurs; (b) If the deposited material has a lattice parameter greater than the substrate, it will contract in the in-plane directions (parallel to the interface) and expand in the growth direction; (c) If the deposited material has a lattice parameter smaller than the substrate, it will expand in-plane and contract in the growth direction [2]. The three different possibilities above described will lead to a deposited film without strain, with compressive strain and tensile strain, respectively. The described situations are schematically represented in figure 1.1 in a three-dimensional view (the growth direction is vertical for this figure).

The deformation that occurs in cases (b) and (c) (different lattice parameters) will lead to elastic energy storage in the film. After a certain amount of deposited material, known as critical thickness, the film can no longer store all the elastic energy by straining its lattice parameter during the growth process, and defects (such as dislocations and stacking errors) might occur. These processes release some elastic energy, generating a new equilibrium state.

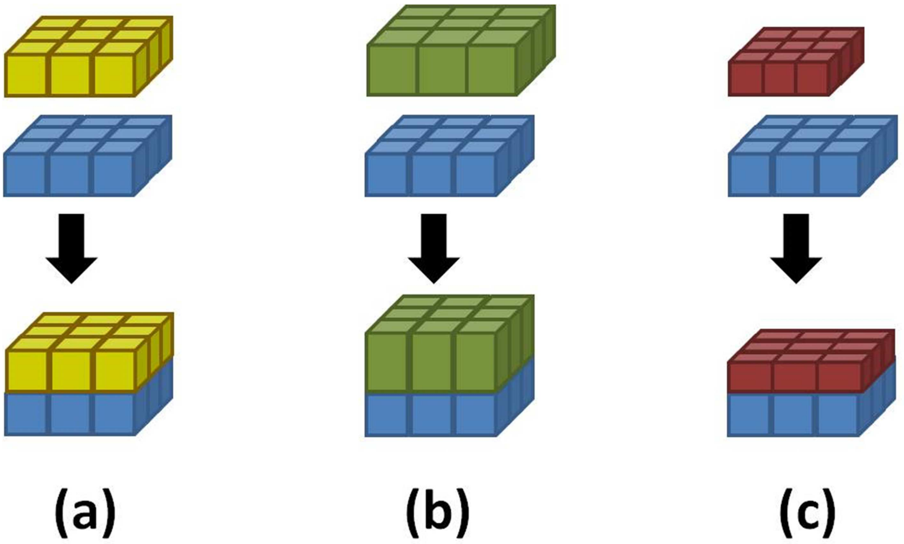

Fig 1.1 - Scheme showing how heteroepitaxial growth of a crystalline layer on a substrate (blue color) can occur: a) same lattice parameter, b) the deposited material has a lattice parameter greater than the substrate, and c) the deposited material has a lattice parameter smaller than the substrate.

In Figure 1.2 we show a relaxed InAs island that presents defects. The image was obtained using transmission electron microscopy [3].

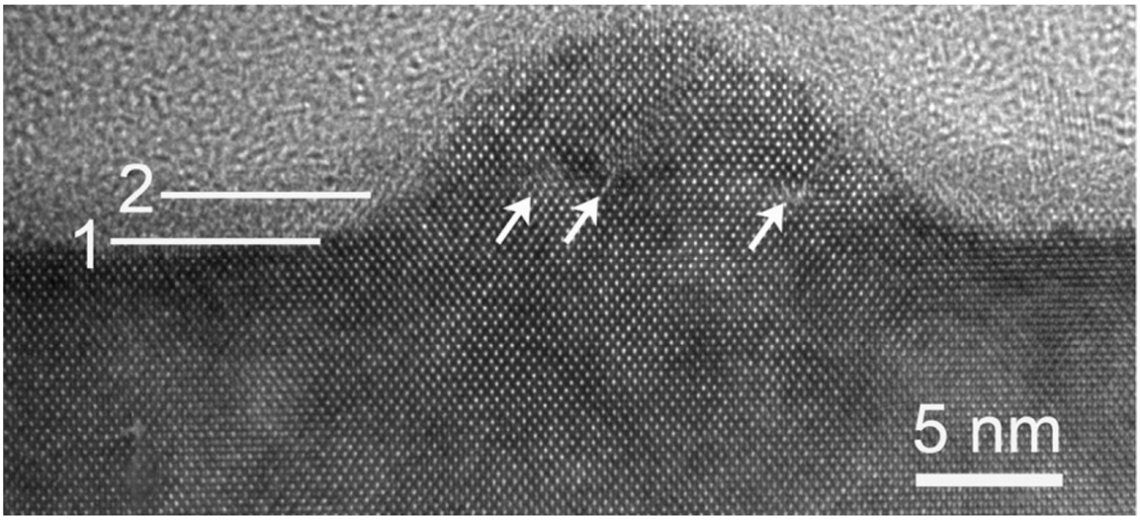

Fig 1.2 - Image of an InAs island with defects, grown on GaAs. The image was obtained using transmission electron microscopy [3]. Lines 1 and 2 indicate, respectively, the crystalline surface of the substrate and the layer of amorphous material on the top. The lattice misalignment positions are indicated by arrows.

1.2 Techniques for epitaxial growth

Many of the interesting phenomena for the semiconductor industry occurs at the surface, therefore it is of considerable importance to develop methods of growth of epitaxial layers of thin films and nanostructures with composition and thickness control [1]. Thus, deposition techniques such as molecular beam epitaxy (MBE) and vapor deposition via metal organic chemical vapor deposition (MOCVD) have gained great interest in the last decades.

MBE is known as the method for epitaxial growth, in ultra-high vacuum (UHV), that produces the sharpest interfaces, resulting from the condensation of molecules or atom beams directed to the substrate [4]. The beams are created by effusion cells maintained at well defined temperatures, which results on known vapor pressures. The deposition on the substrate may occur near or out of the thermal equilibrium [5], being an almost purely kinetic process (with adsorption and migration of atoms at surface sites) [4]. For best results with this technique, it is crucial to have a reliable UHV system to avoid impurities during the growth process. It is also desirable the presence of a mass spectrometer in order to monitor the flow of the vapors and the environment in which the film is being grown. Compared with other techniques, MBE is generally characterized by the low growth rate at medium temperatures (400 ° C - 600 ° C) and the possibility to generate abrupt interfaces (the interruption of the molecular beam stops the process). The fact that the growth rate is low allows a better control of the thickness of the structure being grown, while the reduced temperature in relation to other methods minimizes any undesired process, such as the diffusion of material through interfaces. In addition, since the constituents reach the substrate from different beams, and it is possible to control (with a great precision) the concentration of each one.

The MOCVD, process also known as organometallic chemical vapor deposition (OMCVD), metalorganic vapor phase epitaxy (MOVPE) and organometallic vapor phase epitaxy (OMVPE), is the thin film growth technique that, together with MBE, has been dominant for research, development and fabrication of devices based on semiconductor components since the early 1980s [6]. The MOCVD reactors are basically constituted by three components: a system to conduct the reactive gases, a reaction chamber and a security chamber. The reagent conduction system is an extremely clean set of tubes that connect the chambers where the reactant gases are stored to the reaction chamber. The reaction chamber is the place where the gases are mixed and conducted to a heated region, where chemical reactions occur, allowing the deposition of films on the substrate. The presence of a safety chamber is necessary, since the use of toxic gases in the MOCVD reactions is very common. It allows the manipulation of the substrate/sample in a safe environment moments before and after the deposition reactions [6]. It is clear how advantageous the use of MBE may be for the growth of nanostructures with abrupt changes in composition and/or doping. On the other hand, MOCVD growth has great industrial appeal, since it can work in large scale (larger deposition surface area and reproducibility) due to the reduced need for a vacuum system and the control of the volume of reagents in the deposition chamber.

In general, to monitor the crystalline quality of the surface of the film that is grown in high vacuum, the high-energy electron diffraction (RHEED) is used. This technique basically consists on focusing an electronic beam on the surface of the growing sample with a grazing incident angle θ. Some of these electrons will be diffracted by the surface of the sample (due to the charge of the electrons and the low angle of incidence, the penetration power is restricted to few atomic layers). A window covered with a phosphoric film is then used to convert the diffracted electrons into light signals, and this luminous diffraction pattern provides information about the quality of the sample surface [6].

Figure 1.3 shows a schematic representation of a MBE growth chamber. It is possible to observe the effusion cells, each with a different atomic species. The beams coming out of these cells go directly to the substrate, which is in a heated support, allowing the control of the growth temperature of the film being deposited. The electron gun and the phosphoric window, monitored by a CCD, are also represented.

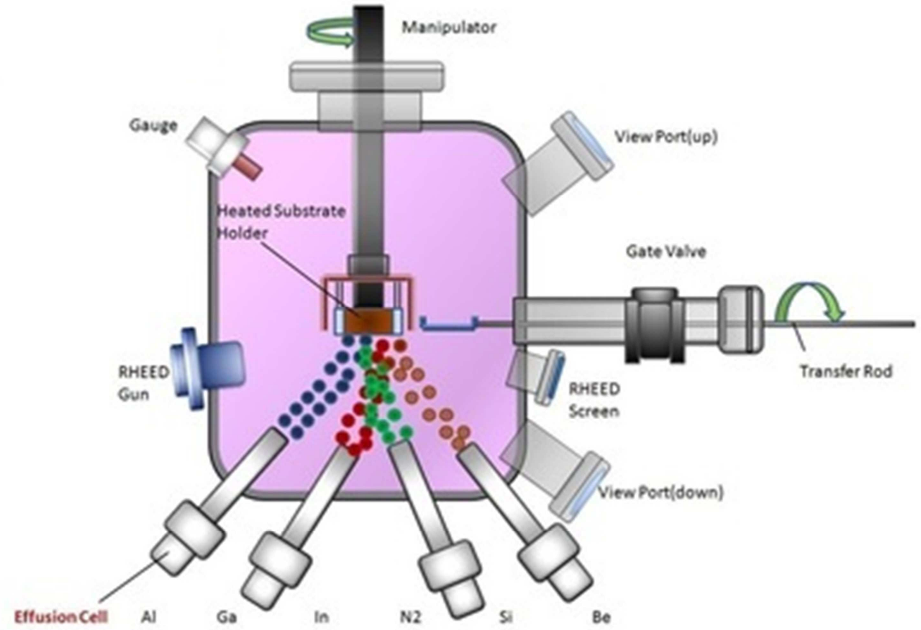

Fig 1.3 – Schematic representation of a Molecular Beam Epitaxy growth chamber.

In the figure 1.4 it is possible to observe, in a more detailed scheme, the monitoring system that is generally used in the MBE chambers, the RHEED. One observes that some of the electrons coming out of the electron gun are diffracted, reaching the window covered with phosphor and its light is picked up by the detector/CCD at different points, giving information about the structure of the first layers of the material being grown.

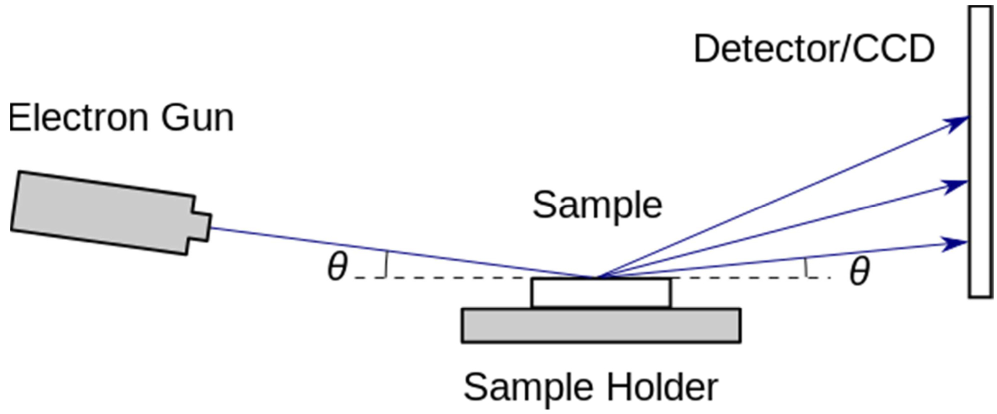

Fig 1.4 – Schematic representation of the technique generally used to control the quality of the films grown by MBE, the RHEED.

In figure 1.5 one can see a schematic representation of a MOCVD reactor, where the gases leave their storage chambers, pass through the conduction system and enter the reaction chamber. Some of the reaction products are discarded into the atmosphere, and the substrate with the freshly grown film goes to the security chamber, at controlled pressure.

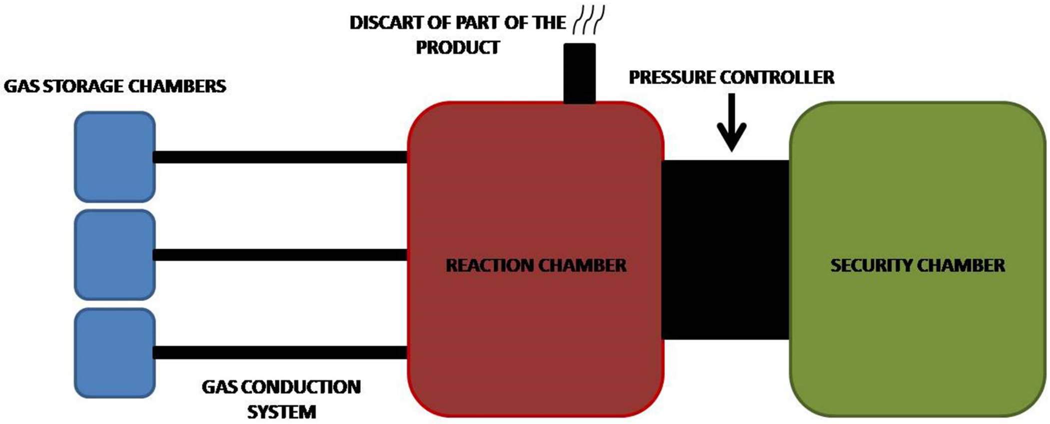

Fig 1.5 – Schematic representation of a MOCVD growth system.

1.3 Epitaxial growth modes

In the processes of heteroepitaxial films growth, some physical properties of the materials involved are relevant to determine how the growth process will take place at the interface. In addition to the lattice parameter, which is the most relevant structural characteristic, it is indispensable to also consider some factors such the chemical affinity between the materials in order to understand the morphological evolution of the growing layers.

One can describe three different modes that may occur during the heteroepitaxial deposition [7]. In the first mode, named **Frank-van der Merve**, the material grows layer by layer, i.e. a new layer will only start to grow when the bottom is fully filled. In this mode the interaction between the substrate material and the new layer of atoms is energetically advantageous when compared with the interaction between the atoms of the layer itself (considering the growth of the first layer). In the second mode, **Volmer-Weber**, the interaction between the neighboring atoms of the deposited material is energetically favorable if compared to the interaction with the atoms from the substrate. In this case the atoms tend to agglomerate, and the material forms three-dimensional islands. In the intermediate case, named **Stranski-Krastanov**, the deposited material first grows forming layers, up to a certain thickness (critical thickness), and thereafter starts to form islands. What occurs in this scenario is a growth mode in which the deposited materials and the substrate have a reasonable chemical affinity, but a considerable difference on the lattice parameter. Consequently, upon initiating the growth process on layer by layer, the deposited film will store elastic energy due to the elastic deformation at the interface, and that energy will increase proportionally to the layer thickness. After the critical thickness the stored energy in the epitaxial layer can be released by changing the length of the atomic bonds, leading to a lower energy configuration. The result is the formation of three-dimensional islands, where the lattice parameter of the deposited material can approach its bulk value.

One of the factors that can be evaluated to determine the growth mode that will take place is the free surface energy. If σ_f is the free surface energy of the deposited film, σ_s is the free surface energy of the substrate and σ_i is the free surface energy of the interface between them. In this case, if

$$\sigma_f < \sigma_s + \sigma_i \tag{1}$$

the growth will be layer by layer, while if

$$\sigma_s < \sigma_f + \sigma_i \tag{2}$$

Islands will be formed.

In the Stranski-Krastanov mode, equation 1 is true up to the critical thickness, when the surface free energy becomes very large, equation 2 becomes valid and the growth process will start to form islands.

In figure 1.6 it is possible to see a schematic step-by-step representation of the three growth modes for heteroepitaxial materials, previously described.

The growth of self-organized nanostructures by MBE or MOCVD occurs in Stranski-Krastanov mode for some systems (eg InAs:GaAs, Ge:Si, InP:GaAs, and others) and generally leads to the formation of quantum dots presenting great homogeneity in size, which can be used for optoelectronic applications [8, 9].

Recently, the deposition of InAs on top of GaAs have been vastly studied, and the difference on their lattice parameter is about 7% (a_{GaAs} = 5.6532 Å and a_{InAs} = 6.0583 Å). During the InAs growth process, the transition from two-dimensional layers to islands occurs after the deposition of, approximately, 1.5 ~ 1.6 monolayers (MLs). The islands that will be formed after that can be either, coherent or incoherent, transitions that occurs at 2.3 MLs. One might calls coherent the film or nanostructure that keeps a perfect record of the crystalline lattice of the substrate on which it was deposited. In this case, the elastic energy stored is maximum. If the film does not keep a complete record on the substrate, it is said to be incoherent. In incoherent films the elastic energy is reduced due to the appearance of dislocations or defects. Generally, an InAs island grown on GaAs becomes incoherent when its volume is too large and no longer allows the elastically storage of more material.

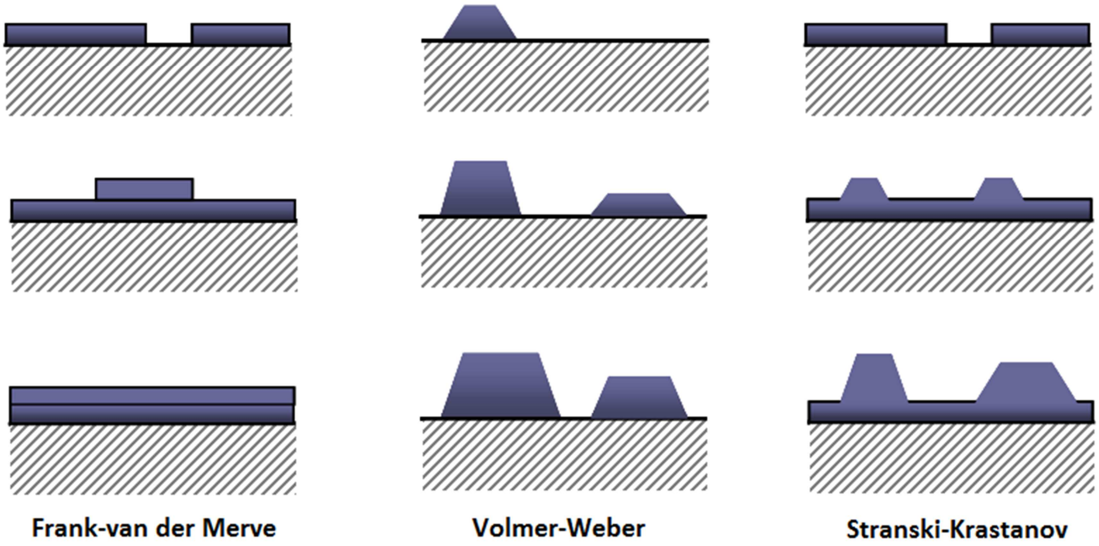

Fig 1.6 – Schematic representation of the three growth modes for heteroepitaxial materials: Frank-van der Merve, Volmer-Weber and Stranski-Krastanov.

Another system vastly studied during the last decades is the Ge deposited on top of Si(001). Both atoms have similar structural and electronic properties: crystallize in the diamond structure and have indirect electronic energy gap. Their lattice parameters are 5.431 Å (Si) and 5.65 Å (Ge), corresponding to a lattice mismatch of 4.2%.

The growth of Ge on Si follows follows the Stranski-Krastanov mode. One can observe three main different stages on the growth process, as shown in fig. 1.7. Ge growth first proceeds in a layer-by-layer mode up to a coverage (Θ) of about 3.5 MLs of Ge. Then, for thicker layers, the elastic strain is released by the formation of small pyramidal shaped islands, which are islands with a low aspect ratio and {105} facets. Finally, when the Ge coverage exceeds approximately 6 MLs (and for a constant growth temperature) a shape transition from pyramids to dome islands occurs [2]. Dome islands are larger in volume (number of atoms) and in height (despite of having essentially the same base radius of pyramids), exhibiting more complex facets when compared to pyramids.

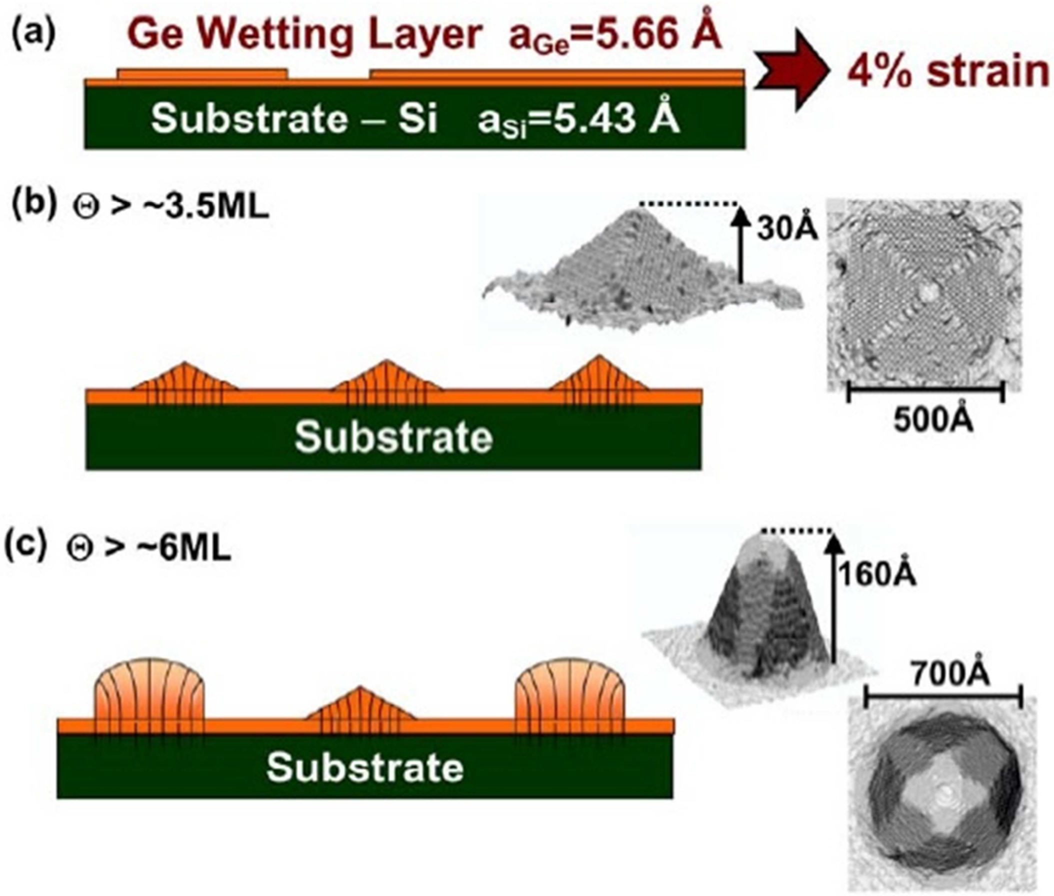

Fig 1.6 – Representation of the steps of Ge growth on Si(001). (a) A wetting layer is formed. (b) Pyramid islands nucleation occurs for coverages Θ > ~3.5 ML. (c) Island shape transition to domes occurs for content Θ > ~6ML. Typical pyramid and dome islands are shown with their dimensions [2].

Chapter 2

X-ray diffraction

2.1 Crystalline structure

In order to start a discussion about X-ray scattering and diffraction, first it is necessary to understand the crystalline structure of the solids that will be studied. When X-ray photons diffract from crystalline planes, we can extract information about the organization of the atoms that form a given crystal.

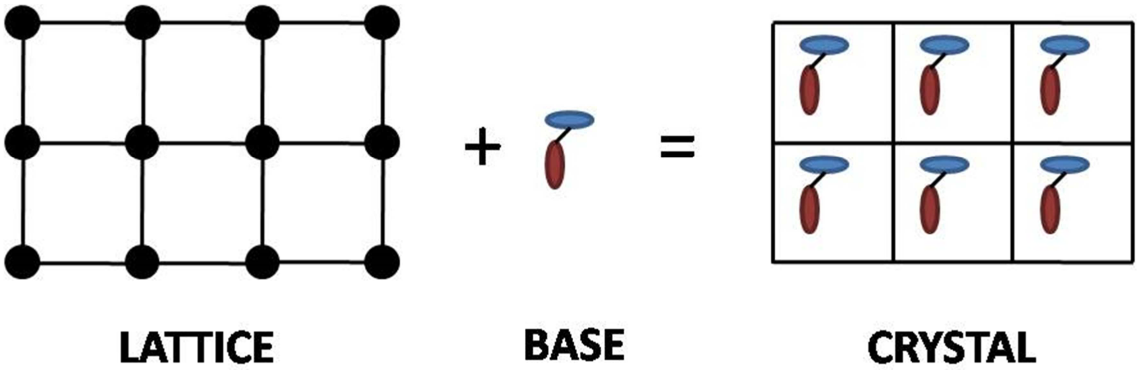

Fig. 2.1 - Schematic representation of a crystal, composed by a lattice (which determines its symmetry) and by a base (which determines the organization of the atoms in each of these units of symmetry).

A crystal is an infinite repetition of a base. One can imagine the base represented by a point, and then the arrangement of these points would be called the Bravais lattice. A lattice can be formed using vectors $\mathbf{a}_1$, $\mathbf{a}_2$ e $\mathbf{a}_3$, for any given position any $\mathbf{r}$ ou $\mathbf{r} + \mathbf{a}_n$, and they will be called the lattice vectors [10]. In addition on how these atoms are distributed along the crystal, other extremely important information is the composition of the base. By knowing the lattice and base, we have information about the structure of the crystal we are studying, as shown in figure 2.1.

Figure 2.2 shows a schematic representation of the 14 possible fundamental lattices, i. e. the 14 ways crystalline materials can be organized by symmetry, as well as the name commonly given to each of them.

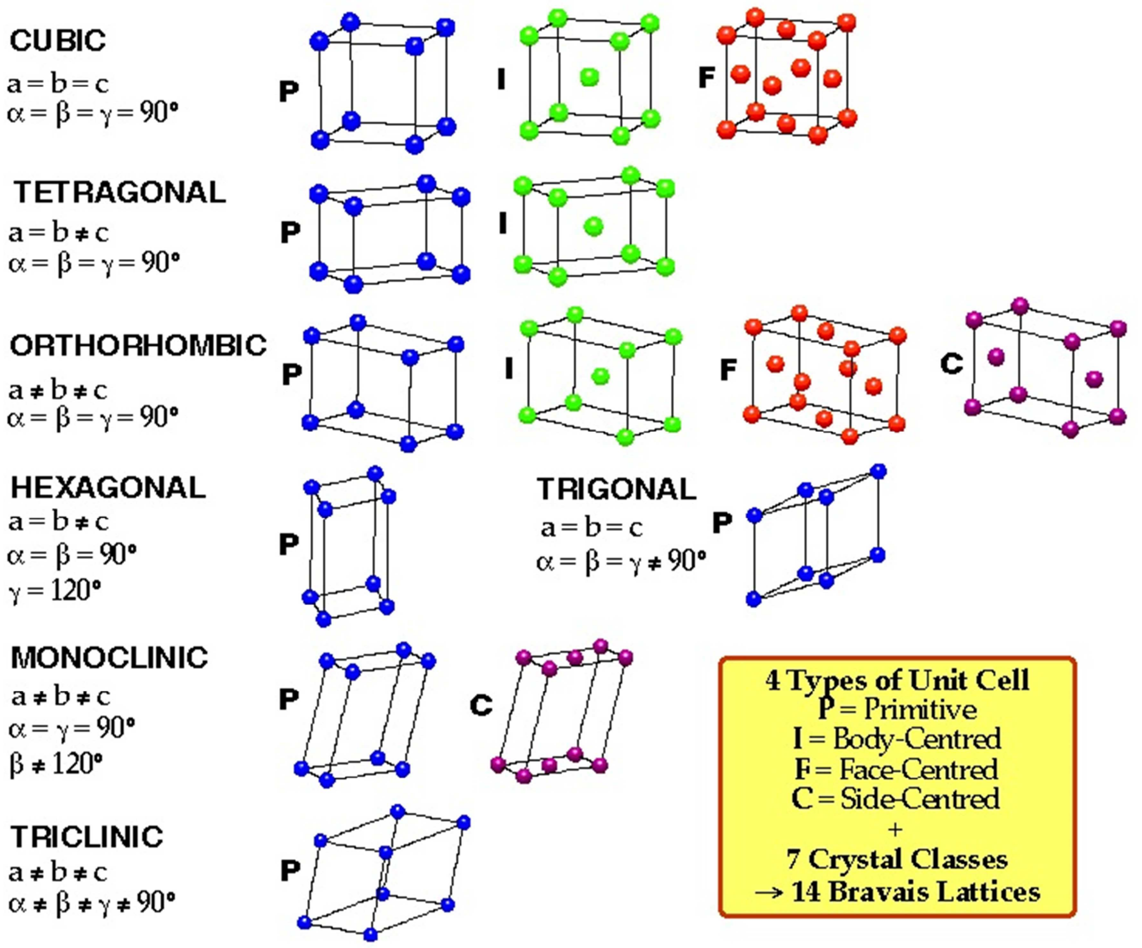

Fig. 2.2 - Schematic representation of the 14 different Bravais lattices possible found in nature.

Most semiconductors (including the ones presented in this thesis) are organized forming one or more face centered cubic (FCC) lattices. One can understand the structure of these crystals by setting the base at appropriate positions on a unit cell of the FCC lattice. For materials like Si, Ge, GaAs, InAs, and others, the base consists on one atom at the (0, 0, 0) position and another one at the (1/4, 1/4, 1/4), for each of these points. For materials of the IV group, like Si and Ge, consisting on only one atomic species, this leads to the diamond structure, i.e. two FCC lattices displaced from (1/4, 1/4, 1/4). For III-V semiconductors, like GaAs and InAs, the cation occupies the (0, 0, 0) position and the anion is in the (1/4, 1/4, 1/4), leading to a structure that is known as Zincblende [11].

However, two materials that organize in the same way can, still differ by the size of the lattice in each direction, i.e. they can have different lattice parameters. InAs and GaAs, as an example, are generally found at the Zincblend structure. Nevertheless, the fact that In is bigger than Ga makes the lattice parameter of the bulk InAs (6.0583 Å) larger than the GaAs (5.65325 Å). If we then deposit InAs on GaAs there will be an effort to adjust the lattice parameter at the interface, and therefore a strain must appear and, consequently, elastic energy may be stored in the film. Such effect sometimes might lead to the formation of structural defects, but is also responsible for the formation of nanostructures generally called islands (can be specifically named as huts, pyramids, domes, or other terms, depending on their characteristics) [12,13].

Once we know that atoms and molecules can be periodically arranged to form crystals, it is helpful to find a way to study the structure of such materials. Since we are talking about periodic arrangements with spacing of the order of angstroms, to obtain information about the structure of crystals it is necessary to use a radiation that is capable of diffract through their atomic planes, i.e. photons (or other particles like electrons or neutrons) with a wavelength with the order of magnitude found in the X-ray regime. The huge potential of X-ray photons (wavelength of some angstroms) for the study of nanomaterials has led scientists on the search of new sources of radiation and experimental techniques, aiming to take some benefit from this idea.

X-ray diffraction can be mathematically described by the elastic scattering of photons by atoms that constitute some families of planes, making it very useful to define a way to distinct and nominate different families of planes. The most usual way to nominate a family of planes is using the Miller's indexes. The Miller indexes (h, k, l) are defined so that the closest plane to the origin (but not passing through it) intercepts the axes ($\mathbf{a}_1$, $\mathbf{a}_2$, $\mathbf{a}_3$) at the (a_1/h, a_2/k, a_3/l) points. Some examples that help to clarify how one can determine the Miller indexes can be seen in figure 2.3. The planes of a given family are equally spaced, and this spacing d (in a cubic system) is given by:

$$d_{hkl} = \frac{a}{\sqrt{h^2+k^2+l^2}} \quad , \tag{2.1}$$

where a is the lattice parameter [14].

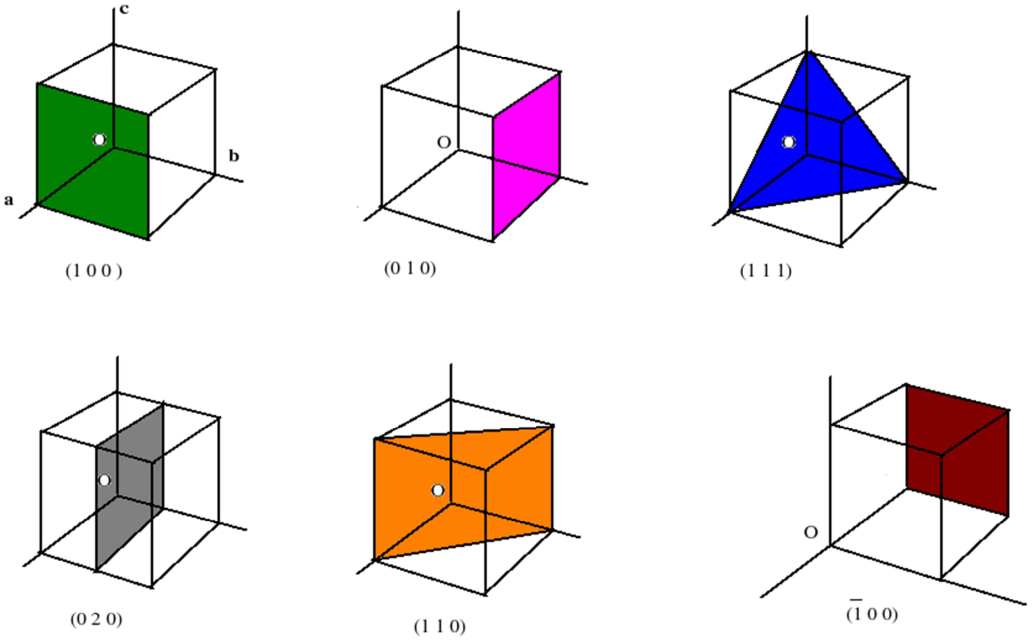

(1 0 0) (0 1 0) (1 1 1)

(0 2 0) (1 1 0) $(\bar{1}\ 0\ 0)$

Fig. 2.3 – Exemples of Miller indexes for centain family of planes.

2.2 X-ray diffraction by crystals

2.2.1 Coplanar diffraction

According to Bragg's Law (nλ = 2dsenθ), when the X-ray beam (wavelength λ and angle of incidence to the normal θ) is scattered in the atomic planes (with spacing d) of a crystal, if n is an integer the Bragg's law is satisfied, and then we have a diffraction condition (a constructive interference on the scattered beam). A sketch of this process can be seen in figure 2.4.

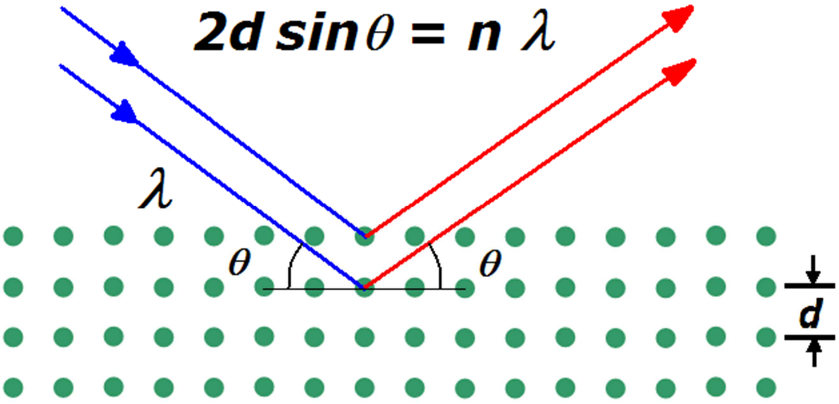

Fig. 2.4 – Schematic representation of Bragg's Law. A beam of wavelength λ and angle of incidence θ is scattered by the atomic planes of spacing d in the crystal. If nλ = 2dsenθ is valid for n integer, then the Bragg's Law is satisfied.

If the incident beam undergoes the diffraction process along the same plane on the crystal, that is, the incident and the reflected beams are coplanar, then one can say this is a coplanar diffraction geometry. A schematic representation that better illustrates coplanar diffraction can be seen in figure 2.5, where it is possible to see the incident beam making an angle θ with the sample, and the scattered one leaving at 2θ (relative to the incident beam) and going towards the detector. When the X-ray beam scattered by a family of planes we can also define the momentum transfer vector **Q** as the difference between the scattered wave vector and the incident wave vector, i.e. **Q** = **k`** - **k**.

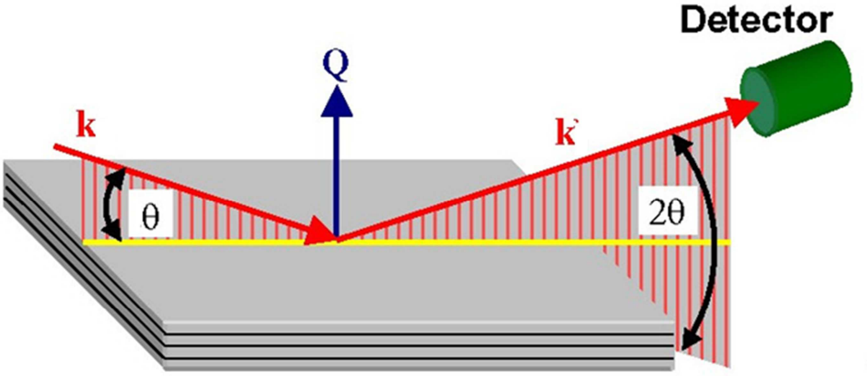

Fig. 2.5 – Schematic representation for the X-ray coplanar diffraction geometry. The beam impinge the crystal at an angle θ, and is reflected towards the detector at 2θ, so that **k** and **k`** are coplanar. One can also see the representation of the **Q** transfer wave vector, which respects the **Q** = **k`** - **k** relation [14].

We now want to better understand the signal obtained by the detector when the scattered X-ray beam is collected. The intensity I is defined such that the product of the scattering amplitude of the beam F with its complex conjugate F*, which can be calculated by:

$$F(\boldsymbol{Q}) = \sum_{l}^{all\ atoms} f_l(\boldsymbol{Q}) e^{i\boldsymbol{Q}\cdot\boldsymbol{r}_l} \quad , \qquad (2.2)$$

where $f_l(\boldsymbol{Q})$ is the atomic form factor (approximately the number of electrons Z, under non resonant conditions) for the atom situated at $\boldsymbol{r}_l$ ($\mathbf{r} = x_n\mathbf{a}_1 + y_n\mathbf{a}_2 + z_n\mathbf{a}_3$) position. It is important to notice that such equation has general validity (even for amorphous materials). But one can make it simpler for crystalline materials, which is possible since we can exploit the periodic repetition of the unit cell. Writing the position of each atom as the position of a unit cell and specifying the location of the atom inside the cell, equation 2.2 becomes:

$$F^{crystal}(\boldsymbol{Q}) = \sum_n e^{i\boldsymbol{Q}\cdot\boldsymbol{R}_n} \sum_j f_j(\boldsymbol{Q}) e^{i\boldsymbol{Q}\cdot\boldsymbol{r}_j} \quad , \qquad (2.3)$$

where the first term is a summation over all the n sites of the crystal lattice, while the second term is a summation over the structure factor $f_j(\boldsymbol{Q})$ for all the atoms of the unit cell located at the position r_j of the cell occupying the position R_n.

The first term on the right side of equation 2.3, referring to the lattice form factor, tells us that only when the moment transfer vector **Q** coincides with the reciprocal lattice vector **G**, defined as $\mathbf{G} = h\,\mathbf{a}_1^* + k\,\mathbf{a}_2^* + l\,\mathbf{a}_3^*$, where $(\mathbf{a}_1^*, \mathbf{a}_2^*, \mathbf{a}_3^*)$ is the basis of the reciprocal lattice defined by $\mathbf{a}_n^* = 2\pi/\mathbf{a}_n$, is that the scattering amplitude will be non-zero. Such result is known as Laue condition (details can be seen in [14]).

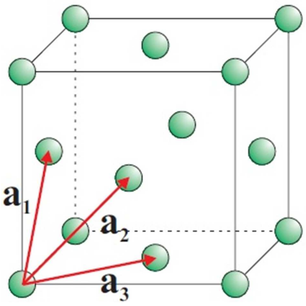

Fig. 2.6 – Sketch of the FCC lattice and the vectors $\mathbf{a}_1$, $\mathbf{a}_2$ e $\mathbf{a}_3$ that can define it [14].

To define when the second term will be non-zero, one must first understand the packaging of the atoms in the crystal being studied. For a FCC structure, as shown in figure 2.6, $\mathbf{r}_1 = 0$, $\mathbf{r}_2 = (\mathbf{a}_1 + \mathbf{a}_2)/2$, $\mathbf{r}_3 = (\mathbf{a}_2 + \mathbf{a}_3)/2$ and $\mathbf{r}_4 = (\mathbf{a}_3 + \mathbf{a}_1)/2$ are parallel to the edges of a cube, and then:

$$\boldsymbol{Q} = (h\boldsymbol{a}_1^* + k\boldsymbol{a}_2^* + l\boldsymbol{a}_3^*) \quad , \qquad (2.4)$$

leading to

$$F^{FCC} = \sum_j f(\boldsymbol{Q})\, e^{i\boldsymbol{Q}\cdot\boldsymbol{r}_j} \qquad , \qquad (2.5)$$

$$F^{FCC} = f(\boldsymbol{Q})(e^0 + e^{i\frac{1}{2}(\boldsymbol{a}_1 + \boldsymbol{a}_2)\cdot(h\boldsymbol{a}_1^* + k\boldsymbol{a}_2^* + l\boldsymbol{a}_3^*)} + e^{i\frac{1}{2}(\boldsymbol{a}_2 + \boldsymbol{a}_3)\cdot(h\boldsymbol{a}_1^* + k\boldsymbol{a}_2^* + l\boldsymbol{a}_3^*)} + e^{i\frac{1}{2}(\boldsymbol{a}_3 + \boldsymbol{a}_1)\cdot(h\boldsymbol{a}_1^* + k\boldsymbol{a}_2^* + l\boldsymbol{a}_3^*)}) \qquad , \qquad (2.6)$$

$$F^{FCC} = f(\boldsymbol{Q})(1 + e^{i\pi(h+k)} + e^{i\pi(k+l)} + e^{i\pi(l+h)}) \qquad , \qquad (2.7)$$

$$F^{FCC} = f(\boldsymbol{Q}) * \begin{cases} 4, & if\ h,k,l\ are\ all\ even\ or\ all\ odd \\ 0, & otherwise \end{cases}. \qquad (2.8)$$

Thus, reflections like (1 0 0), (2 1 0), (2 2 1), and others, have zero structure factor and therefore zero amplitude for an FCC crystal, while reflections like (2 2 0), (2 0 0), (4 0 0), and others, have non-zero amplitude for a crystal that follows this structure.

The samples presented by this thesis (Si, Ge, GaAs, InAs) have two FCC lattices displaced ¼ in each direction (Diamond and Zinc Blende structures). We can then write the structure factor for the diamond lattice as the product of the structure factors of a FCC lattice and a base of two atoms, considering one in (0,0,0) position and the other one in the (1/4,1/4.1/4). Thus, the structure factor of Si becomes:

$$F^{Si} = (f^{Si}(\boldsymbol{Q}) + f^{Si}(\boldsymbol{Q})e^{i2\pi(\frac{h}{4}+\frac{k}{4}+\frac{l}{4})})(1 + e^{i\pi(h+k)} + e^{i\pi(k+l)} + e^{i\pi(l+h)}). \qquad (2.9)$$

It is now possible to see that the (1 1 1) reflection, for example, has structure factor F = 4 (1-i), the (4 0 0) has structure factor 8 and the (2 0 0) e (2 2 2) reflections are forbidden. On allowed reflections the diffracted intensity will be proportional to the product of the structure factor with its conjugate complex (F x F*), and the complex value from F at the (1 1 1) reflection becomes real.

To illustrate the case for materials with the Zincblende structure, one can see that the GaAs structure factor, considering the Ga at the (0,0,0) position and As at (1/4,1/4,1/4), is:

$$F^{GaAs} = (f^{Ga}(\boldsymbol{Q}) + f^{As}(\boldsymbol{Q})e^{i2\pi\left(\frac{h}{4}+\frac{k}{4}+\frac{l}{4}\right)})(1 + e^{i\pi(h+k)} + e^{i\pi(k+l)} + e^{i\pi(l+h)}). \quad (2.10)$$

Therefore, the (2 0 0) reflection, forbidden at the Diamond (Si/Ge) structure, has structure factor given by:

$$F^{GaAs} = 4(f^{Ga}(2,0,0) - f^{As}(2,0,0)) \quad , \quad (2.11)$$

i.e. not zero, since Ga and As have a different number of electrons ($Z_{As} > Z_{Ga}$) and, therefore, $f^{Ga}(\boldsymbol{Q}) \neq f^{As}(\boldsymbol{Q})$ [14].

2.2.2 Grazing-incidence diffraction (GID)

Due to their weak interaction with matter the X-ray photons have a large penetration depth, which makes coplanar geometry X-ray diffraction a not suitable technique to study materials surfaces. For a beam with wavelength on the order of angstrom, an angle of incidence about 1° is already sufficient to result in an X-ray penetration depth of thousands (or even tens of thousands) of nanometers, as showed by figure 2.7. However, when studying nanostructures it is generally desirable to clearly detect the signal coming from objects on the surface of the sample. In order to overcome such issue, one can make use of a X-ray diffraction non-coplanar geometry technique, with the incident beam under grazing incidence diffraction (GID) [15,16].

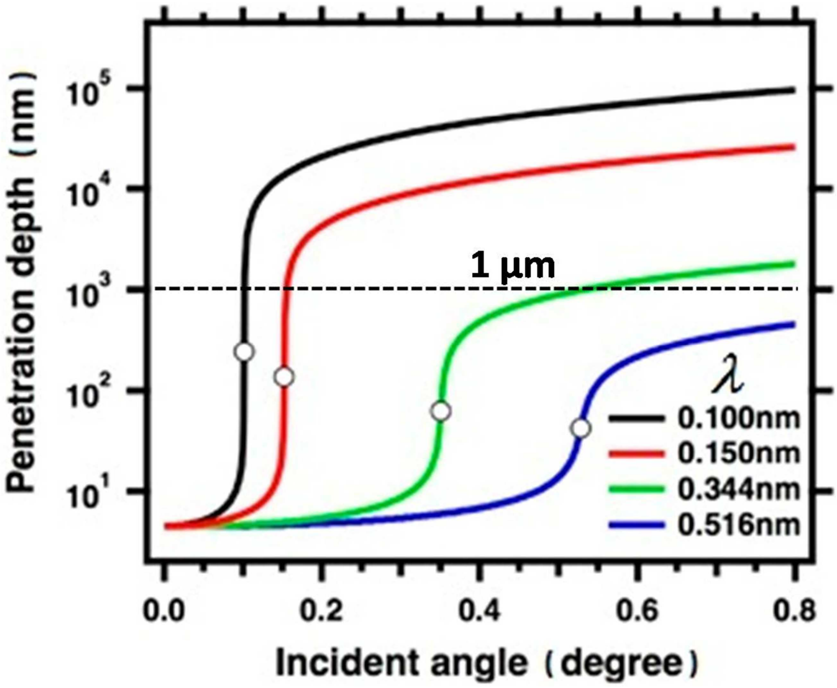

Fig. 2.7 – The penetration depth of the X-ray beam (wavelength of a few angstroms) is larger than 1,000 nanometers for incident angles greater than 1°. This effect makes the coplanar geometry unsuitable for the study of nanostructures on the surface of the sample. The white dots indicate the critical angle for each selected wavelength [17].

GID measurements are carried out at a very low incidence angle, in order to minimize the signal coming from deeper layers of the crystal, and generating a better contrast that enhances the relative signal coming from the surface. In a typical geometry to perform GID measurements, the incident X-ray beam illuminates the surface of the sample at an angle very close to the critical angle for total external reflection (about 0.3° for the samples presented in this thesis). The scattered beam is then collected at grazing exit angles, either in the same direction as the incident beam, giving rise to the grazing incidence small angle scattering (GISAXS) signal (good for the investigation of nano objects), or even at higher diffraction scattering in-plane angles, the GID signal. A representative sketch for GID can be seen in Figure 2.8. For samples containing islands, the GISAXS signal contains information about the form and size distribution of the structures, while the in-plane signal (GID) gives us the information about size, crystalline packaging and strain.

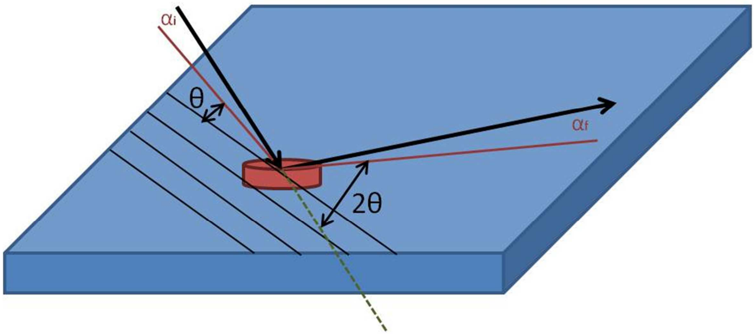

Fig. 2.8 – Schematic representation of the X-ray diffraction under grazing-incidence (GID). The atomic planes of the sample are represented by black lines along the surface. The beam hits the sample at a small incidence angle α_i with respect to the surface, but making an angle θ with the crystalline planes (in-plane). Thus, it is reflected at an angle α_f out-of-plane and 2θ in-plane.

One can now decompose the moment transfer vector **Q** into three components: $\mathbf{q}_z$, $\mathbf{q}_r$ e $\mathbf{q}_a$. The $\mathbf{q}_z$ vector represents the momentum transfer in the normal direction with respect to the surface, $\mathbf{q}_r$ is the radial momentum transfer, which defines the distance to the origin of the reciprocal space (and, consequently, the indexes of the reflection), and $\mathbf{q}_a$ is the angular momentum transfer vector, which arises for positions of the reciprocal space where there is some Δθ deviation of the diffracted beam with respect to the Bragg condition (θ = 2θ/2). It is shown in figure 2.9 a schematic representation of $\mathbf{q}_z$, $\mathbf{q}_r$ e $\mathbf{q}_a$, where a side view and a top view of the process can be seen.

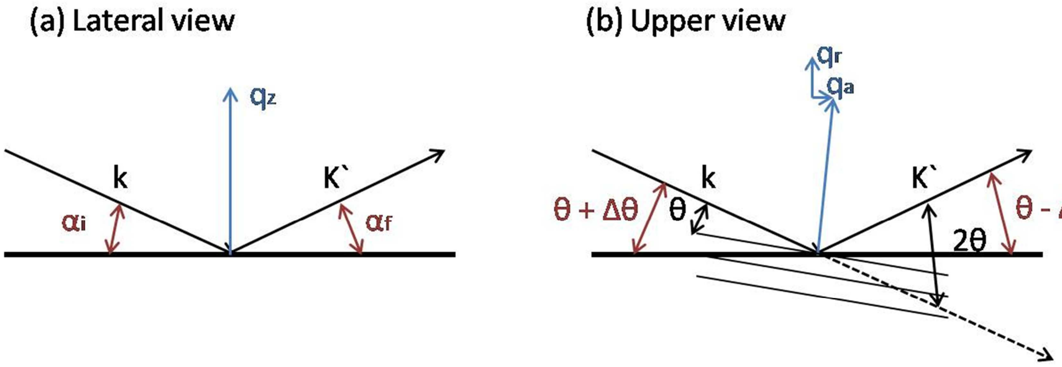

Fig. 2.9 – Schematic representation of the vectors $\mathbf{q}_z$, $\mathbf{q}_r$ e $\mathbf{q}_a$. One can see in (a) a lateral view of the process, where the grazing angles α_i and α_f of incidence and reflection, respectively, are represented in red and the transfer vector for the vertical moment is in blue. In (b) it is shown the transfer vectors of radial and angular momentum on top view.

Measurements in reciprocal space that run parallel to each of these three vectors have different meanings. The $\mathbf{q}_r$ direction gives us the local lattice parameter (strain). If we measure $\mathbf{q}_a$ for a fixed lattice parameter we can extract information about the size and shape of the crystals that diffract at a given Bragg condition. Measurements along $\mathbf{q}_z$ provide information regarding variations in the electron density and crystal structure in the normal direction with respect to the surface [18].

To better understand the meaning of a measure along $\mathbf{q}_r$ or $\mathbf{q}_a$, one can refer to the schematic representation of the H-K plane of the reciprocal space, shown in figure 2.10 with the directions of both, radial and angular vectors.

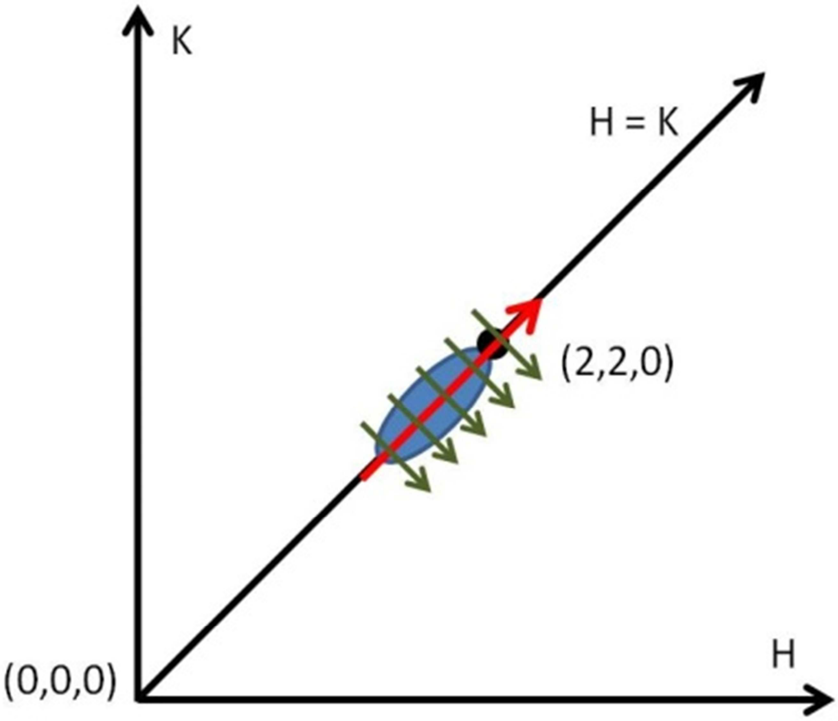

Fig. 2.10 – Schematic representation of the H-K plane of the reciprocal space, showing the scan direction for measurements along $\mathbf{q}_r$ (red arrow) and $\mathbf{q}_a$ (green arrows). The black dot corresponds to the (2,2,0) position in the reciprocal lattice and the region in blue represents an area under strain. Radial measurements follow along the path that leads a given reflection to the origin of the reciprocal lattice. Angular measurements are perpendicular to the radial scans.

2.3 Resonant X-ray scattering (charge)

To mathematically determine the correction factors for the atomic scattering factor in the resonant case, one can consider a classical model of an electron connected to an atom. This electron is subjected to an electric field due to the incident X-ray beam, $\boldsymbol{E_{in}} = E_0 \mathrm{e}^{-i\omega t}\hat{\boldsymbol{x}}$, linearly polarized along the x-axis, with amplitude E_0 and frequency ω. The motion of the electron can be described by:

$$\ddot{x} + \Gamma\dot{x} + \omega_s^2 x = -\left(\frac{eE_0}{m}\right)\mathrm{e}^{-i\omega t} \quad . \tag{2.12}$$

The damped term that depends on the velocity, $\Gamma\dot{x}$, represents the energy dissipation of the applied field, mainly due to the reissue of radiation. The damping constant, which has dimension of frequency, is generally much smaller than the resonance frequency ω_s. Using a solution of the type $x(t) = x_0\mathrm{e}^{-i\omega t}$ one obtain the following solution for the amplitude of the forced oscillator:

$$x_0 = -\left(\frac{eE_0}{m}\right)\frac{1}{\omega_s^2-\omega^2-i\omega\Gamma} \quad . \tag{2.13}$$

An observer at a distance R and a time t would see the irradiated field, which is proportional to the acceleration $\ddot{x}(t - R/c)$, on the retarded time $t' = t - R/c$:

$$E_{rad}(R,t) = \left(\frac{e}{4\pi\epsilon_0 Rc^2}\right)\ddot{x}(t-\frac{R}{c}) \quad , \tag{2.14}$$

Where the polarization factor, by convenience, was set as $\hat{\boldsymbol{\varepsilon}} \cdot \hat{\boldsymbol{\varepsilon}}' = 1$. Then inserting $\ddot{x}(t - R/c) = -\omega^2 x_0 \mathrm{e}^{-i\omega t}\mathrm{e}^{i(\omega/c)R}$, with x_0 given by the equation 2.13, one finds:

$$E_{rad}(R,t) = \frac{\omega^2}{(\omega_s^2 - \omega^2 - i\omega\Gamma)} \left(\frac{e^2}{4\pi\epsilon_0 mc^2}\right) E_0 \mathrm{e}^{-i\omega t} \left(\frac{\mathrm{e}^{ikR}}{\mathrm{R}}\right) \quad , \tag{2.15}$$

or, equivalently:

$$\frac{E_{rad}(R,t)}{E_{in}} = -r_0 \frac{\omega^2}{(\omega^2 - \omega_s^2 + i\omega\Gamma)} \left(\frac{\mathrm{e}^{ikR}}{\mathrm{R}}\right) \quad . \tag{2.16}$$

The atomic scattering length, f_s, is defined as the amplitude of the scattered spherical wave, ($\mathrm{e}^{ikR}/\mathrm{R}$). In $-r_0$ units, one can write:

$$f_s = \frac{\omega^2}{(\omega^2 - \omega_s^2 + i\omega\Gamma)} \quad , \tag{2.17}$$

which represents the atomic scattering length for one oscillator. For frequencies much larger than the resonant frequency, ω >> ω_s, one can consider a free electron, and we are left with the well known case of the Thomson scattering, i.e. $f_s = 1$.

The expression for f_s given by equation 2.17 can be further rearranged as follows:

$$f_s = \frac{\omega^2 - \omega_s^2 + i\omega\Gamma + \omega_s^2 - i\omega\Gamma}{(\omega^2 - \omega_s^2 + i\omega\Gamma)} \quad , \tag{2.18}$$

$$f_s = 1 + \frac{\omega_s^2 - i\omega\Gamma}{(\omega^2 - \omega_s^2 + i\omega\Gamma)} \quad , \tag{2.19}$$

$$f_s \cong 1 + \frac{\omega_s^2}{(\omega^2 - \omega_s^2 + i\omega\Gamma)} \quad , \tag{2.20}$$

where the result of eq. 2.20 is due to the fact that Γ is usually much smaller than ω_s. It becomes clear that the second term is the dispersion correction for the scattering factor. Writing $\chi(\omega)$ in the as $\chi(\omega) = f_s' + if_s''$, such that:

$$\chi(\omega) = f_s' + if_s'' = \frac{\omega_s^2}{(\omega^2 - \omega_s^2 + i\omega\Gamma)} \quad , \tag{2.21}$$

the real part is given by:

$$f_s' = \frac{\omega_s^2(\omega^2 - \omega_s^2)}{\left(\omega^2 - \omega_s^2\right)^2 + (\omega\Gamma)^2} \quad , \tag{2.22}$$

and the imaginary part by:

$$f_s'' = -\frac{\omega_s^2 \omega\Gamma}{\left(\omega^2 - \omega_s^2\right)^2 + (\omega\Gamma)^2} \quad . \tag{2.23}$$

The factors of equations 2.22 and 2.23 are known as the dispersion and absorption correction factors. Their shape as a function of the frequency near an absorption edge can be seen in figure 2.11.

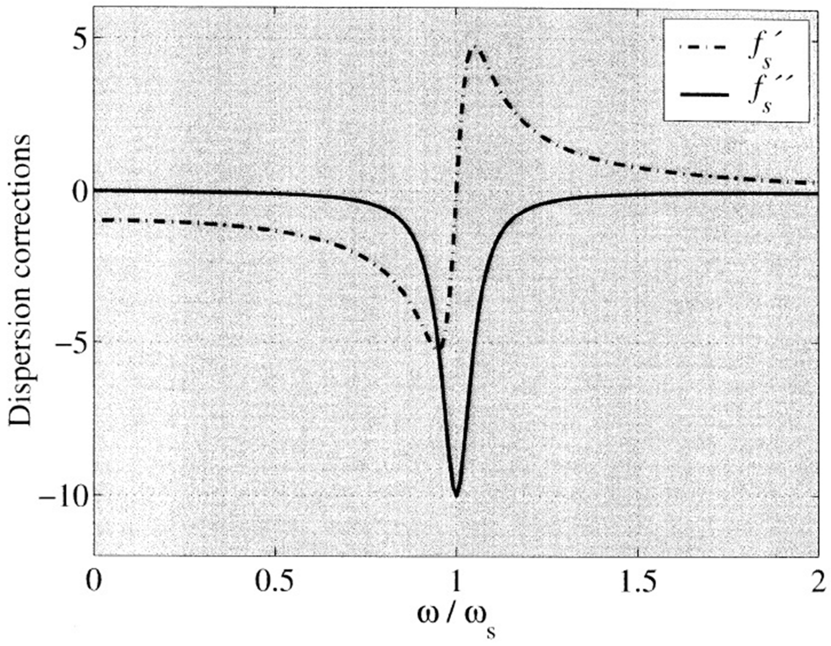

Fig. 2.11 – The real part, f_s', and the imaginary part, f_s'', of the atomic scattering correction on the vicinity of an absorption edge, plotted as a function of the frequency ω relative to the resonant frequency ω_s, calculated from the damped harmonic oscillator model [14].

However, it is not always convenient to depend on this theoretical formulation to obtain the scattering factor correction terms, since it may not be sufficiently accurate. Another serious issue is that it is often not easy to look for effects that point out to a direct value for f_s' or f_s''. Luckily, there is a method to obtain f_s' indirectly, using the absorption cross section $\sigma_a(\omega)$. Initially, one can experimentally determine $\sigma_a(\omega)$, and then obtain f_s'' through the equation 2.24:

$$f''(\omega) = -\left(\frac{\omega}{4\pi r_0 c}\right)\sigma_a(\omega) \quad , \tag{2.24}$$

The next step, that will allow us to obtain the value for f_s' exploits the relations between f_s' e f_s'', shown in the equations 2.25 e 2.26:

$$f'(\omega) = \frac{2}{\pi}\wp\int_0^\infty \frac{\omega' f''(\omega')}{(\omega'^2-\omega^2)} d\omega' \, , \tag{2.25}$$

$$f''(\omega) = -\frac{2\omega}{\pi} \wp \int_0^{\infty} \frac{f'(\omega')}{(\omega'^2-\omega^2)} d\omega' \quad , \qquad (2.26)$$

where $\wp$ represents the principal value for the Cauchy integral [19]. These equations are known as the Kramers-Kronig relations. The meaning of these relations consist on the fact that, if the dependency of the absorption straight section with respect to the energy is known, then f_s'' can be determined by equation 2.24, and with a substitution in equation 2.25 one can also obtain the value for f_s', the real part of the dispersion correction for the scattering amplitude [14]. The figure 2.12 illustrates the dependency of the dispersion and the absorption factors with respect to the energy variation for Zn. It is possible to note that the experimental curves converge to the theoretical ones by increasing the range of energy used on the absorption measurements [20].

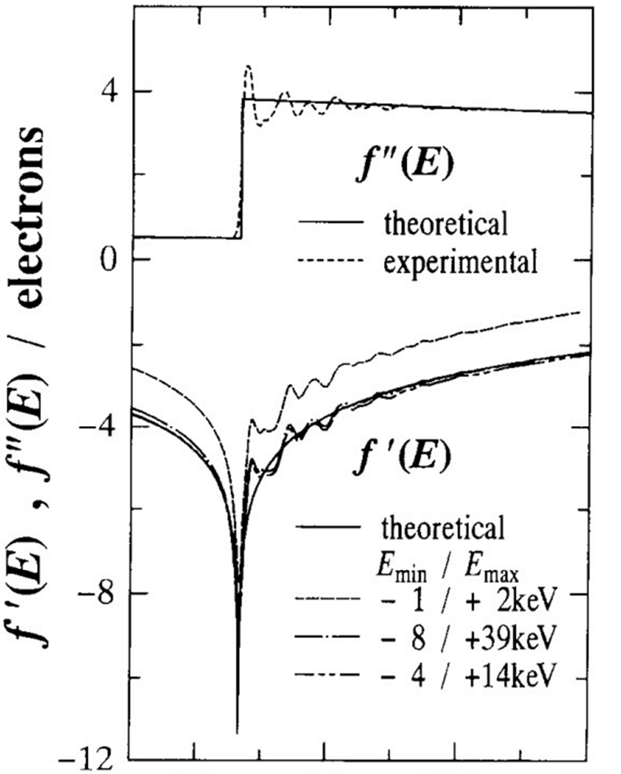

Fig. 2.12 – Energy variation of the anomalous dispersion factors for Zn. Solid lines represent the theoretical curves, while dashed lines stand for experimental ones [20].

2.4 Micro and nano-focusing diffraction with synchrotron radiation

During the last decade many techniques have been developed to obtain micro- and nanoscopic images, in order to study objects with nanometric dimensions. Since X-ray diffraction is a powerful technique to obtain structural information of nano-objects, it would be highly appreciated to make use of it to obtain high resolution images of nanostructures correlating spatial position and structural properties.

A technique able to transform a beamline dedicated to X-ray diffraction into a giant powerful strain microscope capable of making real space images of the strain field on nanostructures was implemented in the ID01 beamline, in the European Synchrotron Radiation Facility (ESRF). This technique consists on a two-dimensional continuous mapping of the sample with nanometric resolution, at a chosen Bragg condition. The X-ray beam can be focused using either a Fresnel Zone Plate (FZP) or a pair of KB mirrors. Using the first one a focus of 70 nm on the vertical plane and 100 nm on the horizontal can be achived, while the second device produces a 200 nm focus in the vertical and 300 nm in the horizontal direction, but with a higher photon flux. A beam stopper is generally placed just before the FZP to prevent direct beam transmission through the central region of the lens (which is not able to focus it). An order sorting aperture (OSA) is used to eliminate focusing by higher orders diffraction.

A two-dimensional detector is then positioned at the scattering angle 2θ and records the images obtained from each region of the sample for the chosen Bragg condition. A set of piezoelectric stages with closed loop are responsible for moving the sample so that the beam scans the entire area to be mapped. Maps correlating information in real space with the reciprocal space scattering results can be obtained by moving the sample while the two-dimensional detector saves the diffracted pattern for each position of the piezoelectric stages [21]. A schematic representation of the K-mapping setup is shown in figure 2.13.

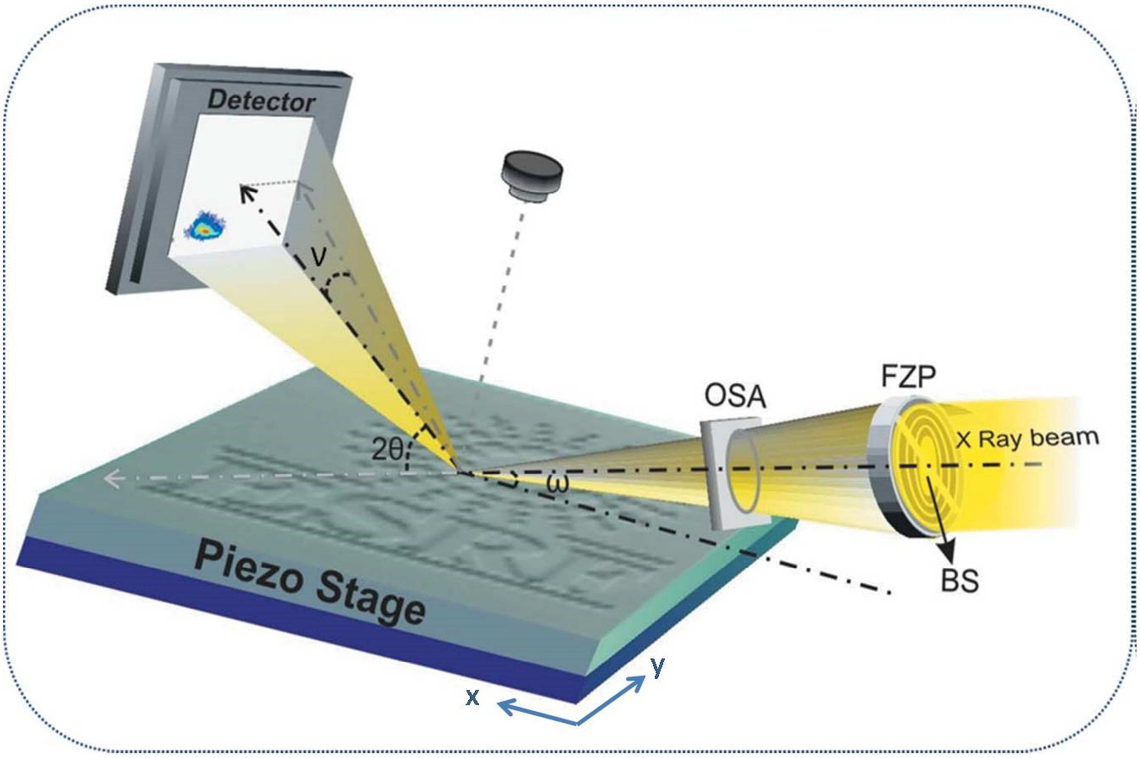

Fig. 2.13 – Schematic representation of the setup used for the quicK-MAPping technique (K-MAP), with a Fresnel Zone Plate (FZP) and in coplanar geometry. The X-ray beam is focused using the FZP X-ray lens, hits the sample at an incient angle ω and diffracts at an angle 2θ. An optical microscope is positioned just above the sample to help on the alignment procedures [21].

2.5 Coherent Diffraction Imaging

Coherent Diffraction Imaging (CDI) is a novel form of lensless X-ray imaging, where the diffraction pattern of a noncrystalline specimen or a nanocrystal is first measured and then directly inverted to obtain a high-resolution image [22]. The phase is retrieved by combining the oversampling method [23] and iterative phase-retrieval algorithms [24-30]. The idea of CDI was suggested by Sayre [31], but it was only in 1999 that an experimental demonstration was first conducted by Miao *et al.* [32]. Since then, CDI has been applied to imaging a wide range of materials science and biological samples such as nanoparticles, nanocrystals, biomaterials, cells, cellular organelles, and viruses [22]. An scheme illustrating the general idea of a CDI experiment is shown in figure 2.14.

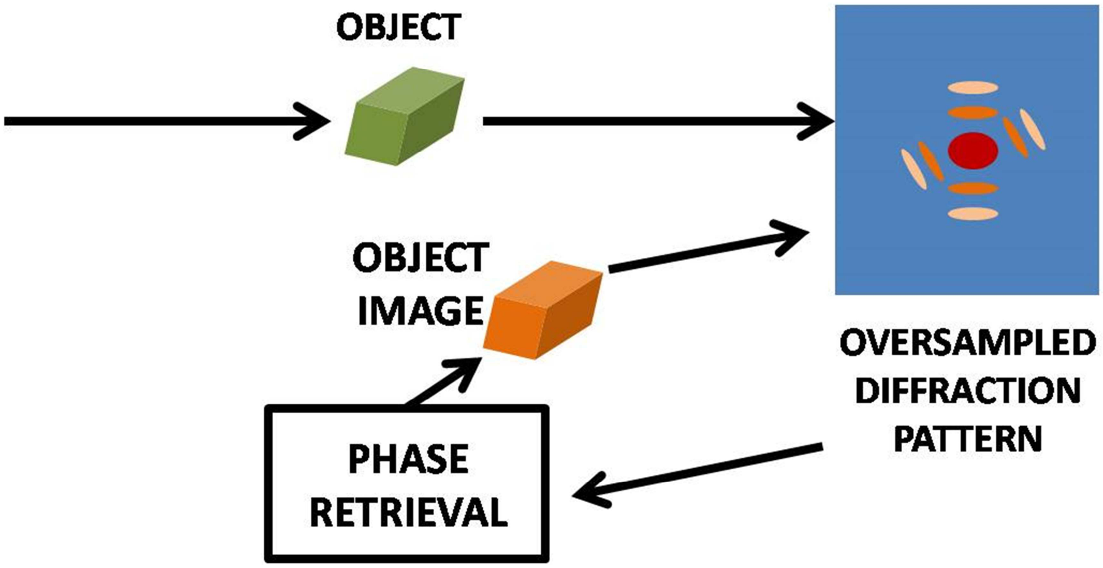

Fig. 2.14. A CDI experiment consists on a coherent wave illuminating an object, and then the oversampled diffraction pattern is measured by a 2D detector. The image is reconstructed from the diffraction pattern by iterative phase-retrieval algorithms.

There are four different techniques for CDI, each one suitable for specific cases. In the plane-wave CDI the beam insides directly on the object, and the scattered wave is collected by the detector. This geometry is insensitive to sample vibrations, and can easily be implemented in single-shot experiments [33,34]. In the Fresnel CDI the beam passes through a zone plate, then only the first order is selected by an order-sorting aperture, insides in the object and is collected by the detector. The algorithm convergence is fast, and the real space resolution is generally good with this geometry [35]. In the scanning CDI (also known as ptychography) an aperture is used before the object, so one can collect the scattered wave corresponding to small regions. This geometry is applicable to large objects and its convergence is also fast [36]. In the Bragg CDI the beam and the crystal are in Bragg condition, so one can collect the diffracted wave for specific reflections. It is very convenient to study nanocrystals and allows the determination of the 3D strain tensor and displacement field [22]. A schematic representation of the four techniques is shown in figure 2.15.

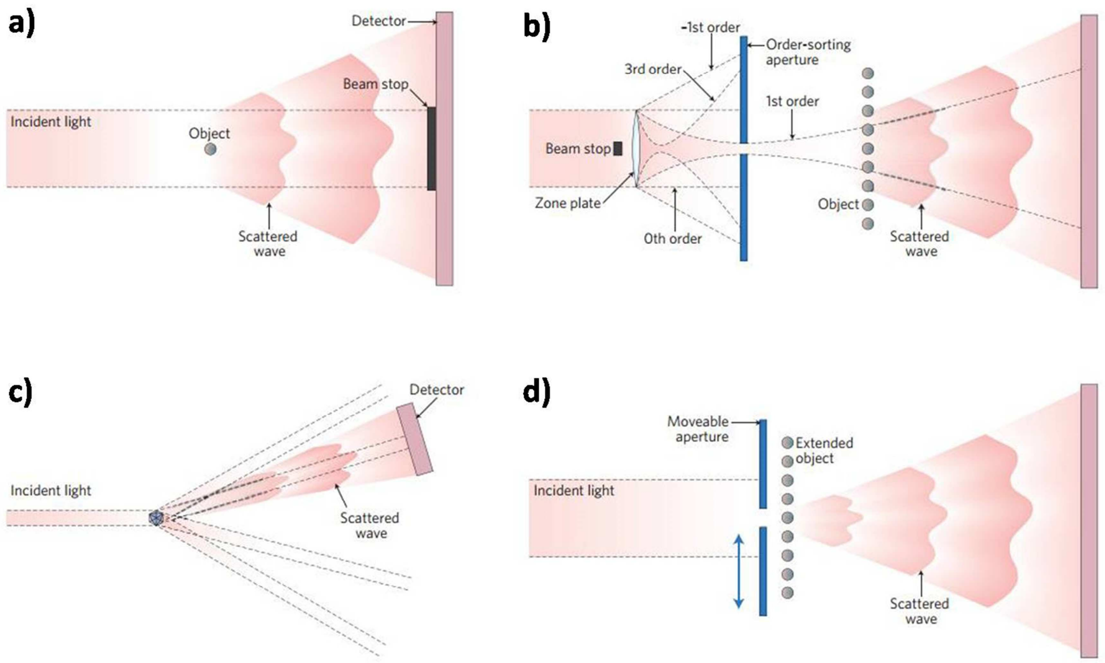

Fig. 2.15. Schematic representation of the (a) Plane-wave, (b) Fresnel, (c) Bragg and (d) Ptychography.

This technique is ideally suited for non-periodic objects or nanocrystals. Its resolution is limited by the radiation damage to sample and the sample stability, resulting generally in tens of nanometers (20 nm for Fresnel CDI and 30~50 nm for Scanning, Bragg and Plane-wave CDI). Due to the sample instability, to perform a good CDI experiment one needs short and bright pulses.

In order to retrieve the morphology of crystalline nanostructures, and also associate with the strain field, tri-dimensional Bragg CDI measurements can be performed. To obtain the data that allows reconstructing the structures in direct space, one must initially find a Bragg reflection, maximize its intensity, then change the Bragg (incident) angle until the signal disappears in both directions, and save the images for different incident angle values between both vanishing angles. If the collected data is good enough, one can obtain the nanostructure in direct space using iterative phase-retrieval algorithms.

Chapter 3

Other characterization techniques

3.1 Atomic Force Microscopy

Atomic Force Microscopy (AFM) is an experimental technique suitable to study the morphology, thermal, electric and magnetic properties of surfaces, which has been intensively used since the second half of the 1980s. The topographic mapping of the surface obtained by this technique is not dependent on the material characteristics as conductivity, and allows the measurement of very small variations of interaction forces between the surface and the probe, enabling the acquisition of images even in atomic scale. The use of AFM also extends to different types of surfaces, such as liquids [37].

The operation of an AFM microscope can be briefly described as: i) initially a laser beam hits the back of a small lever containing a probe (tip) of nanometer size; ii) this beam is reflected and then collected by a detector divided into four zones, which is sensitive to changes in the signal arriving at each zone (and thus allowing to define a reference signal); iii) the probe, which is at the end of the lever, ends at a very thin tip, which is brought into contact with the surface of the sample; iv) the probe moves guided by a calibrated piezoelectric stage controlled via software, which allows the probe to perform well defined scans on the surface to be studied. During the scan the probe goes up and down according to the surface morphology, changing the direction of reflection of the laser. When it happens, the laser will hit a different point of the detector, and the piezoelectric stage will act on the sample (or the probe, depending on the microscope) in order to keep the force constant. Thus, a two-dimensional surface scan produces a topographic map of the sample. A schematic representation of the technique is shown in figure 3.1.

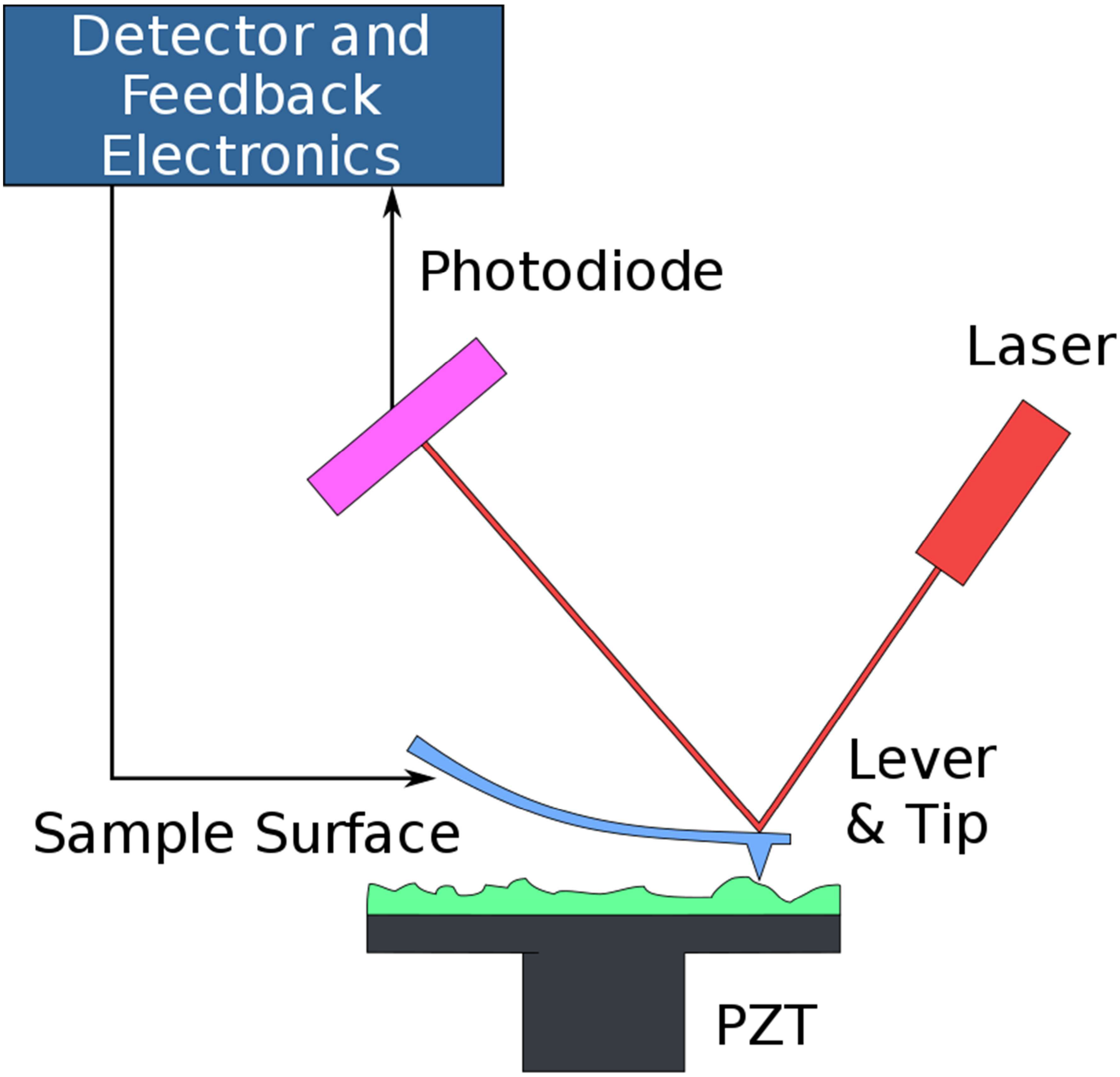

Fig. 3.1 – Schematic representation of the atomic force microscopy technique.

Modern AFMs can be operated in contact or semi-contact mode. In contact mode the probe remains constantly pressed against the sample, while in semi-contact mode the probe vibrates at a characteristic frequency, touching the surface of the sample only by a small interval during the oscillatory movement. Both modes are somewhat destructive, but the semi-contact mode tends to preserve the original morphology better. In figure 3.2 one can see an example of images obtained by AFM, where both the two-dimensional and tri-dimensional view of Ag nanoparticles are shown.

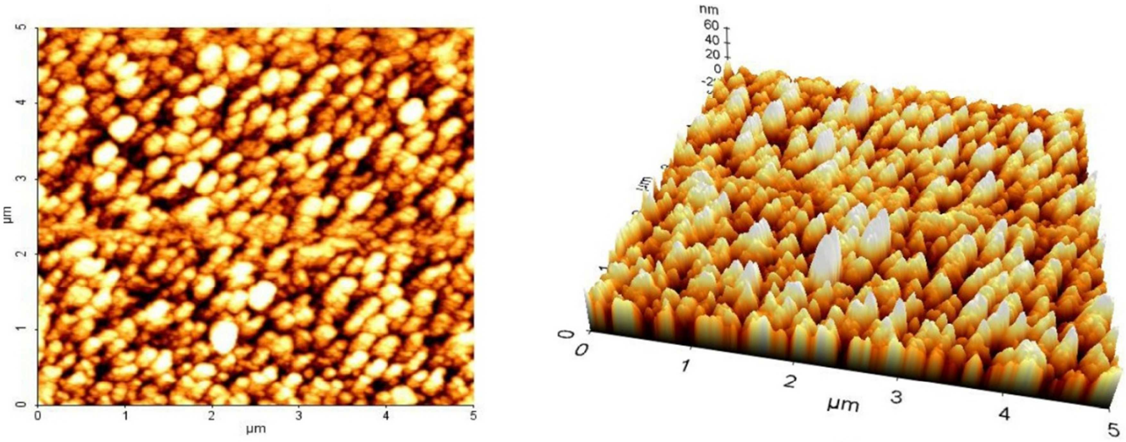

(a) (b)

Fig. 3.2 – (a) Two-dimensional and (b) tri-dimensional views for AFM measurements on Ag nanoparticles [38].

3.2 Finite Elements Simulation

When the mathematical problems become too complex to be solved analytically, emerges the need to find a method to obtain the desired solution numerically. The Finite Elements Method (FEM) is a computational approach to solve complex physical and mathematical problems, which consists on obtaining numerical solutions for problems that can be described by differential equations. It divides the structure into a large number of small elements (pieces of the original structure) and reconnects these elements into nodes, remolding the original structure back again, which results in a set of differential equations to be solved [39].

The method was initially developed as a computational simulation method to the analysis of aerospace structures back on the 1960s. It quickly began to be used for the design and analysis of complex structures, not only on the aerospace, but also civil and mechanical engineering. In the late 1960s the range of problems that could be solved by the method became much broader, with the emergence of problems involving fluids, thermodynamics and electromagnetism. In the 1970s, the method began to gain attention also among mathematicians and the software companies, which led the FEM to be divided into academic applications and the development of commercial products (Abaqus, Adina, Ansys , among others) [40]. Recently, the method has shown its value on the study of nanostructures.

One of the main factors that made FEM a very attractive method, for both engineering applications and the analysis of fundamental problems is the huge improvement on the hardware industry during the last decades. The fact that we now have access to computers that are much faster and capable of performing simultaneous tasks is crucial for software packages based on the numerical solution of differential equations. Today, FEM based software give us the possibility to work with problems that present complex initial conditions such as inertial forces, pressure, temperature changes, time dependent frequencies, tensions and elastic deformations, chemical gradients, among others.

Finite elements software will try to solve numerically the proposed problem, finding the equations of interest according to the initial conditions previously specified by the user. We can, as an example, analyze systems submitted to strain fields, which can be originated by a lattice parameter difference. Materials subject to such condition undergo elastic relaxation, which is in turn mathematically described by the Hooke's Law (for small deformations). For an isotropic cubic lattice system with negligible shear (which is a common generalization for the materials studied in this thesis) the generalized Hooke's Law can be written as shown by equation 3.1:

$$\begin{bmatrix}\sigma_x\\ \sigma_y\\ \sigma_z\end{bmatrix} = \frac{E}{(1+\nu)(1-2\nu)}\begin{bmatrix}1-\nu & \nu & \nu\\ \nu & 1-\nu & \nu\\ \nu & \nu & 1-\nu\end{bmatrix}\begin{bmatrix}\varepsilon_x\\ \varepsilon_y\\ \varepsilon_z\end{bmatrix} \quad , \qquad (3.1)$$

where σ_i represents the stress and ε_i indicates the strain in the i direction, E is the Young's modulus (defined as the ratio of stress applied in one direction to the strain in the same direction), and ν is the Poisson's ratio of the material (defined as the fraction of volume expanded in a certain direction divided by the fraction of volume compressed in orthogonal directions). For two directions in-plane and the third one out-of-plane (considering the out-of-plane as the growth direction) we can assume that, for the last deposited layer, the out-of-plane stress is zero, since the material is free to expand. In this case, the out-of-plane strain relates to the in-plane strain by the equation 3.2 [1]:

$$\varepsilon_{\perp} = \frac{-2\nu}{1-\nu}\varepsilon_{||} \qquad , \tag{3.2}$$

And the software is able to compute one of the values if the other one is provided by the user, based on experimental data.

However, finite element software does not directly deal with strain. It actually evaluates the displacement of each portion of the material, comparing with the original position before the relaxation process. To map the strain along the geometry the program solves equation 3.3, which relates the strain with the displacement (u_i) in the direction i (and analogously for the other directions):

$$\varepsilon_i = \frac{\partial u_i}{\partial i} \qquad . \tag{3.3}$$

Chapter 4

Quantitative measurement of Manganese incorporation into (In,Mn)As islands by resonant X-ray scattering

4.1 Motivation

In the past decades semiconductor materials with magnetic properties have attracted the attention of the scientific community. Intense effort has been focused on the possibility of combining electronic charge with the spin degree of freedom in a single magneto-electronic device [41-52]. Particularly interesting physical properties, pointing to a potential use in spintronics, are foreseen for In(Mn)As, as well as Ga(Mn)As [42-45,48,51-57]. Thin films and nanostructures based in these materials are strong candidates to play a substantial role on the next generation of optoelectronic devices and spin-based components, since their lattices may present Mn magnetic ions substituting a fraction of the cations of the original III-V binary compound, which was found to induce local magnetic moment [57]. In such scenario it is crucial to know the density of substitutional and interstitial Mn ions on a given InAs lattice. Mn atoms are expected to modify band structure properties, since interstitial Mn atoms are double donors, reducing the hole density [46,56,58-60].

Many previous works have been done on nanostructures based on Ga(Mn)As in order to search potentially interesting properties for spintronics applications [45,53,61]. It is known that substitutional Mn does not changes the GaAs lattice drastically, in contrast with when it is located in one of the two possible interstitial sites [46,50,58]. X-ray diffraction was used to quantify both the total concentration of Mn atoms on the GaAs lattice and the new lattice parameter after incorporation [59,61,62]. It is known that isolated interstitial Mn atoms reduce the availability of holes in GaMnAs system [63]. On the other hand, substitutional Mn atoms produce holes that are able to compensate such effect. Since each allocation site impacts on ferromagnetic properties for these structures, it has been reported that ferromagnetism is still observable for some configurations of ternary alloys [63-65].

In this work we have grown In(Mn)As islands through molecular beam epitaxy (MBE) on GaAs(001) substrates. The amount of Mn co-deposited with In and As is varied, leading to distinct Mn incorporation conditions. Resonant (anomalous) synchrotron X-ray diffraction was employed here to provide unambiguously the amount of Mn atoms that enter the islands within each type of lattice site. A threshold for interstitial incorporation of Mn was found, followed by the filling of substitutional sites as the relative Mn/In deposition ratio increases. Density Functional Theory (DFT) calculations are employed to address energetic and electronic aspects of Mn incorporation into the InAs lattice.

4.2 Samples and techniques

The samples studied in this work consist of InMnAs islands grown on semi-insulating GaAs (001) substrates by MBE using a RIBER 32P solid-source apparatus over a high temperature (HT). After oxide desorption a 300 nm GaAs buffer layer was deposited at 580ºC. After the HT GaAs buffer growth, the temperature was lowered to

350 °C under a constant As_4 flux. The $In_{1-x}Mn_xAs$ QDs growth follows the usual strained epitaxy within the Stranski-Krastanov growth mode. First, one monolayer (ML) of InAs was deposited and, without any growth interruption, a 2.4 ML of $In_{1-x}Mn_xAs$ following the Mn-free material, with x = 0, 0.22, and 0.35 were grown under 420ºC. The two dimensional (2D) to tridimensional (3D) transition takes place at 1.6 ML, with a growth rate set to 0.06 ML/s, using the nominal InAs rate as the reference. The resulting islands were then annealed during 40 s under As_4 flux, which was subsequently interrupted during temperature quench. The $In_{1-x}Mn_xAs$ islands were left uncapped in all samples. The evolution of all processes of the island formation was monitored in-situ by reflection high-energy electron diffraction (RHEED). The nominal In:Mn growth ratio was determined by the In/Mn flux rate. Sample A has a 22% nominal Mn composition, while Sample B was grown with 35% nominal Mn. A pure InAs sample, called Sample Ref, was also studied. A sketch of the growth of samples A and B is shown in figure 4.1(a).

Atomic Force Microscopy (AFM) topography maps were acquired for each sample. The topography of the samples containing Mn is shown in Figs. 4.1(b-c), for the lower and higher Mn concentration, respectively. One observes that the islands density is higher in sample A ($1.1x10^{12}$ islands/cm^2), but structures are bigger on sample B (density $4.0x10^{11}$ islands/cm^2). For both samples the average islands height was found to be of 5.0 nm, with average diameters of 10 nm (sample A) and 18 nm (sample B).

The anomalous X-ray experiments were carried out at grazing-incidence diffraction (GID) geometry, mapping the vicinity of the GaAs (200) and (400) reflections at XDS and XRD2 beamlines of the Brazilian Synchrotron Light Laboratory (LNLS). Three different energies used were 6.440 keV, 6.534 keV and 6.640 keV (the Mn K-edge is located at 6.5377 keV). The experiment was performed using a fixed incident angle of 0.4º, slightly below the critical angle of total external reflection. The scattered photons were detected using a Pilatus 100 K detector, which integrates a 2º exit angle. Performing anomalous diffraction in diffuse scattering peaks from self-assembled islands allows the extraction of the atomic content as a function of the local lattice parameter along the lattice gradient observed in these nano-object. This technique was used in Si:Ge [66,67] and III-V semiconductor islands [68], thin films [59,69] and other systems [70], allowing a concentration sensitivity of 0.5% to few % in atomic content, depending on the measurement system (synchrotron source and beamline).

Finally, we have also carried out a systematic search for segregated MnAs clusters. No intensity from this binary compound was found at the eight most intense X-ray reflections, indicating that formation (and segregation) of MnAs most likely does not occur.

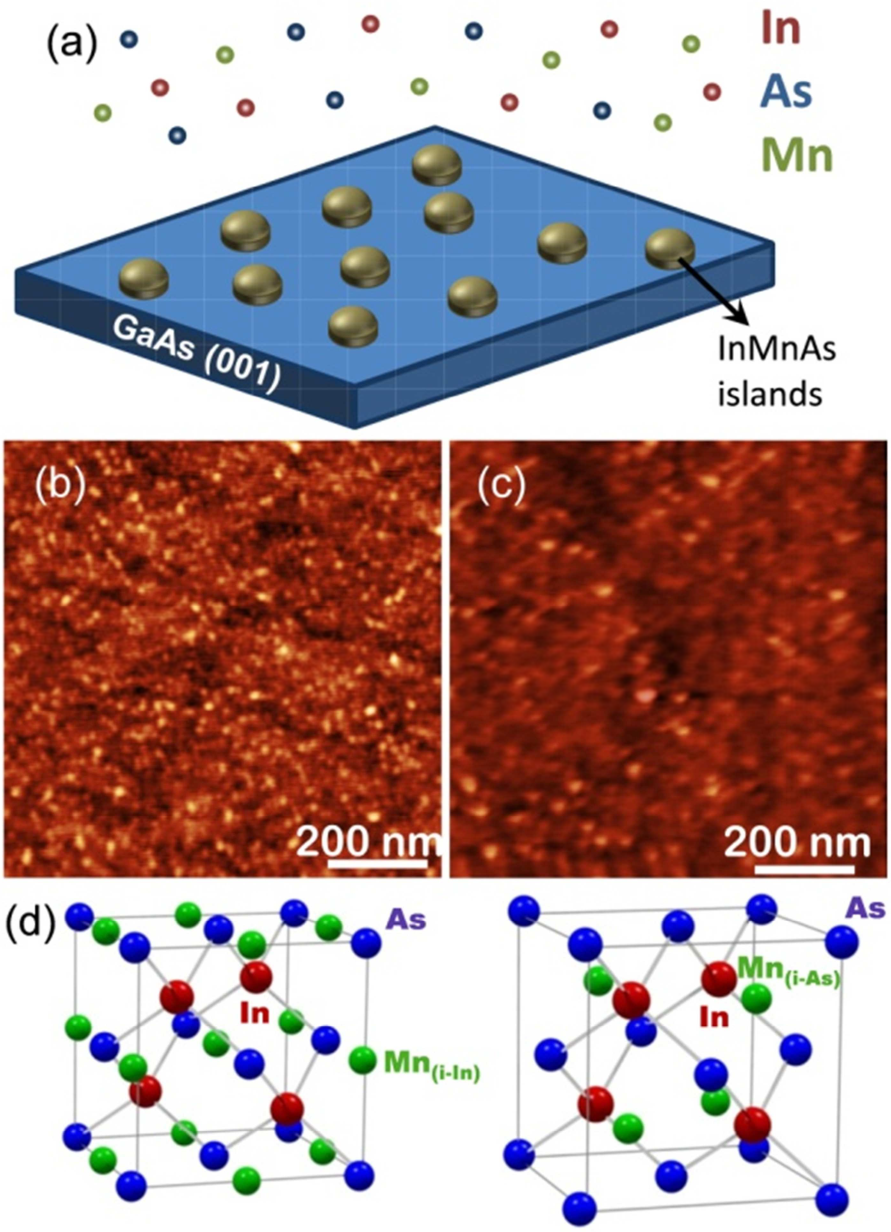

Fig. 4.1 – (a) Representation of the In/Mn/As co-deposition during MBE growth of In(Mn)As self-assembled islands. Atomic force microscopy topographic images are shown in (b) and (c) for samples with nominal Mn composition of 22% and 35%, respectively. (d) InAs lattice unit cell (blue and red atoms) with additional green atoms representing the Mn incorporation at interstitial sites, hereafter names In-interstitial (i-In) and Arsenic interstitial (i-As).

4.3 Resonant X-ray diffraction results

Previous works have indirectly pointed out to the incorporation of Mn atoms at the InAs lattice by measuring the center of mass of diffuse X-ray diffraction near the expected InAs peak position [20,71]. The observed lattice contraction, which evidenced the presence of Mn atoms, could not be used to quantify the amount of this atomic species incorporated into the islands. In order to quantitatively clarify this question one must derive structure factors for X-ray/electron diffraction, finding out which reflections provide the best contrast.

Similarly to the GaMnAs case, Mn atoms can replace In atoms in the main lattice (substitutional sites), but also enter in interstitial sites, which form new face-centered cubic (FCC) lattices displaced from the In/As original ones. These new lattices are placed at positions which correspond to a displacement of (-1/8, -1/8, -1/8) with respect to the In lattice, constituting the In-interstitial sites (i-In); and at (-1/8, -1/8, -1/8) from the As lattice, constituting the As-interstitial sites (i-As) [59]. These two interstitial lattices are represented in figure 4.1(d) as green dots. Finally, the replacement of As atoms by Mn atoms is energetically unfavorable and was not observed experimentally in both InMnAs and GaMnAs compounds [46].

The quantification of the Mn concentration for each site can be carried out by exploring the structure factor dependency of fundamental and superstructure reflections using X-ray energies near the Mn-K edge. For fundamental (strong) reflections such as (220), (400) and (620), the scattered intensity I^{fund} calculated for the unit cell with both interstitial sides is given by [59]

$$I^{fund} = I_0 |f_{In} + f_{As} + C_s(f_{Mn} - f_{In}) + f_{Mn}(C_{i-As} + C_{i-In})|^2, \qquad (4.1)$$

where I_0 is a constant that depends on setup parameters (incident photon flux, illumination footprint, etc…) and C_s, C_{i-As} and C_{i-In} are the concentration of the substitutional and both interstitial Mn sites, respectively, and f_{In}, f_{As}, f_{Mn} are the atomic scattering factors of In, As and Mn. Some of the plus signs of equation (4.1) are replaced by minus signs in the scattered intensity I^{sup} of superstructure reflections such as (200) and (420), which is then given by

$$I^{sup} = I_0 |f_{In} - f_{As} + C_s(f_{Mn} - f_{In}) + f_{Mn}(C_{i-As} - C_{i-In})|^2. \tag{4.2}$$

For X-ray energies that are near an absorption edge of a specific element (anomalous conditions) the dispersion (*f'*) and absorption (*f''*) factors of the atomic scattering factor change drastically, as shown in fig. 4.2(a). The quantitative results for *f'* and *f''* shown in this figure are retrieved by measuring fluorescence within an energy range that comprises the Mn K-edge and performing a Kramers-Kronig calculation, according to ref. [71]. Measuring diffraction in selected energies near the Mn K-edge allows for distinct scattering responses from each possible site in the InMnAs structure. Making use of two reflections (a fundamental and a superstructure reflections) it is possible to retrieve the Mn content for each of the three Mn sites discussed previously.

A first glimpse of the effect of adding Mn atoms to the diffraction of In(Mn)As islands in non-resonant and resonant conditions is shown by the longitudinal scans of Figs. 4.2(b-d). In these figures the reciprocal space position near the GaAs (200) reflection was directly converted into local lattice parameter. One observes that besides the GaAs narrow peak a diffuse scattering arises, due to the In(Mn)As lattice of the islands. From fig. 4.2(b) one observes that the addition of Mn atoms shift the diffuse hump of island diffraction – which has a peak at 6.00 Å for the reference InAs sample – towards slightly smaller lattice parameter values (5.99 Å for sample A and 5.98 Å for sample B). This indirect evidence of Mn incorporation is better understood at anomalous conditions. Figures 4.2(c) and 4.2(d) show longitudinal scans for samples A and B at the three distinct photon energies.

Intensity contrast dependency on the photon energy is well observed for sample A but not clearly seen for similar measurements on sample B. The poor contrast in this latter case [fig. 4.2(d), sample B] could, in a quick observation, lead to the conclusion that Mn is not being incorporated at the InAs lattice, since the presence of Mn atoms in one of the described sites is enough to generate anomalous intensity variations. From equation (4.2) one perceives that the term related to substitutional Mn atoms contributes negatively for the measured intensity, as well as the term for the In-interstitial position. However, at the Mn K-edge, the first term (substitutional Mn) becomes more negative, while the second one (i-In) changes its value, approaching zero. The term corresponding to the As-interstitial position is positive and its value reduces at the Mn edge. The interplay between behaviors for each of the three different Mn sites explains why it is possible to find low contrast around the absorption edge, even having considerable amounts of Mn incorporated at the sample.

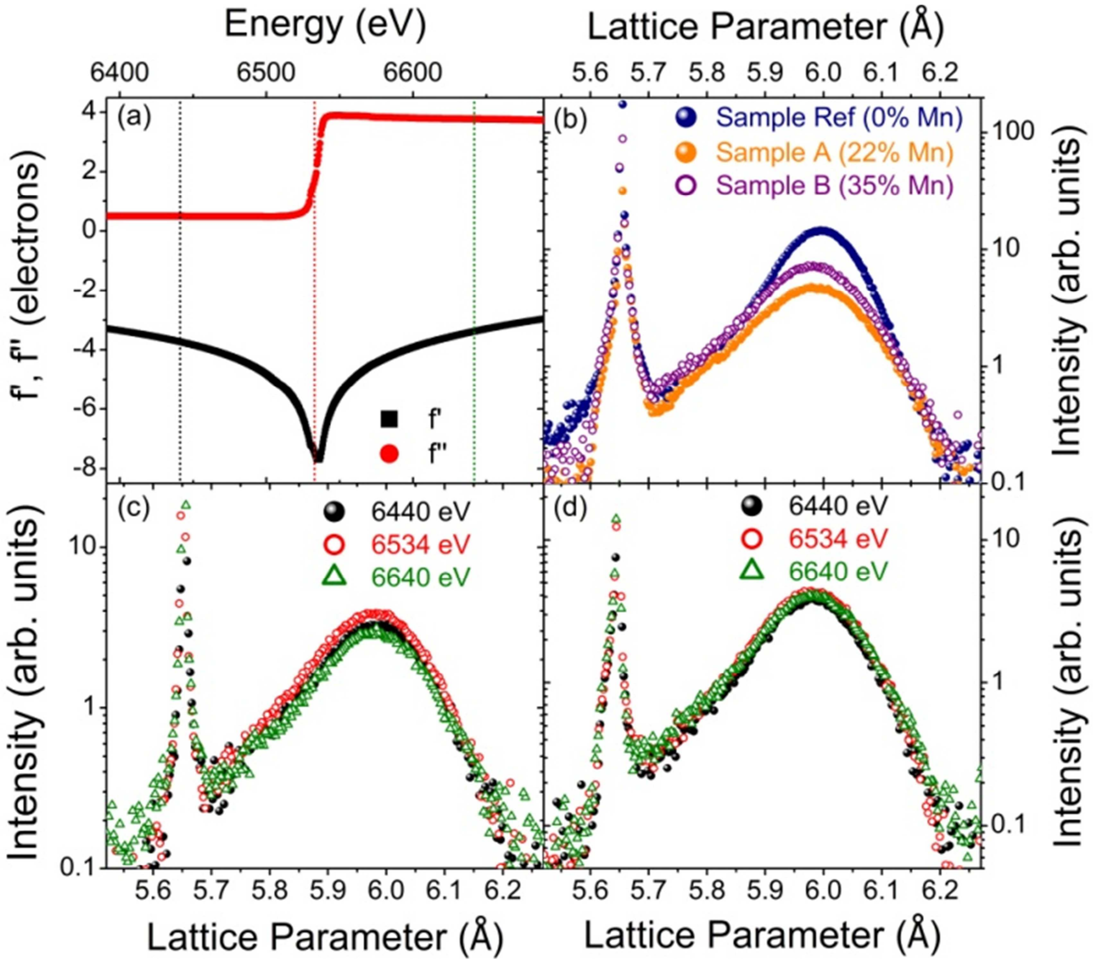

Fig. 4.2 – (a) Dispersion (*f′*) and absorption (*f″*) atomic scattering factor corrections near the Mn K-edge used in this work (measurements/calculations follow ref. [71]). (b) Longitudinal scans near the GaAs (200) in-plane reflection for samples grown with different nominal Mn content. The broad In(Mn)As peak slightly shifts its maximum towards smaller lattice parameter as more Mn is added to the system. From the analysis of its intensity in different energies around the Mn K-edge, shown in the anomalous measurements of panels (c) (sample A) and (d) (sample B), the substitutional Mn concentration and the difference between interstitial concentrations can be found.

4.4 Determination of the Mn concentration

In order to quantify such behavior equations (4.1) and (4.2) are solved as a function of each of the Mn concentration variables and the intensity I_0 (normalization constant) for each of the measured energies. The problem becomes better-determined (and non-ambiguous) with the use of three energies and two reflections. This allows for a fit to the experimental data by varying C_s, $C_{i\text{-}As}$ and $C_{i\text{-}In}$. Some of these fits are shown in figure 4.3 for samples A and B using intensities of the (200) reflection. At this reflection a clear distinction of the substitutional C_s and interstitial difference ($C_{i\text{-}As}$ - $C_{i\text{-}In}$) terms is obtained. One notices that the intensity for selected local lattice parameters in fig. 4.3(a) is larger at energies below the Mn-K edge than at higher energies. This trend is modified for the results of Fig. 4.3(b). While the fits of the first case (sample A) can be carried out by using zero values for C_s and a negative value for ($C_{i\text{-}As}$ - $C_{i\text{-}In}$), both terms must differ from zero in order to fit the data retrieved for sample B. Particularly, we find $C_s = 0$ and $C_{i\text{-}As} - C_{i\text{-}In} = -0.3$ for sample A and $C_s = 0.4$ and $C_{i\text{-}As} - C_{i\text{-}In} = -0.3$ for sample B. These values correspond to the average concentration retrieved for in-plane lattice parameters ranging from 5.95 Å to 6.05 Å.

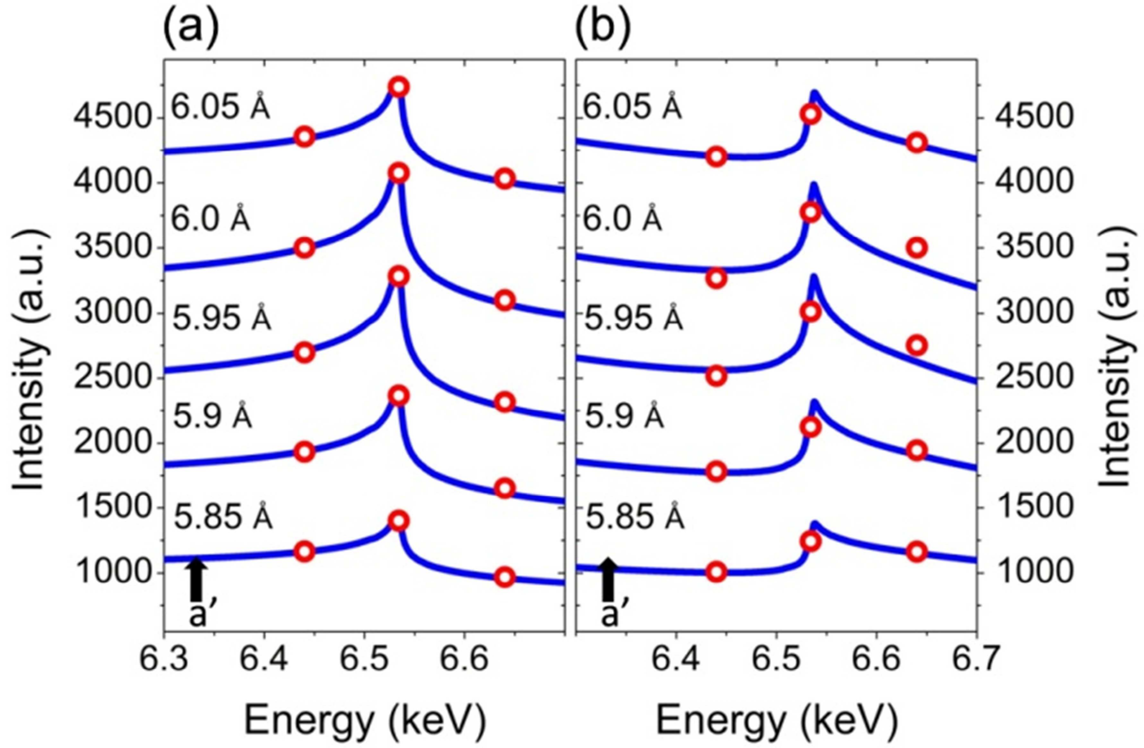

Fig. 4.3 – Fits to the diffracted intensity near the (200) reflection at selected local lattice parameters near the In(Mn)As broad peak for samples (a) A and (b) B. Here we represent the dependency of the scattering intensity with the energy of the incident photons as solid lines, which must fit the experimental data (open dots) retrieved from each of the three energies used.

A removal of ambiguation of the Mn content of each interstitial site is provided by the analysis of the (400) reflection, shown in Fig. 4.4. In the longitudinal scans of fig. 4.4(a) one can observe the anomalous contrast measured at sample B near a' = 5.98 Å as the energy changes near the Mn-K edge. The analysis of such contrast can be quickly performed at this point by fixing the C_s value retrieved at the (200) reflection, as well as the difference ($C_{i\text{-}As}$ - $C_{i\text{-}In}$). In fact, the robustness of our results were also corroborated by leaving the C_s value free to change over the fit procedure, which rapidly converges to the retrieved amount of substitutional Mn from the (200) reflection. Hence, the correct determination of $C_{i\text{-}As}$ and $C_{i\text{-}In}$ is carried out by fitting the intensity profile at each lattice parameter probed along the longitudinal scans for the three energies. One example, for a fixed local lattice with a' = 5.98 Å is shown in fig. 4.4(b). A unique solution is found for $C_{i\text{-}As} = 0$ and $C_{i\text{-}In} = 0.23$. Trial fits with other values which also respect the ($C_{i\text{-}As}$ - $C_{i\text{-}In}$) difference or take into consideration $C_s = 0$ fail in reaching the correct intensity values for the measured energies. After the refinement of compositions using the (200) reflection as a reference condition to the (400) refinement, we have performed a co-refinement of all data. The composition retrieved was the same, which supports the robustness of the method used. The fitting procedure along all measured local lattice parameters and the three energies was carried out for samples A and B. The final composition at the In(Mn)As islands is depicted in Fig. 4.5.

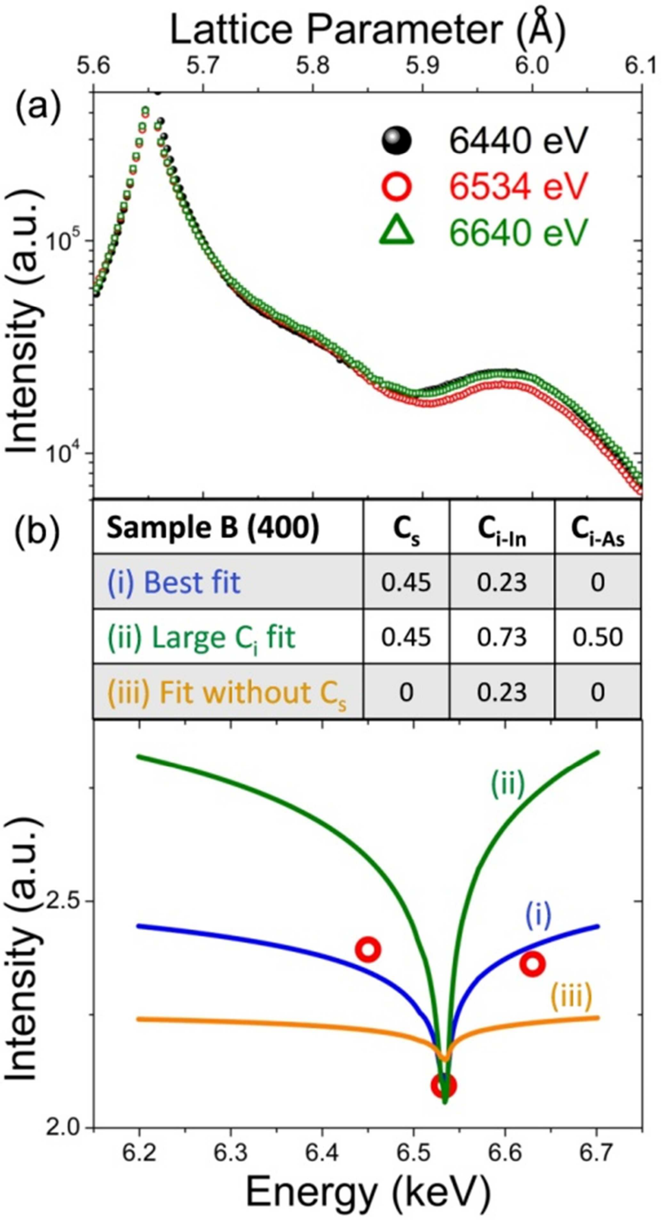

Sample B (400)	C_s	$C_{i\text{-}In}$	$C_{i\text{-}As}$
(i) Best fit	0.45	0.23	0
(ii) Large C_i fit	0.45	0.73	0.50
(iii) Fit without C_s	0	0.23	0

Fig. 4.4 – (a) Longitudinal scans carried out on sample B near the GaAs (400) reflection, using three different energies for the incident photons. (b) Quantitative results from fits with different combinations of C_s, $C_{i\text{-}In}$ and $C_{i\text{-}As}$, shown in (c), for the experimental data retrieved from the curves shown in panel (a) for a' = 5.98 Å. The distinct possibilities explored in this figure represent graphically the uniqueness of the solution of C_i and C_s values, providing the specific Mn content on the interstitial In and As sites, which were entangled in the results from the (200) reflection. The use of large values of C_i [still respecting the difference obtained from the (200) data], or a different C_s do not fit the experimental results.

Once the best parameters are calculated using both (200) and (400) reflections it is possible to separate unambiguously the percentage of Mn allocated at each of the two possible interstitial sites and the substitutional one, for the lattice parameters along the In(Mn)As peak. Our results show that for sample A almost no Mn atoms substitute the In in the lattice, and only in the In-interstitial site an amount of about 35% is occupied. A different scenario is observed for sample B where, still, the As-interstitial site remains unoccupied (zero Mn concentration) and the In-interstitial, presenting the same 35% occupation observed in sample A. However, at sample B the substitutional Mn concentration is much larger, reaching 45% replacement of the original In lattice sites. These results are depicted in fig. 4.5(a), showing the distinct amount of substitutional Mn found for the samples with 22% (A) and 35% (B) nominal Mn concentration. Figs. 4.5(b-c) show for samples A and B, respectively, the amount of In-interstitial sites and As-interstitial sites occupied by the Mn atoms. The similarities of these figures suggest that the Mn starts to fill the In-interstitial sites until a saturation threshold is reached. After such saturation limit the substitutional sites, which probably present a higher activation barrier, become the favorable target for the incoming Mn atoms. The As-interstitial sites occupation seem to be highly unfavorable, indicating that due to its expected chemical coordination a much larger energy barrier needs to be overcome in order to place Mn atoms there.

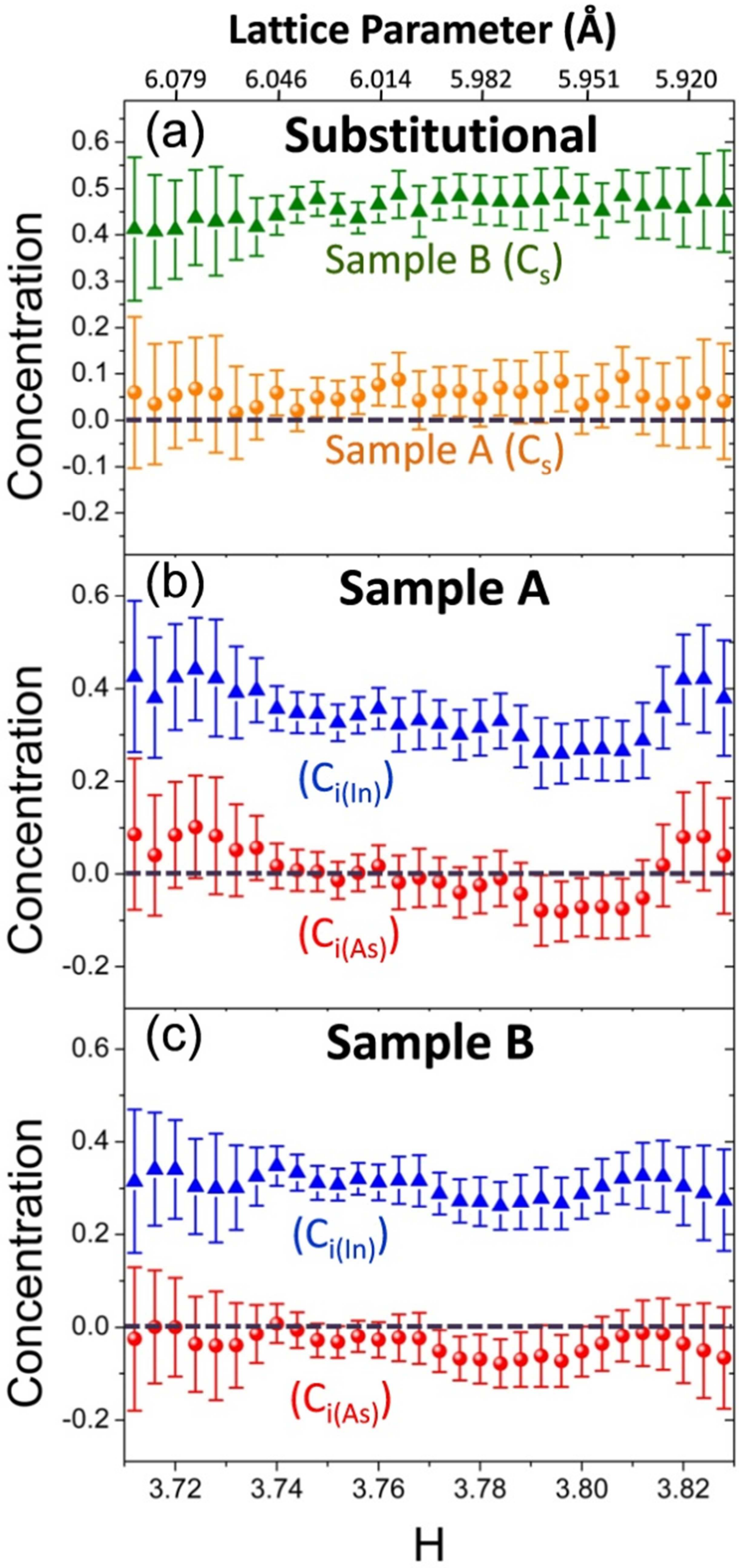

Fig. 4.5 – Mn concentrations for samples A and B retrieved at the vicinity of the In(Mn)As peak for substitutional Mn (a) and the In-interstitial and the As-interstitial sites for samples A [panel (b)] and B [panel (c)].

4.5 Electronic structure

A theoretical analysis of this issue was performed by means of spin Density Functional Theory [72,73] (DFT) within the SIESTA implementation [74], which includes the use of norm-conserving Troullier-Martins pseudopotentials [75] in the Kleinman-Bylander factorized form [76] and a numerical basis set composed of finite range pseudo atomic orbitals. The generalized gradient approximation (GGA) with the rev-PBE [77] parametrization was chosen to determine the exchange correlation functional. All coordinates in our geometric models were relaxed until the maximum force component in each atom was less than 0.026 eV/Å. Using this analysis we address the energetic aspects of the Mn incorporation into the InAs structure as well as the electronic structure of the resulting doped compound.

An atomistic description of an InAs-Mn island with 10 nm of diameter and 5.0 nm of height is not affordable within an *ab initio* scheme. However, since we are seeking general trends rather than a quantitative analysis, we adopted a simplified model based on an initial cubic InAs supercell comprising 64 atoms (two replications of the primitive cell in each direction). The pseudomorphic out-of plane lattice expansion observed at the islands, which is found to be near 10% (with respect to the GaAs lattice) as shown by the out-of-plane (002) X-ray reflection depicted in fig. 4.6(a), was also considered for the calculations. Figure 4.6(b) shows the In(Mn)As supercell, in which periodic boundary conditions were imposed in the three directions. The lengths of the lattice vectors in the *x*, *y* and *z* directions were fixed in 12, 12, and 12.93 Å (15% expansion with respect to GaAs), respectively, to mimic the measured dimensions in our experiments. As an example, the middle and lower panels of Fig. 4.6(b) shows the initial and final geometries, respectively, for 8 interstitial Mn atoms randomly placed into the InAs matrix.

We begin our discussion with the energetic aspects involved in the doping process. It is well established in previous theoretical works that a single Mn atom incorporates preferably in an In substitutional site. For instance, it has been reported [78] a formation energy difference of 1.11 eV favoring it with respect to an interstitial site in which the Mn is first neighbor to four As atoms. It is therefore intriguing why we observe a large amount (35% of available sites) of interstitial Mn atoms in both A and B samples. Even more intriguing, it is the i-In site, which is 0.48 eV less favorable compared to the i-As site according to our total energy calcuations for a single Mn interstitial, the one observed in our experiments.

Interestingly, our theoretical results suggest a trend which may be related to this phenomenology. Using the models previously mentioned, we performed DFT calculations to determine formation energies for structures containing n = 1, 2, 4 and 8 Mn atoms, with Mn atoms placed in randomly chosen sites, according to the expressions (4.3) and (4.4):

$$(E_F)_{int} = E_T(InAsMn_n) - E_T(InAs) - n\mu_{Mn}, \tag{4.3}$$

$$(E_F)_{sub} = E_T(InAsMn_n) + n\mu_{In} - E_T(InAs) - n\mu_{Mn}, \tag{4.4}$$

in which E_T is the total energy directly derived from the bulk DFT calculation, μ_{Mn} and μ_{In} are the chemical potentials for Mn and In, respectively. The relevant quantity in our reasoning is the difference per number of Mn atoms (n) between the formation energies in interstitial and substitutional configurations, $\Delta E_F /n$, shown in expression (4.5):

$$\frac{\Delta E_F}{n} = \frac{(E_T)_{int} - (E_T)_{sub}}{n} - \mu_{In}, \tag{4.5}$$

in which μ_{In} is determined from a bulk In calculation in a body centered tetragonal (bct) phase.

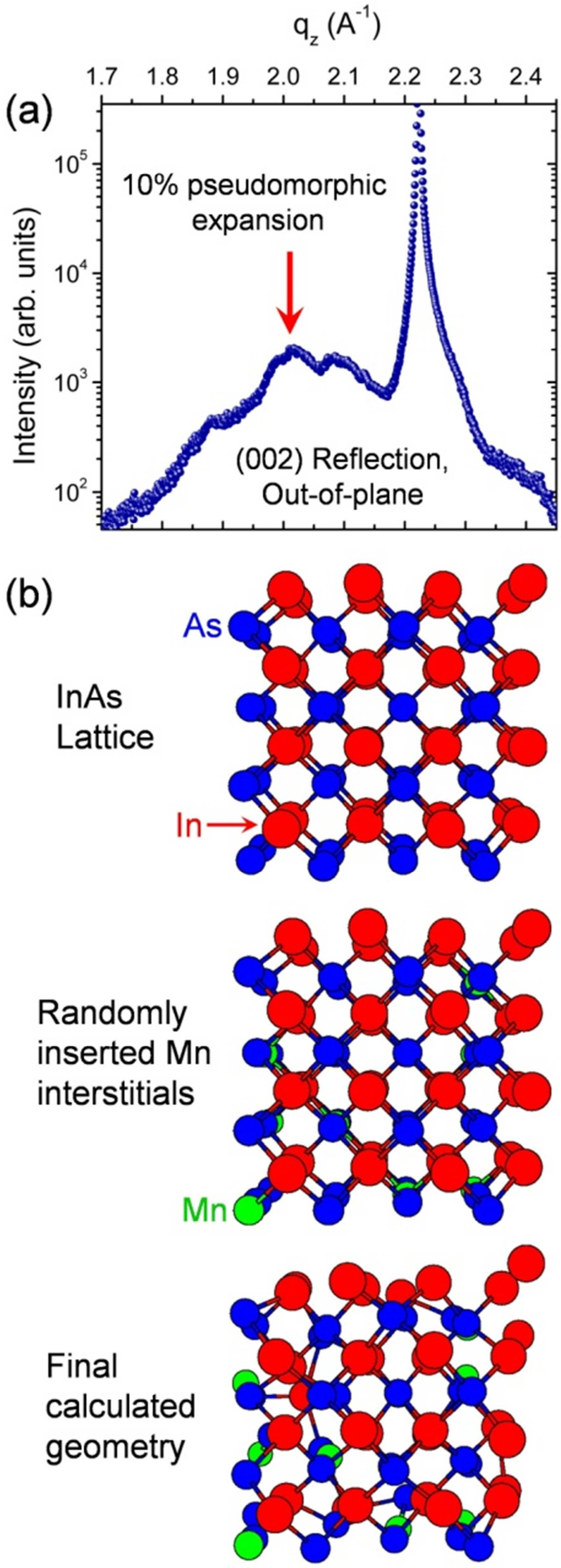

Fig. 4.6 – (a) Longitudinal scan near the GaAs X-ray (002) reflection (sharp peak at q_z = 2.22 Å^{-1}), showing the diffuse scattering from the InAs islands of sample B (centered at a lattice parameter 10% larger than the GaAs lattice) (b) Geometric model for a InAs supercell with 2 replications in each direction, without Mn (upper panel) and at the initial and final states with Mn doping the interstitial sites (middle and lower panel, respectively). Blue, red and green spheres represent As, In and Mn atoms, respectively.

The results, depicted in Fig. 4.7(a), show a monotonic decreasing behavior of the energetic cost associated with the formation of interstitial structures compared to substitutional ones. The choice of In chemical potential is not unique, which means that we cannot pinpoint what value of n is related to a sign change in $\Delta E_F/n$. Also, it was not our goal to find the lowest energy configurations for each n, which would be a formidable task beyond the scope of the present work. However, the calculations can definitely establish that the stability of interstitial doping increases with the number of Mn atoms: indeed, Fig. 4.7(a) shows that from $n = 1$ to $n = 8$ the lower bound for energetic gain for doping in interstitial sites in comparison with the substitutional case is at least 0.78 eV, a result that may be ascribed to structural relaxations originated from local distortions, as it can be seen in Fig. 4.6(b), and the enhancement of Mn-Mn interactions. It is still important to address the problem of the relative stability between the two distinct interstitial configurations, since, as mentioned before, the i-As site for a single Mn leads to a structure 0.48 eV lower in energy. To check if this result is preserved for a large amount of Mn atoms, we performed an additional calculation for 8 Mn atoms placed in i-As interstitial sites. The restrived result indicates an inversion: in this condition it is the i-In structure which is lower in energy, with a calculated total energy difference of 0.30 eV. Therefore, we once more detected an energetic trend favoring i-In interstitial Mn incorporation for large Mn amounts.

Concerning the electronic properties, we found that the incorporation of Mn atoms in the concentrations considered in the present work tends to close the energy gap in our bulk doping models. This is evident in the electronic band structure shown in Fig. 4.7(b) for a single interstitial Mn (i-In site) in the 2x2x2 InAs supercell. Similar features are present in the calculations for $n = 2$, 4 and 8 Mn atoms. The absence of bandgap with the inclusion of Mn atoms is in agreement with the lack of photoluminescence observed in capped In(Mn)As quantum dot samples.

Finally, although a clear contrast is observed between DFT calculations and the retrieved Mn content from anomalous diffraction results a more complete qualitative scenario has to be established on the basis of growth conditions. DFT calculations are based in thermal equilibrium conditions, which do not take into account the surface kinetic mechanisms of Mn incorporation into InAs islands. Such process, which takes place far from the thermodynamic equilibrium during the MBE growth of islands, is probably responsible for the rich Mn content on In-interstitial sites. The contact between experiments and the simulation framework explored here is found on the increasingly lower energy of additional Mn atoms at the In-interstitial sites as the Mn content becomes larger in such condition. We believe the used growth dynamics allows a sufficient supply of Mn atoms that are incorporated in In-interstitial sites at a large rate, probably due to surface strain or surface-driven processes, helping to reduce activation barriers and the final overall system energy to a point where this type of incorporation is stabilized.

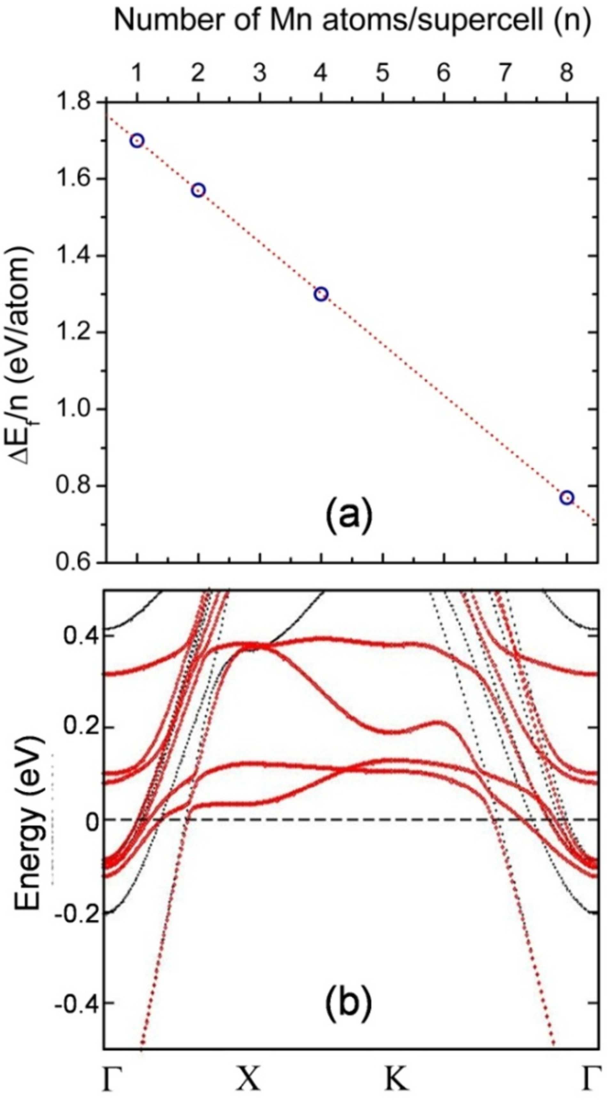

Fig. 4.7 – (a) Difference in formation energy of In(Mn)As per Mn atom (*n*) between intestitial and substitutional doping configurations as a function of *n*. The dotted straight line is a guide to the eyes solely. (b) Electronic band structure for a single Mn atom in the simulated In(Mn)As supercell, placed in an In interstitial (i-In) site. The Fermi level is set to zero, and red and black lines distinguish the two spin components. X and K represent the points (1,0,0) and (1,1,0), respectively, in units of π/a (a = 12 Å).

4.6 Conclusion

Our experimental results using three photon energies near the Mn-K absorption edge and comparing the intensity contrast in fundamental and superstructure X-ray reflections show, unambiguously, that Mn atoms can be incorporated at the InAs lattice of self assembled islands. Interstitial In-sites are initially occupied for low Mn nominal deposition content, while the presence of Mn atoms in substitutional In sites is only detected after a approximately 35% In-interstitial Mn-filling threshold. Such result may be a consequence of the island surface potentials and Mn incorporation kinetic mechanisms, which can be favored by the strain relaxation at the In(Mn)As island surface. DFT simulations were also carried out. Inspite of their inherent thermal equilibrium character, these simulations show that, for increasing Mn content on interstitial In sites, the energy for insertion of additional Mn atoms at other interstitial sites on the resulting deformed lattice decreases.

Chapter 5

Effects of large-miscut Si(001) substrates on strain and interdiffusion in Ge islands: a synchrotron surface resonant X-ray diffraction study

5.1 Motivation

Self-assembled semiconductor nanostructures have been intensively investigated in the past decades. In particular, the interest in obtaining either spatially ordered islands [79,80] and/or with the enhancement of specific crystal facets [81-84] has driven recent interest to the use of substrates with distinct surface conditions [79,85]. It is known that both high crystallographic index oriented substrates as well as the surfaces with crystal steps introduced by a miscut angle affect the growing process at the nanoscale [86,87] and alter the symmetry of the elastic-interaction potential between epitaxial nanostructures [88]. The ability to control optoelectronic properties due to elastic tensor constraints in these structures plays an important role for modern nanoscale engineering

[89-92]. Finally, surface configurations and energies of the vastly studied heteroepitaxial growth of Ge islands on vicinal Si(001) can be also better understood when compared to similar objects grown on substrates with miscut [82,93-95].

On Si(001) substrates, the coverage-dependent evolution of islands shape and size is well understood. There are characteristic transitions from unfaceted prepyramids to {105} faceted SiGe pyramidal huts up to multifaceted domes and superdomes increasing the Ge concentration [96-98]. In this work we study Si/Ge intermixing, as well as the elastic energy stored in the nanostructures, for a set of samples with different nominal Ge coverages (4 ML and 13 ML), located within the vicinal pyramidal and dome/superdome regimes, grown at distinct temperatures (600º C and 730º C). The retrieved information on strain fields, elastic energy and composition (using resonant synchrotron X-ray diffraction) is compared for islands grown on substrates with and without miscut.

5.2 Samples and techniques

The samples studied in this work consist of SiGe islands grown on Si(001)substrates. The islands were grown by physical-vapor deposition of Ge on the singular Si(001) surface and on vicinal substrates misoriented by 6º and 10° towards the [110] direction at T = 600°C and 730°C and at constant flux of 1.8×10^{-3} ML/s. In order to verify the island morphology, scanning tunneling microscopy (STM) measurements were carried out *in situ* by using a scanning tunneling microscope (STM) under ultra high-vacuum conditions ($p < 3 \times 10^{-11}$ torr) [99].

Synchrotron grazing-incidence X-ray diffraction measurements were carried out at the ID01 and BM02 beamlines of the European Synchrotron Radiation Facility (ESRF, Grenoble), as well as at the XRD2 beamline of the Brazilian Synchrotron Light Laboratory (LNLS, Campinas). The experiments were performed using 6-circle (BM02 and XRD2) and 3+2-circles (ID01) diffractometers equipped with area detectors (Maxipix, Pilatus 100K). The incident angle was fixed at the critical angle of total external reflection (0.16°) near 11.103 keV (K-absorption edge of Ge). The diffracted signal was measured over a minimum exit angle range of 1.5°.

Finite Elements Method (FEM) analysis using a commercial software package (COMSOL Multiphysics) was carried out to simulate the displacement and strain fields inside the measured islands, and then to simulate their scattering signal.

Figures 5.1(a) and 5.1(b) display the STM images obtained for the samples with 4 ML of Ge coverage grown at 600°C on a Si(001) substrate without miscut and with 10° miscut, respectively. On the flat substrate (0° miscut), a mixture of {105} faceted pyramids and domes is observed, while for the 10° miscut sample, the growth of the pyramids is hindered by the geometrical constraint of the miscut angle, and instead a wetting layer completely faceted by {105} ripples appears, so the domes and a {105} faceted wetting layer can be found. For the sample with 4 ML coverage and without miscut. the two observed types of islands have different densities: pyramids correspond to 85% of the islands and domes to 15%, resulting in an overall density of 12 x 10^9 islands/cm^2. The average height and lateral size of the domes are (23±6) nm and (110±20) nm, respectively. Conversely, the pyramids are (5±2) nm in height and (50±10) nm in lateral dimension. Only domes are observed on the 10° miscut sample, with a density of 1.8 x 10^9 islands/cm^2, and average height of (15±2) nm and a lateral size of (80±20) nm. Figures 5.1(c) and 5.1(d) show STM images obtained for the samples with 13ML of Ge on 0° and 10° miscut substrates, respectively. One notices that the average length of one of the semiaxis along the [110] direction increases for larger miscut angles. On the other hand, island density is reduced, which indicates that the material deposited is re-distributed among islands. From the images, one can see that the sample with 0° miscut and 13 ML coverage contains nanostructures with an average height of (15±2) nm and a length of (110±20) nm along the longer semiaxis. Instend for the islands on the 10° miscut substrate, a height of (23±6) nm and a length of (190±40) nm (longer semiaxis) are observed. At 13 ML of Ge coverage, 15% of the island population consists of superdomes. The islands density is about 1.7 x 10^9 islands/cm^2 for the flat substrate and 0.9 x 10^9 islands/cm^2 for the substrate with 10° miscut. Figure 5.1(e) displays one isolated dome and one superdome, from the 13 ML sample, evidencing the differences on sizes, specially along the [110] direction.

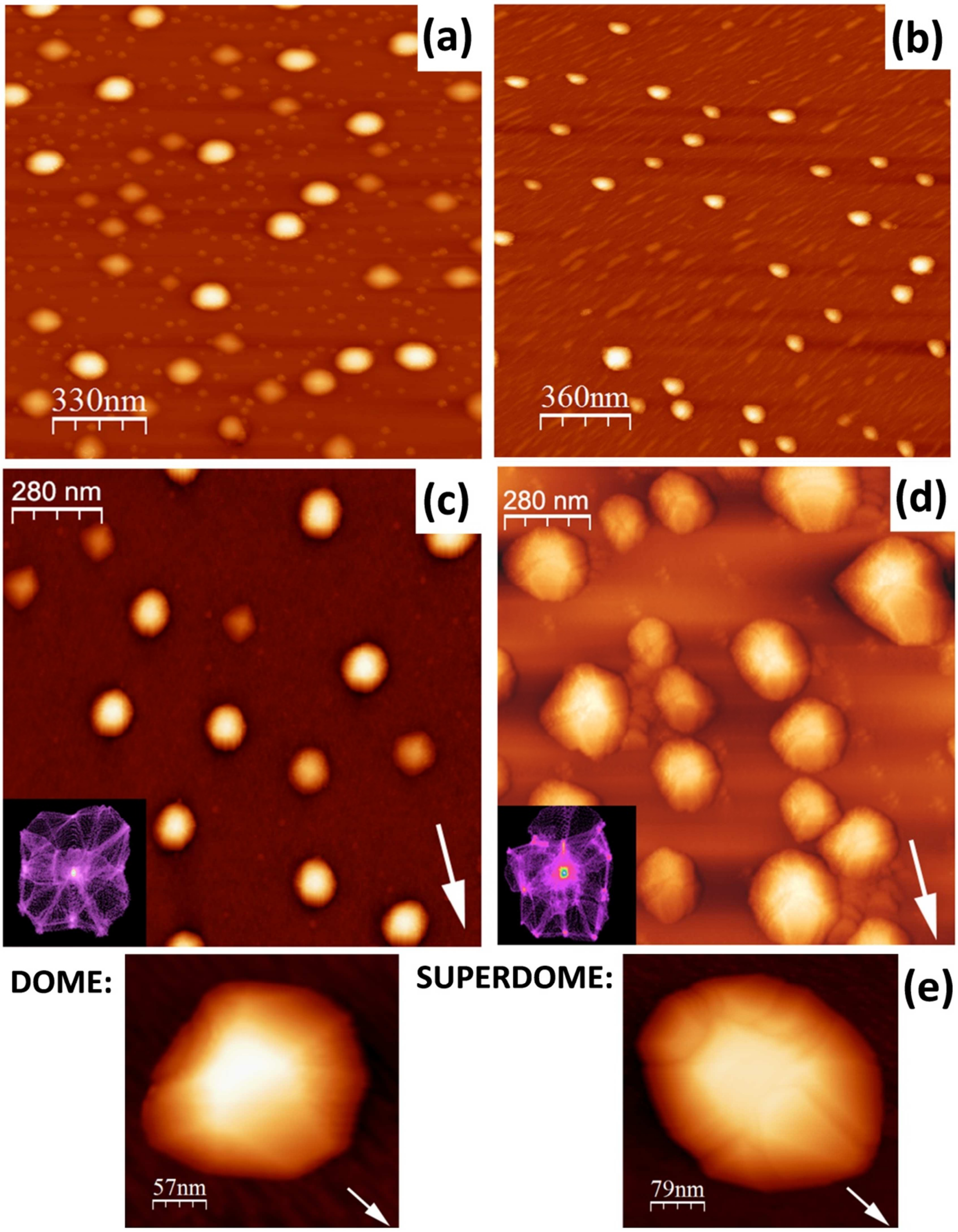

Fig. 5.1 – Scanning Tunneling Microscopy images showing the morphology of islands on the (a) 4ML sample without miscut, (b) 4 ML sample with 10° miscut, (c) 13 ML sample without miscut and (d) 13 ML sample with 10° miscut. All of the images correspond to samples grown at 600°C. The insets show the facets of the structures. It is possible to notice a longer semi-axis along the [110] direction (indicated by arrows in the STM images for the 13 ML samples) for the sample with miscut. Figure (e) shows a zoom for a dome and a superdome from the 13 ML sample, evidencing the stretching on the superdome at the [110] direction.

5.3 Resonant X-ray diffraction results

To seek distinct lattice relaxation responses caused by any strain anisotropy that may take place due to islands shape, surface X-ray measurements along perpendicular directions were performed for the sample with 13 ML of Ge coverage grown at 600°C. Figures 5.2(a) and 5.2(b) show X-ray diffraction longitudinal (radial) profiles along the [220] and [2$\bar{2}$0] directions, respectively. One narrow and intense peak coming from the Si substrate is observed at H = K = 2 (reciprocal lattice units of Si) for each of the two scans. A broad peak extends towards lower values of (H, K), corresponding to larger local lattice parameters. It is attributed to the presence of a gradient of lattice parameter values inside the Ge nanostructures [100]. The intensity signal drop around H, K = 1.945 for both reflections indicates that asymmetries on the strain distribution are not significant comparing both in-plane directions. Nevertheless, the distinct faceting from each direction generates features between H, K = 1.97 and H, K = 1.99.

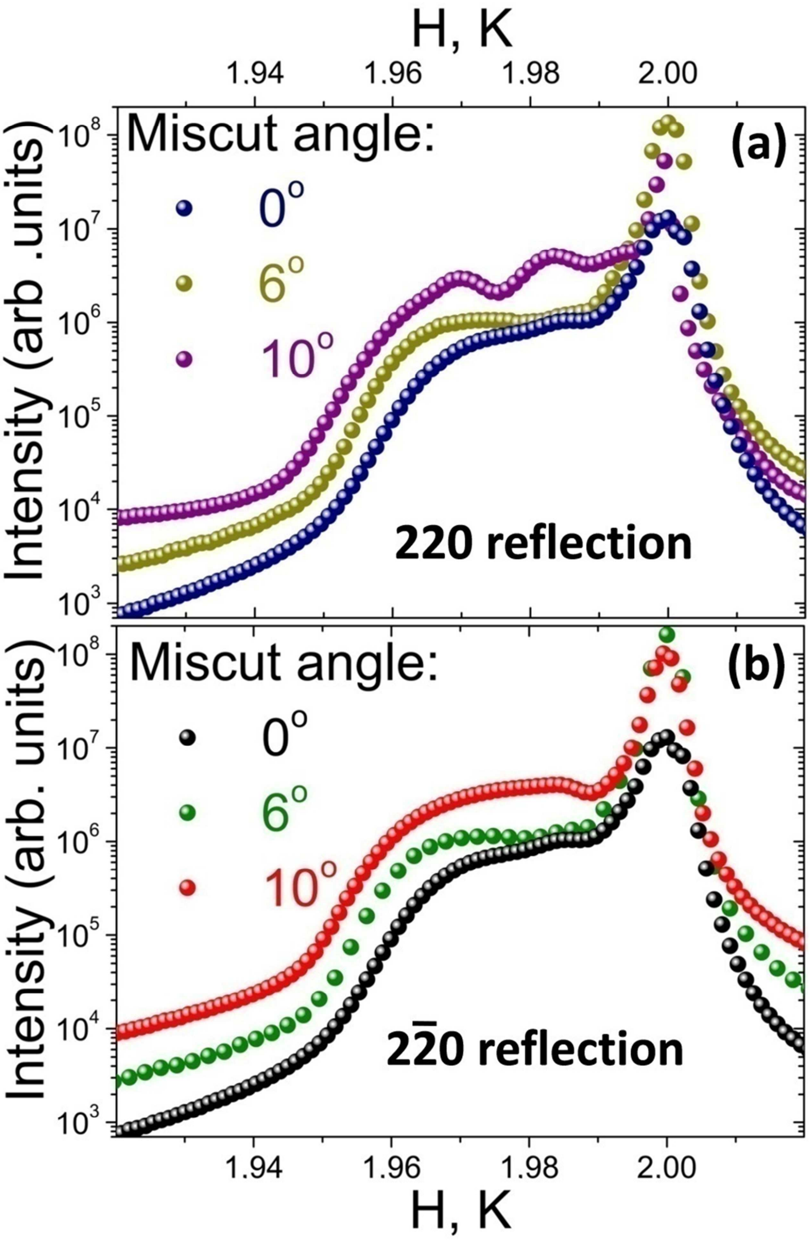

Fig. 5.2 – Longitudinal X-ray diffraction scans near the (a) (220) and (b) (2$\bar{2}$0) reflections for the sample with 13 ML Ge (T_G= 600°C). The presence of features between H, K = 1.97 and H, K = 1.99 indicates distinct faceting from each direction.

Figure 5.3 shows longitudinal scans measured near the **220** Si Bragg peak for the samples containing 4 ML (a) and 13 ML (b) of Ge coverage, grown on Si substrates with 0° and 10° of miscut. The broad intensity distribution observed for the scans corresponding to the samples with 10° miscut reach lower (H, K) values compared to the signal of islands grown on the flat substrate for both 4 and 13 ML. Higher diffracted intensities were also detected at lower (H, K) values, indicating the existence of more material with partially or fully relaxed lattice parameter in these structures. These results suggest that for larger miscut angles, the Ge concentration increases inside islands.

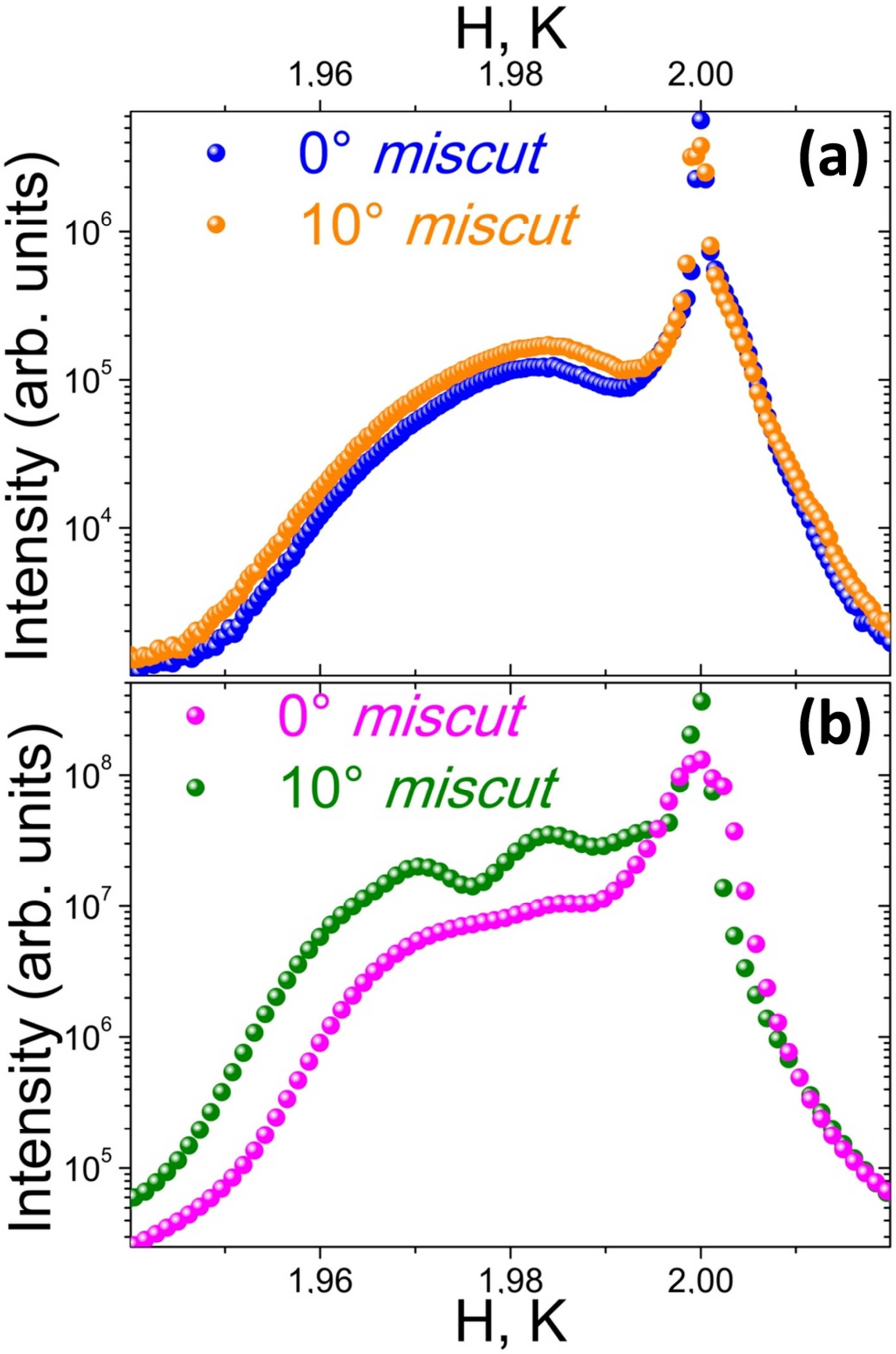

Fig. 5.3 – Longitudinal X-ray diffraction scans are shown for the samples containing (a) 4 ML and (b) 13 ML of Ge coverage grown at 0° and 10° miscut under 600°C. The diffraction peaks corresponding to the islands span a larger range of (H, K) values for the samples with miscut angle, suggesting a larger Ge concentration in the domes and superdomes grown on substrates with miscut.

The Ge composition in all samples was retrieved performing resonant (anomalous) X-ray diffraction measurements. Figure 5.4 shows longitudinal scans for three different photon energies: i) 80 eV below the Ge K absorption edge, ii) 6 eV below the edge, and iii) on resonance with the edge. Panel (a) is referred to the sample grown at 600°C with no miscut, (b) to the sample grown at 730°C with no miscut and (c) to the sample grown at 600°C with 10° miscut for Ge coverage of 4 ML. For all the three samples, it is clear that the diffracted intensity from the domes decreases as the energy gets closer to the edge. This effect is stronger for the samples grown at 600°C, which is consistent with a reduced Si interdiffusion at lower growth temperature, leading, in turns, to domes with larger Ge content. This result is in agreement with the data measured on samples grown at 730°C reported in figure 5.4(b), where narrower peak for the domes indicates a lower Ge concentration, since the observed lattice parameter distribution does not span significantly towards the value of bulk Ge. Differences between the samples grown at 600°C with and without miscut cannot be directly noticed at this point.

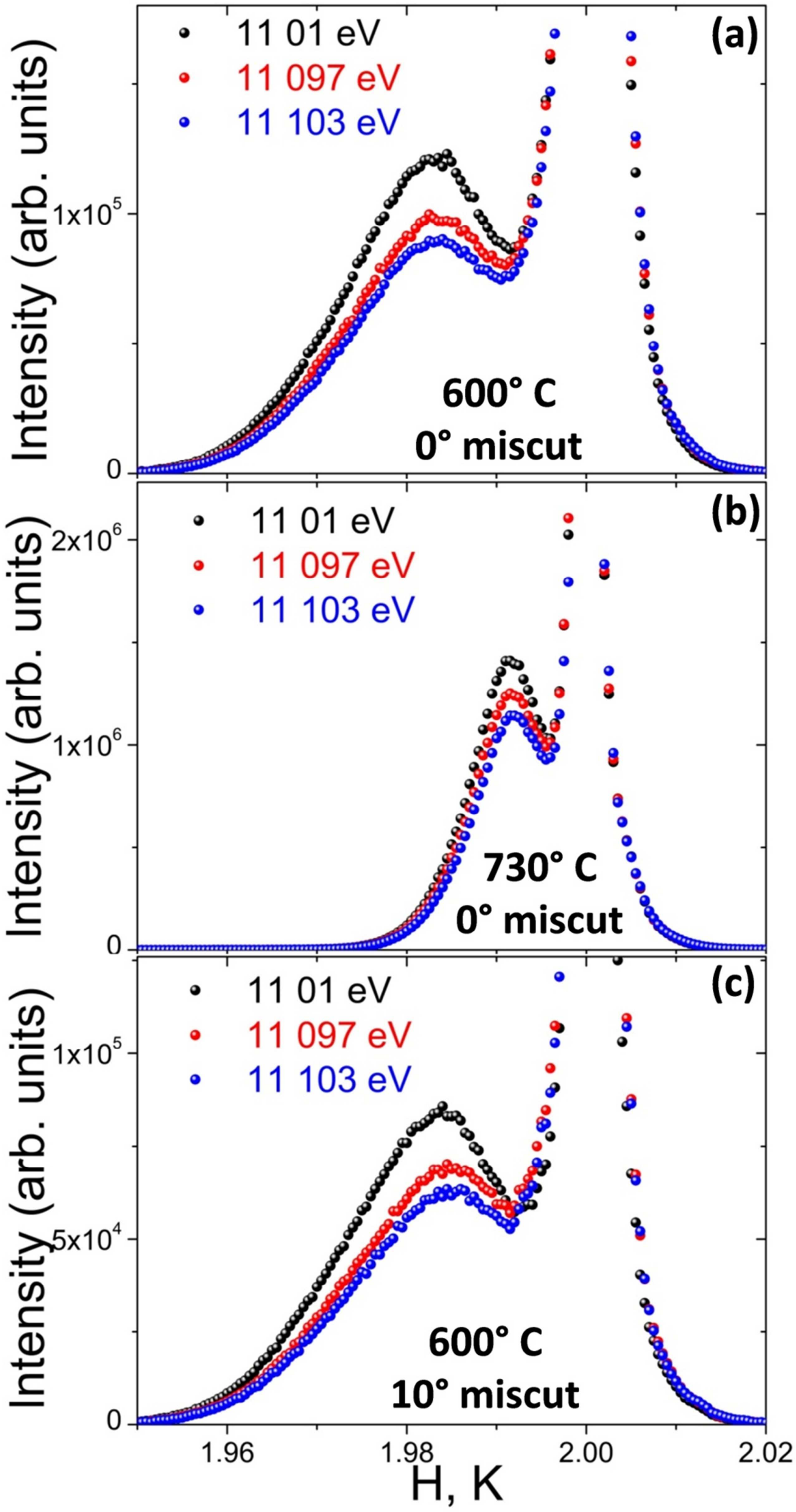

Fig. 5.4 – Resonant X-ray diffraction longitudinal scans performed near the Si **220** Bragg peak for (a) the sample grown at 600°C with no miscut, (b) the sample grown at 730°C with no miscut and (c) the sample grown at 600°C with 10° miscut. All results in this figure refer to 4 ML samples. The photon energies used were: 93 eV below the Ge K absorption edge (black dots), 6 eV below the edge (red dots), and at the Ge-K edge (blue dots).

5.4 Determination of the Ge concentration

The dependency of the intensity of the diffracted beam with the Ge concentration is quantified using equation 5.1 [100,101]:

$$I^{SiGe} = I_0|C_{Ge}f_{Ge} + C_{Si}f_{Si}|^2$$

$$= I_0|C_{Ge}(f_{Ge} - f_{Si}) + f_{Si}|^2 \quad , \qquad (5.1)$$

where I^{SiGe} is the intensity for a given energy, I_0 is a normalization constant that depends on the beam flux, C_{Ge}, C_{Si}, f_{Ge} and f_{Si} are the concentrations and the atomic scattering factors for the Ge and Si, respectively.

Applying equation 5.1 on the resonant X-ray scattering data, we obtain the Ge concentration, since f_{Ge} and f_{Si} are known for a given energy and I^{SiGe} can be retrieved from the measurements, leaving only I_0 and C_{Ge} unknown. Varying the normalization constant and the Ge concentration, with fixed values of scattering factors for each energy, we found the optimal fitting for the variables that matches each calculated I^{SiGe} to the corresponding measured intensities. Minimizing the differences from the theoretical and experimental outputs for the three energies, simultaneously, C_{Ge} becomes unambiguously determined. The procedure was used for different values of (H, K), allowing us to plot the Ge concentration as a function of the in-plane lattice parameter condition, for each of the studied samples. The left panels from figure 5.5 show the Ge concentration results for the samples grown at (a) 600°C (4 ML Ge), (b) 730°C (4 ML Ge) and (c) at 600°C (13 ML Ge), with 0° and 10° miscut for the first two sets of samples and 0° and 6° miscut for the last one. Clearly, the Ge concentration is reduced in the direction where the in-plane lattice parameter moves towards the bulk Si value. For larger lattice parameter values, the local Ge content increases in all cases. One notices that for the 4 ML (600°C) samples, the Ge concentration is larger for islands grown on substrates with miscut, if compared with the flat surfaces. Such result indicates that the island facets, which become larger after growth on substrates with miscut, may present a larger barrier against surface diffusion of Si atoms. This scenario changes when we look at the samples with a deposit of 13 ML of Ge (600°C), where a larger Ge content is retrieved at the flat substrate condition. Such effect indicates that the {111} facets at the base of superdomes (which are present at this coverage) become larger for the substrates with miscut, and are preferential sites for Si diffusion from the substrate [102].

The right panels of figure 5.5 show the elastic energy per atom, displayed as a function of the local lattice parameter for each sample. From figure 5.5(d), it can be noticed that the elastic energy is higher when the miscut substrate is used for the samples grown at 600°C with 4 ML of Ge coverage. The same scenario holds for the samples grown at 730°C (4 ML Ge) and at 600°C (13 ML Ge), as shown in figures 5.5(e) and 5.5(f) respectively, up to large lattice parameters, corresponding to the domes/superdomes regime. The elastic energy assumes values close to 0 when the lattice parameter approaches that of the bulk Si, while it increases for the region corresponding to the islands. This result indicates that the symmetry break introduced by the large island facets on substrates with miscut drives the system away from the usual minimum energy condition [99,103].

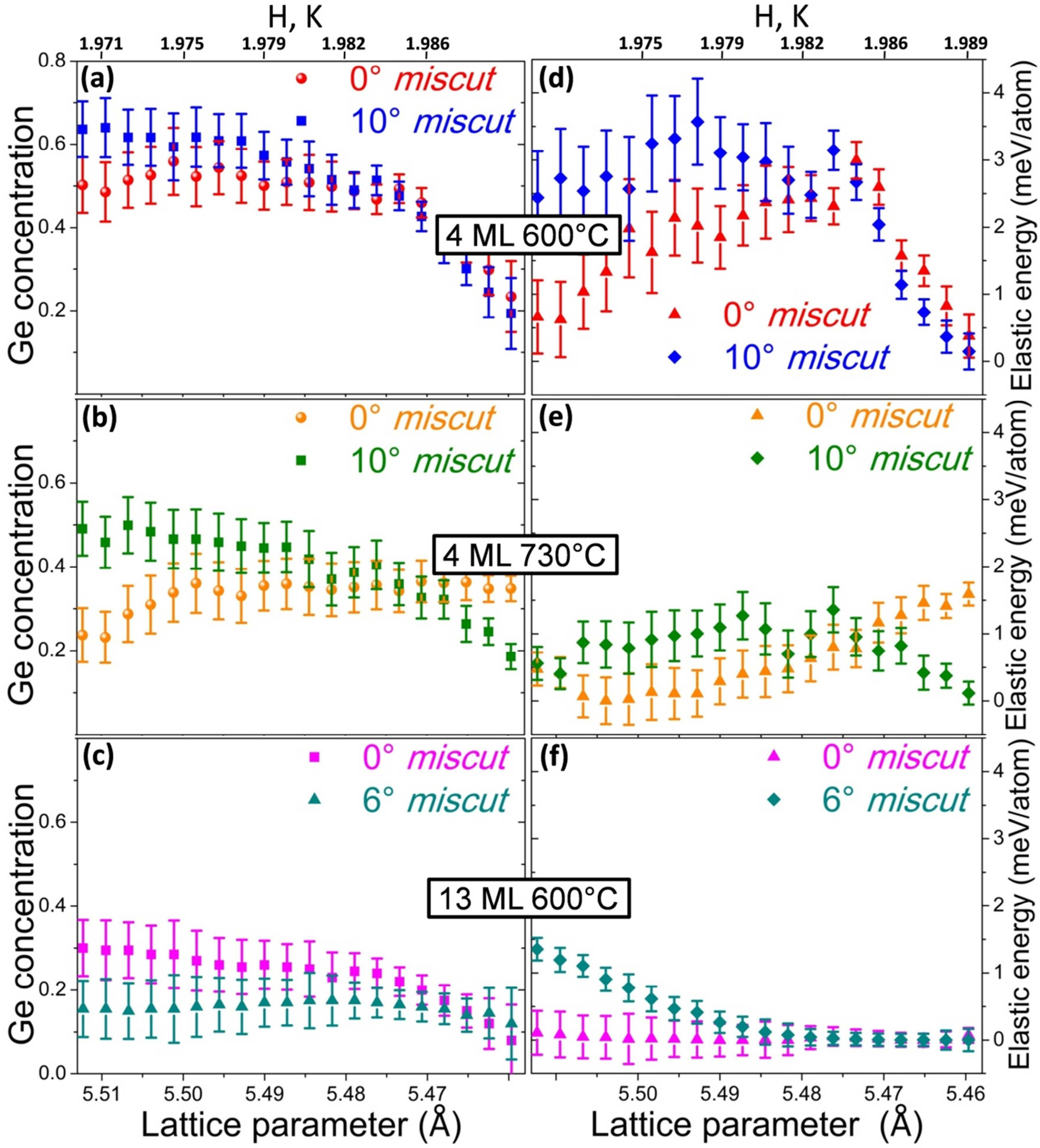

Fig. 5.5 – Ge concentrations for samples grown at (a) 600°C (4 ML Ge), (b) at 730°C (4 ML Ge) and (c) at 600°C (13 ML Ge), with 0° and 10° miscut for the first two sets of samples and 0° and 6° miscut for the set of panel (c). The elastic energy per atom (in meV/atom) is shown for the samples (d) 600°C (4 ML Ge), (e) 730°C (4 ML Ge) and (f) 600°C (13 ML Ge). Higher energies values are generally observed for the samples grown at substrates with miscut.

5.5 Finite Elements Method simulations

Finite Elements Method (FEM) analysis using a commercial software package (COMSOL Multiphysics) was performed to simulate islands with 4ML Ge coverage grown at 600°C. These simulations were carried out to understand whether the broadening of the diffraction peak coming from the Ge islands grown on substrates with and without miscut is due to surface or bulk effects. Figure 5.6(a) shows cross-section images for the two simulated structures, the upper one without miscut and the bottom one with 10° miscut. The colormap shows the displacement ***u*** after relaxation, evidencing the asymmetry of strain distribution on the samples with miscut. A visual comparison of equal-volume islands, such as those depicted in Fig. 5.6(a), is not enough to identify in which island the largest amount of elastic energy is stored. Due to the effect of the asymmetric morphology on the island, variables must be evaluated for the whole volume.

The geometrical asymmetry has, nevertheless, a clear signature on FEM (bulk-like) simulations. For instance, the second principal strain (that depends on the difference of the in-plane directional strains) along a vertical line drawn in the geometrical center of the domes is different for the two geometries. The second principal strain is defined as: $\varepsilon_{II} = \frac{\varepsilon_x+\varepsilon_y}{2} - \frac{1}{2}\sqrt{\left(\varepsilon_x - \varepsilon_y\right)^2 + \gamma_{xy}^2}$, where $\varepsilon_i = \frac{\partial u_i}{\partial i}$ is the derivative of the displacement along the i direction with respect to the same direction and $\gamma_{xy} = \frac{\partial u_y}{\partial x} + \frac{\partial u_x}{\partial y}$ is the shear strain component. The profiles extracted from our simulations are depicted in figure 5.6(b) for both structures along the growth direction (out-of-plane), with and without miscut. The plot again points out a strong strain asymmetry in the 10° miscut sample.

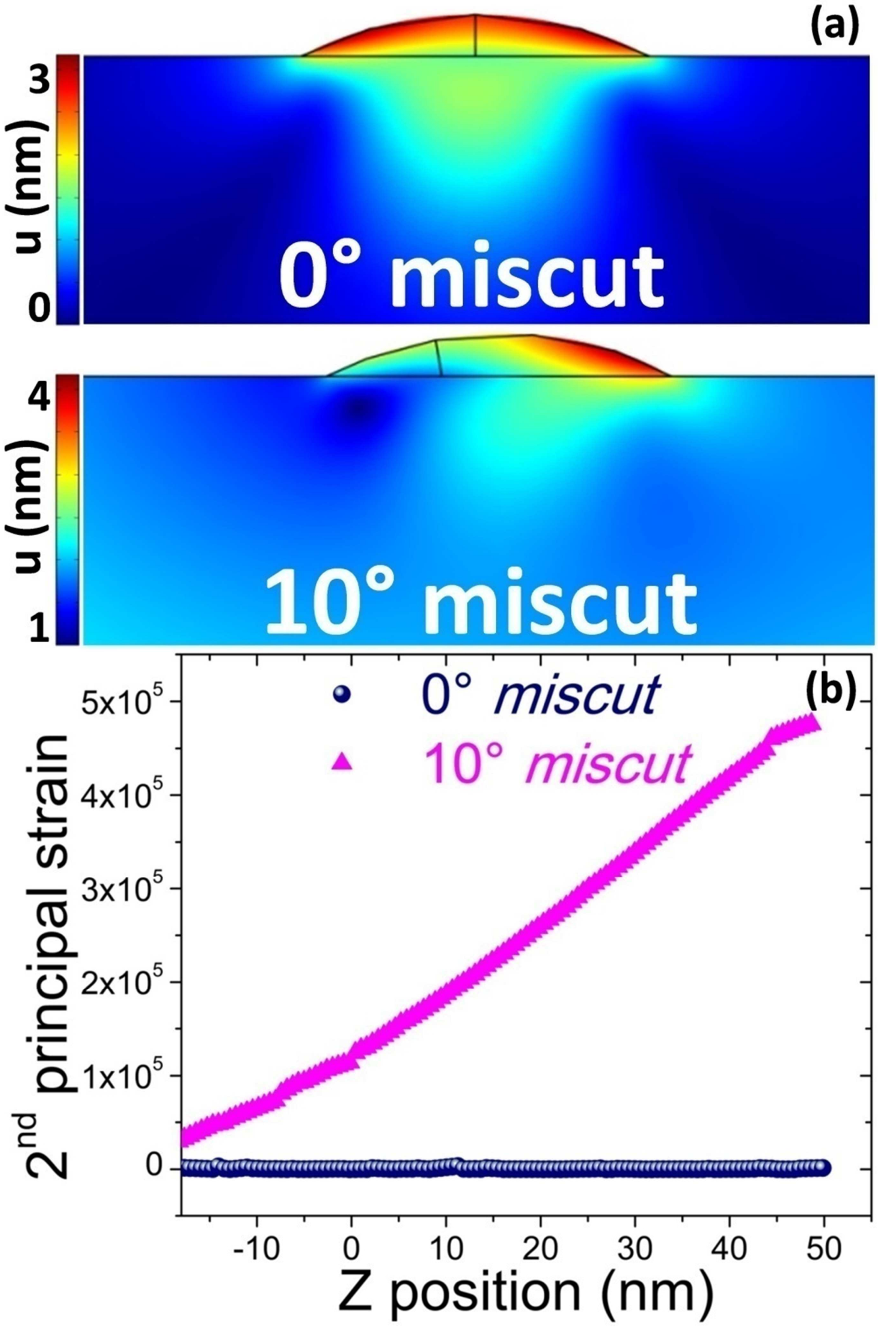

Fig. 5.6 – (a) Cross-section maps for the structures simulated using a Finite Elements Method Simulation commercial software (COMSOL Multiphysics), representing islands with the experimental dimensions of domes with 4 ML Ge coverage grown at 600°C for flat (upper panel) and 10° miscut (bottom panel) substrates. The colormap shows the total displacement ***u*** (sum of in-plane and out-of-plane) after relaxation, evidencing a strain asymmetry on the samples with miscut. Panel (b) shows the second principal strain corresponding for the structures depicted on figure (a) for the elements following a vertical (growth direction) line that passes through the geometrical center of the domes, endorsing the strain asymmetry present on the 10° miscut sample.

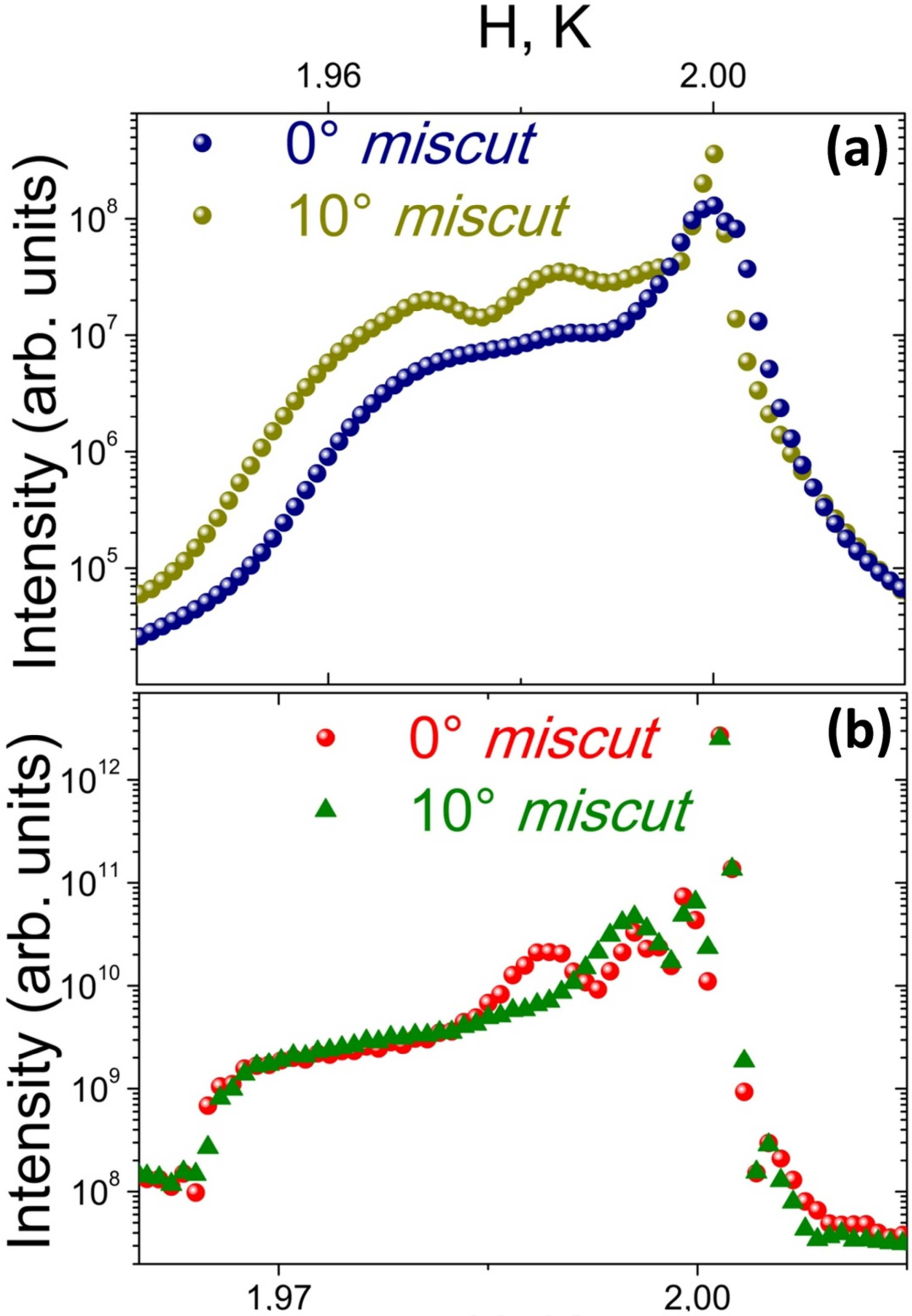

Fig. 5.7 – (a) Experimental data for 0° and 10° miscut samples with 13 ML Ge coverage. (b) Simulated longitudinal X-ray diffraction scans, which indicate that the enlargement of the broad peak observed in the experimental curves [panel (a)] does not arise from the bulk elastic energy configuration.

Longitudinal X-ray diffraction scans on samples with 0° and 10° miscut, shown in figure 5.7(a), show an additional broadening of the diffraction peak of Ge islands in case of non-zero miscut. To check whether the asymmetry observed by FEM simulations in the bulk of the islands is related to the broadening of the island diffraction peak, we simulated the X-ray diffraction radial scans from the FEM structures. The result is shown in figure 5.7(b). The theoretical curves do not exhibit a significant difference for low (H, K) values, indicating that the effect observed in the experiment may not come from the bulk elastic energy, but from the miscut-induced facets, which introduce strain states that cannot be retrieved in the flat substrate systems.

Another series of FEM simulations on iso-volume islands were also analyzed comparing domes with pure Ge content and with a $Si_{0.5}Ge_{0.5}$ alloy ratio. We retrieved the average elastic energy (in meV/atom) for three-dimensional islands simulated with a miscut of 0, 2°, 6° and 10°. The results are shown in figure 5.8 (dotted lines / solid dots), and are compared with those obtained experimentally, displayed as dashed lines/open dots. The size of the marks takes into account the error bar on the vertical axis, while the energy scale (Y-axis) is logarithmic. The comparison has been done for the samples with 4 ML Ge coverage, grown at 600ºC (blue) and 730ºC (red), which are close in composition to simulated islands with pure Ge (dark blue) and a $Si_{0.5}Ge_{0.5}$ alloy structures (dark red).

The simulated pure Ge islands obviously exhibit the largest volume-averaged elastic energy (of about 5.5 meV/atom) [104,105]. This value iis not affected by the morphological asymmetry imposed by the island shape within the simulated miscut range. The experimental data for the islands grown at 600°C clearly show a lower average strain energy density with respect to the simulations with pure Ge content. This indicates a significant intermixing on both the flat and the misoriented substrates. What is indeed remarkable, in the experiment at 600°C, is that the volume averaged strain energy increases strongly for the 10° miscut domes, going from an approximately 1.4 meV/atom value for islands grown on flat surfaces to 2.9 meV/atom on the miscut substrate. Since FEM simulations indicate that this asymmetry is not a bulk effect, we believe that the appearance of miscut-induced facets has indeed a crucial role in the storing of elastic energy in the real (experimentally evaluated) system.

As expected, lower elastic energies are retrieved for the simulated islands with 50% Si content (about 1.1 meV/atom in Fig. 5.8), where again the miscut has no influence on the averaged energy if only bulk conditions are considered. These simulations can be compared to the volume-averaged anergies for the 730°C samples, where intermixing is more severe. Again, for the 4 ML domes grown at substrates with miscut, we measure a larger average elastic energy with respect to their counterparts grown on the flat substrate. Experimentally, we evaluate a strain energy of 0.22 meV/atom for the 0° miscut substrate, while 0.85 meV/atom for the 10° miscut sample. Again, we believe that the difference in elastic energy is stored at the asymmetric facets for the samples with 10° miscut.

The observed difference of elastic energy among islands on distinct substrates (vicinal and with miscut) are quite high if compared in their average values. Namely, the effect of an asymmetric faceting at large miscuts on the energetic balance is comparable to a change in stoichiometry of about 20 ~ 30 % in Si content. We speculate that both surface (kinetic) and bulk diffusion behave differently in assymetric domes. Surface diffusion may be affected by the distinct facet slope and surface reconstruction on the miscut domes, while bulk diffusion may be different for the islands shaped by the miscut due to the different height of the exposed surface (where the perpendicular stress is zero) with respect to the substrate/island interface, compared to the symmetric island shape on the flat substrate.

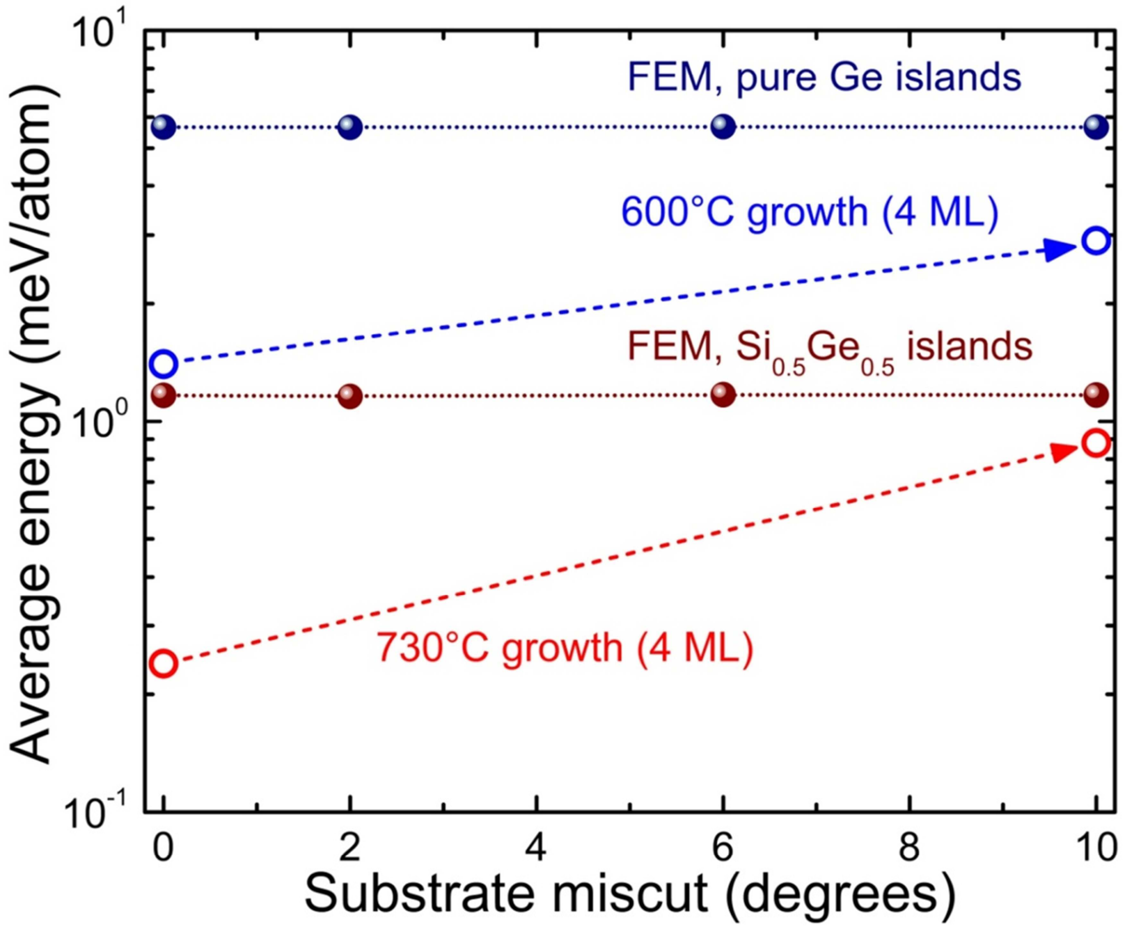

Fig 5.8 - Volume averaged energy (in meV/atom) for the structures simulated through FEM (dotted lines/solid dots) and obtained experimentally (dashed lines/open dots). Experimental results from samples with 4 ML Ge coverage grown at 600ºC (blue) and 730ºC (red) were compared with simulations assuming pure Ge islands (dark blue) and $Si_{0.5}Ge_{0.5}$ islands (dark red). The results point out to a larger elastic energy stored at the asymmetric facets for the samples with 10° miscut. Arrows connecting the experimental data serve as guide to the eyes only.

5.6 Conclusion

In conclusion, we have studied the intermixing inside SiGe islands grown on Si(001) substrates with and without miscut angle. Radial anomalous X-ray diffraction measurements were performed on samples containing 4 ML and 13 ML of Ge, grown under 600°C and 730°C. The Ge concentration and the elastic energy per atom stored during the nanostructures formation process, were retrieved. Previous studies on the flat Si(001) surface have shown that the Ge domes evolve into superdomes and during this transition process relax [106-110], but as far as we know this is the first time that the Ge concentration and the stored elastic energy is quantified for these structures. A comparison between FEM analysis of the structures, suited for bulk-like behavior, and the experimental data indicates that the different values obtained for the elastic energy probably arise due to a non trivial effect of the miscut-induced facets on substrates with large misorientation angles. Islands grown on large miscut substrates present higher values of volume-averaged elastic energy. A distinct local Si intermixing at the asymmetric islands may be responsible for such effect. Therefore, besides modifications on island morphology and density, the introduction of non-flat substrates allows to tune the elastic energy stored inside the Ge islands.

Chapter 6

Study of the strain field of $In_{0.5}Ga_{0.5}As$ islands grown on top of ultrathin GaAs nanomembrane

6.1 Motivation

In the last decade, semiconductor thin membranes gave rise to a promising field in nanotechnology, and have attracted great attention of the scientific community [111-122]. The possibility to transfer a few nanometers thick membrane to a new support opened up substantial potential applications in flexible eletronics and optoeletronics [123-125]. Nanomembranes (NMs) based on semiconductor materials with quantum dots (QDs) are strong candidates to play an important role in the next generation for the nanodevice industry [126,127]. The use of transferred NMs to piezoelectric host substrates, in order to tune embedded quantum emitters by straining the transferred membrane, has been recently reported [128,129]. A releasing process of the membrane generally affects its mechanical properties, leading for changes on optical and electronic features of interest [113,116,120,121,126,128,129]. In such scenario it is crucial to know the strain field on the NM, specially on the vicinity of the QDs, in order to determine the nanostructures new physical properties [114,115,124].

6.2 Samples and techniques

In this work we study $In_{0.5}Ga_{0.5}As$ islands on top of a 25 nm GaAs membrane. The islands were grown on top of the GaAs(001) ultrathin layer, an AlAs sacrificial layer and a GaAs buffer. A lateral view of a scheme of the sample is shown in figures 6.1(a) and 6.1(b). The GaAs layer, along with the islands, was released from the original substrate and transferred to a new host, a kapton foil. The NM was studied via X-ray diffraction (XRD) using a large (~500x700 μm^2, vertical x horizontal) and also a nano-focused (~200x500 nm^2, vertical x horizontal) beam, and the strain status was retrieved for both, an statistical group of islands and some isolated islands, and the results were compared, allowing the discussion about the quality of the structural properties of the NM.

The sample was grown by molecular-beam epitaxy (MBE). The growth conditions used here lead to the formation of islands with a density of 11 x 10^9 islands/cm^2 and an average size of 50 nm diameter and 12 nm height. The ultrathin GaAs layer with the islands was then released from the substrate [130,131]. An optical image of the sample can be seen in figure 6.1(c), evidencing the holes due to the etching process, which is depicted in figure 6.1(d).

X-ray diffraction experiments using a large beam were carried out upon transmission geometry, mapping the vicinity of the (400) and (220) GaAs reflection, at the XRD2 beamline of the Brazilian Synchrotron Light Laboratory (LNLS). The energy of the beam was fixed at 10.2 keV (corresponding to a wavelength of 1.2155 Å). The experiment used a Pilatus 100 K detector at 1.15 m from the sample.

Nano-diffraction experiments were also performed upon transmission geometry using a nano-focused X-ray beam at the ID01 beamline of the European Synchrotron Radiation Facility (ESRF), in Grenoble (France). The nano-beam was focused to a 200 x 500 nm^2 (vertical x horizontal) spot size using KB mirrors, and inciding on the sample upon transmission geometry. The energy of the beam was fixed at 8.388 keV (wavelength of 1.4781 Å) during the nano-diffraction experiments, allowing an incident flux in the order of 10^{10} photons/second. The diffracted beam was recorded with a two dimensional (2D) MAXIPIX photon-counting detector [132], with 516 x 516 pixels of 55 µm^2 pixel size, and positioned 0.95 m from the sample. The sample was mounted on a fast *xyz* scanning piezoelectric stage, with a lateral stroke of 100 µm and a resolution of 2 nm, and the piezo-stage was itself mounted on a hexapod. By simultaneously combining high-speed continuous motion of the *xyz* scanning piezoelectric stage with high frequency MAXIPIX image recording, the recently developed quicK continuous Mapping (K-Map) technique [133] allows two dimensional diffraction maps to be obtained extremely quick with respect to conventional X-ray micro- and nano-focusing diffraction experiments [134,135].

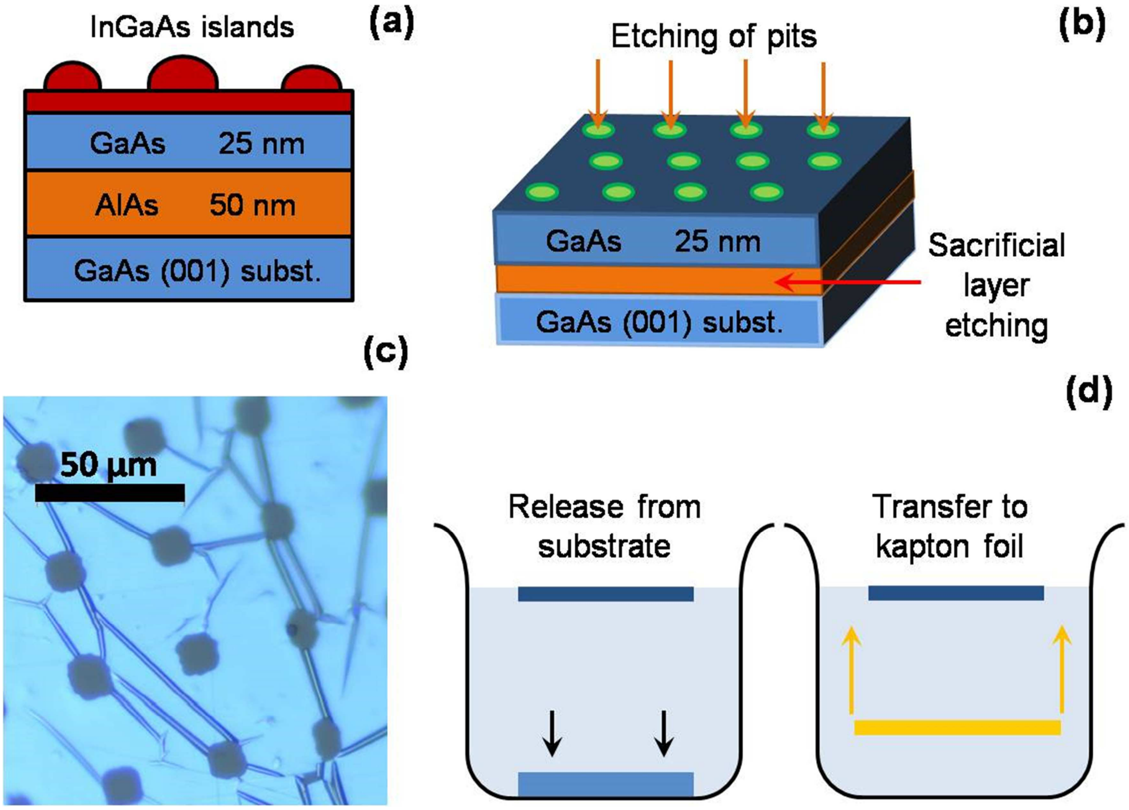

Fig 6.1 – (a) Lateral view of the scheme of the sample growth. (b) Perspective view showing the etching. (c) Optical image of the sample, evidencing the holes due to the etching process, which is depicted in (d).

6.3 Quick-mapping results

An image of the NM, obtained from the K-Map technique, is shown in figure 6.2(a), measured at the bulk (400)GaAs Bragg condition. The holes due to the etching process are easy to identify for such condition, since they follow the pattern of the mask used on the etching process, and have approximately 12 µm of diameter each. The very intense (red) regions on this image can be attributed to the flat, well aligned, membrane, which lattice parameter is close to the bulk GaAs value. Low intense lines can be seen all along the image, and their existence is assigned to the presence of rips and bends on the membrane. Finally, one can notice some intermediary intense dots spread throughout the image, which can be attributed to regions containing the $In_{0.5}Ga_{0.5}As$ islands, since a larger lattice parameter is expected for them when compared to the flat membrane. A K-Map scan were also performed for the islands Bragg condition, in order to confirm and emphasize the information concerning the islands, and the image obtained is shown in figure 6.2(b). The low intense (blue regions) now represent the areas where the membrane exhibits a lattice parameter that does not match with the islands Bragg condition, i.e. closer to the bulk GaAs value. Small dots, about 1~2 µm diameter can be seen spread all over the membrane, and their existence is attributed to isolated, or slightly disoriented, islands (and the halo of strained membrane around each of these structures). One can notice, however, big and very intense features, which can be attributed to very well oriented clusters of islands.

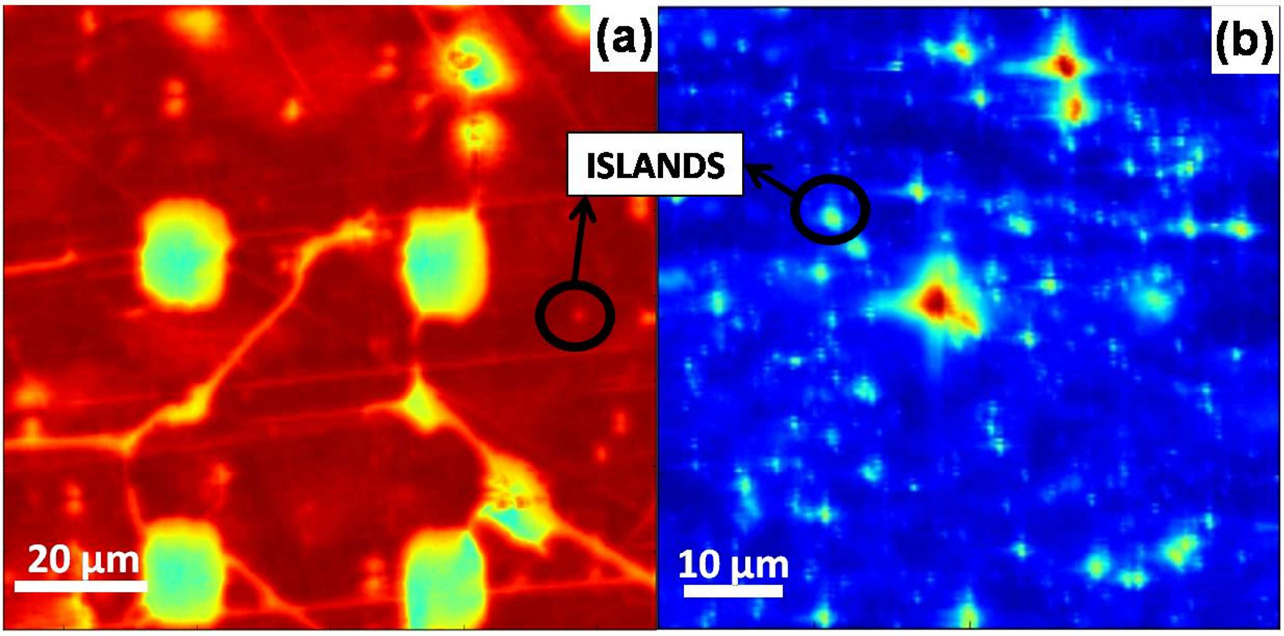

Fig 6.2 – (a) K-map on the GaAs Bragg condition, allowing the orientation of the beam in order to avoid de etching holes. (b) K-map on the InGaAs Bragg condition, evidencing the presence of the islands.

6.4 Discussion

In order to retrieve the overall strain status of the membrane, X-ray diffraction measurements were carried out upon transmission geometry. Longitudinal scans were performed near the (400) as well as the (220) GaAs reflections, and the results are shown in figure 6.3. An intense peak at the position corresponding to the bulk GaAs lattice parameter can be seen for both reflections, while a second peak centered at H=3.943 lattice parameter, which can be signed to the islands and its vicinities, appears in the figure 6.3(a) (400). However, one can see two peaks besides the (220)GaAs reflection, centered at H, K=1.872 and H, K=1.923, indicating that an in-plane anisotropy may takes place on the islands due to partial relaxation [136,137]. Distinct nucleation rates α (In-rich) and β (Ga-rich) dislocations in III-V semiconductors, which present a ratio of 2:1 for bulk configurations, may be responsible for the asymmetrical dislocations [138]. Previous studies on the effects of the substrate dislocations during lattice relaxation in InGaAs grown on (001)GaAs substrates reported anisotropy along the [110] direction [139,140]. The formation of dislocations in a given direction would drives a relaxation of the overall stress state of the islands through a preferential direction, resulting at the anisotropic relaxation of the islands [129].

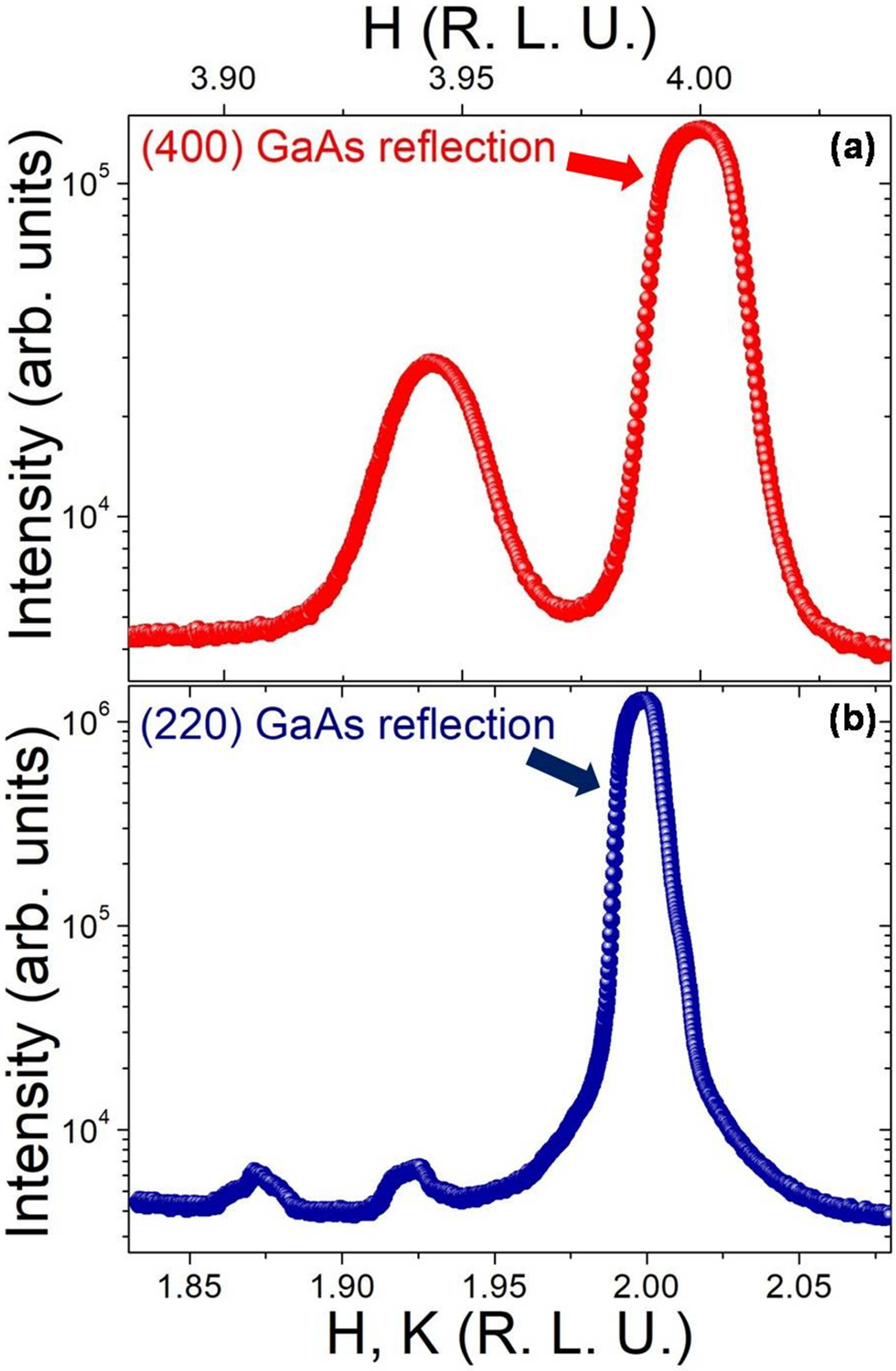

Fig 6.3 – X-ray diffraction measurements upon transmission geometry using a large beam near the (a) (400) and (b) (220) GaAs reflection.

Aiming for a better understanding of the observed effects, and to retrieve the strain status of some isolated islands, longitudinal scans on the vicinity of the same (400) and (220) GaAs reflections were performed using a nano-focused beam, and the results can be seen in figure 6.4. The diffraction intensity near the islands (400) Bragg peak, measured for two isolated islands, can be seen in figure 6.4(a), while the results for three other islands (not necessarily the same ones) are shown in figure 6.4(b) for the (220) reflection. The form of the peaks depend on the local strain status of the islands, but one can notice that the center of mass is overall the same for every island, i. e. the average in-plane lattice parameter does not suffer a significant change for different isolated islands, as seen for the (400) reflection. The scans for the (220) reflection present peaks at two different positions, corresponding to the two peaks obtained using the large beam, however, now one observes three different behaviors: i) scans with one peak centered at H, K=1.875, ii) scans with one peak centered at H, K=1.893, and iii) scans presenting both peaks. Such result indicates that more than one phase is observed for the sample, and the in-plane anisotropy, previously noticed using the large beam, cannot be seen for every island, but is a local phenomenon.

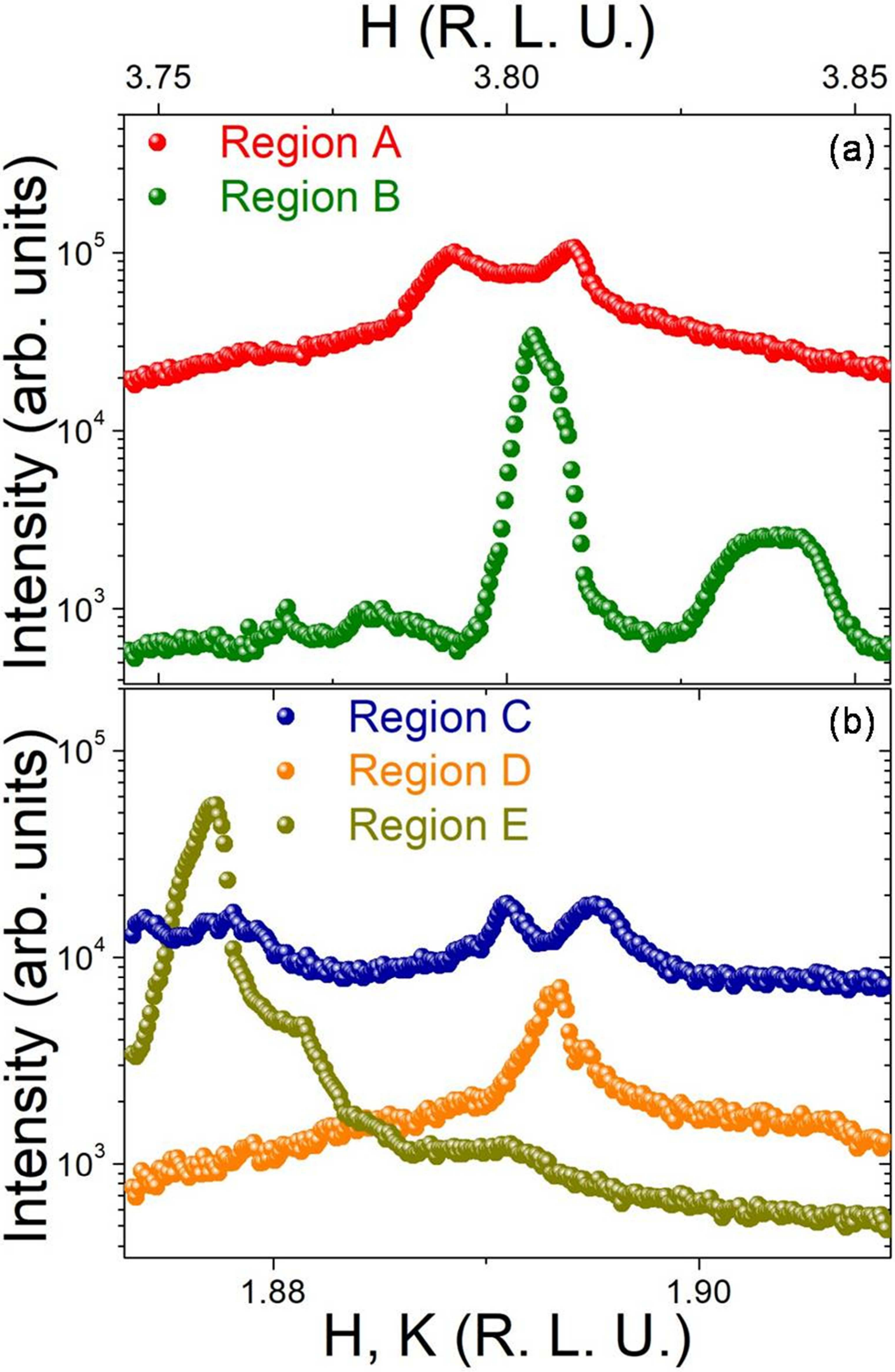

Fig 6.4 – X-ray nano-diffraction measurements upon transmission geometry, on different isolated islands, near the (a) (400) and (b) (220) GaAs reflection.

6.5 Conclusions and perspectives

The analysis of the K-map measurements points out for a crystalline high quality of the membrane, and a general homogeneous strain status, and also suggests the presence of some mosaicity. The comparison of the results coming from the diffraction and the nano-diffraction measurements, and the observation that peaks coming from the islands region are observed for two distinct Bragg conditions, indicate that an anisotropic relaxation process must occurs during the releasing process of the NM. As a perspective for this work, a local study of the tri-dimensional strain field, using coherent diffraction techniques, will be carried out and must clarify the anisotropic effect.

Final conclusions

Semiconductor nanostructures have been vastly studied during the last decades. The development of new techniques for both growth and characterization of promising samples allows the integration of these nanostructures on new devices and boosts the nanotechnology industry. This thesis presented X-ray diffraction techniques, and how it is possible to use synchrotron light sources to study semiconductor structures and determine mechanical and chemical properties, like the strain field and chemical composition. Finite elements simulation was used to collate the X-ray diffraction results, and assisted the data analysis, verifying structural configurations that cannot be directly observed.

Measurements near the Mn K absorption edge allowed a study about the Mn concentration on In(Mn)As islands grown on top of GaAs substrates. A comparison of the intensity of the scans corresponding to each energy determined, unambiguously, the amount of Mn atoms incorporated in all the possible sites. Results showed that for a low Mn relative deposition content the atoms are preferentially incorporated in the In interstitial sites, and the occupation of the In substitutional sites was only observed at, approximately, 35% nominal concentration threshold. Such result may be a consequence of the island surface potentials and Mn incorporation kinetic mechanisms, which can be favored by the strain relaxation at the In(Mn)As island surface.

Resonant X-ray diffraction was also used to study the intermixing inside SiGe islands grown on Si(001) substrates. Measurements near the Ge K absorption edge correlated the Ge concentration with the presence or absence of miscut on the substrate, for samples with 4 and 13 ML of Ge, and grown under 600ºC and 730ºC. The results indicated that the miscut hinders the intermixing for low Ge content (domes regime), but decreases the Ge concentration at the 13 ML samples (superdomes regime), while the temperature facilitates the intermixing. The elastic energy per atom could be retrieved from the previous results, and higher values were found for the samples with miscut. A FEM analysis indicated that the different values obtained for the elastic energy probably arise due to a non trivial effect of the miscut-induced facets on the samples with large miscut angles substrates. Distinct local Si intermixing at the asymmetric islands may be responsible for such effect. Therefore, the introduction of non-flat substrates allows to tune the elastic energy stored inside the Ge islands.

The use of nano-focused X-ray diffraction allowed a study of the local strain field on ultrathin GaAs membrane containing InGaAs islands. The quick mapping technique verified the crystalline quality of the membranes and suggested a mosaicity of the islands. Measuring isolated islands, and comparing with results coming from high statistical diffraction, it was possible to observe that an anisotropic relaxation process takes place during the NM releasing.

References

[1] J. Y. Tsao, *Materials Fundamentals of Molecular Beam Epitaxy*, Academic Press (London, 1993).

[2] Ângelo Malachias, Espalhamento de raios-X em ilhas auto-construídas de InAs, Master's thesis (2002).

[3] Zi-Bin Chen, Wen Lei, Bin Chen, Yan-Bo Wang, Xiao-Zhou Liao, Hoe H Tan, Jin Zou, Simon P Ringer, Chennupati Jagadish, Nanoscale Res. Lett., 7, 486 (2012).

[4] L. L. Chang, L. Esaki, W. E. Howard, R. Ludeke, G. Schul, J. Vac. Sci. Technol. 10, 655 (1973).

[5] J. Tersoff, F. K. LeGoues, Phys. Rev. Lett., 72, 3570 (1994).

[6] V. A. Shchukin, N. N. Ledentsov, D. Bimberg., *Epitaxy of Nanoestructures*, Springer Verlag (Berlin-Heildelberg, 2004).

[7] H. Lüth, *Surfaces and Interfaces of Solid Materials*, Springer Verlag (Berlin-Heildelberg, 1995).

[8] Y.Q. Wang, Z.L. Wang, J.J. Shen, A.S. Brown, Sol. State Commun., 122, 553 (2002).

[9] Vitaliy A. Shchukin, Dieter Bimberg, Rev. Mod. Phys., 71, 1125 (1999).

[10] Charles Kittel, Introduction to Solid State Physics, John Wiley and Sons (United States, 2005).

[11] Paul Harrison, Quantum Wells, Wires and Dots, John Wiley and Sons (United States, 2005).

[12] O. G. Schmidt, C. Lange, K. Eberl, Appl. Phys. Lett, 75, 13 (1999).

[13] A. Malachias, S. Kycia, G. Medeiros-Ribeiro, R. Magalhães-Paniago, T. I. Kamins, R. StanleyWilliams, Phys. Rev. Lett., 91, 17 (2003).

[14] Jens Als-Nielsen, Des McMorrow, Elements of Modern X-ray Physics, John Wiley and Sons (United States, 2011).

[15] T. H. Metzger, I.Kegel, R. Paniago, A. Lorke, J. Peisl, Thin Solid Films, 336, 1 (1998).

[16] I. Kegel, T. H. Metzger, A. Lorke, J. Peisl, J. Stangl, G. Bauer, K. Nordlund, W. V. Schoenfeld, P. M. Petroff, Phys. Rev. B 63, 035318 (2001).

[17] Itsuki Saito, Daiki Shimada, Mayu Aikawa, Tsukasa Miyazaki, Keisuke Shimokita, Hideaki Takagi, Katsuhiro Yamamoto, Polymer Journal 48, 399 (2016).

[18] Ângelo Malachias, X-ray Study of Strain, Composition, Elastic energy and Atomic ordering in Ge islands on Si(001), Ph.D’s thesis (2005).

[19] J.D. Jackson, Classical Electrodynamics (3rd ed.), John Wiley & Sons (United States, 1999).

[20] Yoshio Waseda, Anomalous X-ray Scattering for Materials Characterization, Springer-Verlag (Berlin Heidelberg, 2002).

[21] G. Chahine, M. I. Richard, A. Homs, T.-N. Tran-Caliste, D. Carbone, V. L. R. Jacques, R. Grifone, P. Boesecke, J. Katzer, I. Costina, H. Djazouli, T. Schroeder, T. U. Schülli, J. Appl. Cryst. 47, 762 (2014).

[22] Miao, Jianwei, Richard L. Sandberg, and Changyong Song. "Coherent X-ray diffraction imaging." Selected Topics in Quantum Electronics, IEEE Journal of 18.1 (2012): 399-410.

[23] J. Miao *et al.*, “Phase retrieval from the magnitude of the Fourier transforms of nonperiodic objects,” *J. Opt. Soc. Amer. A*, vol. 15, pp. 1662– 1669, 1998.

[24] J. R. Fienup, “Reconstruction of an object from the modulus of its Fourier transform,” *Opt. Lett*, vol. 3, pp. 27–29, 1978.

[25] J. R. Fienup, “Phase retrieval algorithms: a comparison,” *Appl. Opt.*, vol. 21, pp. 2758–2769, 1982.

[26] V. Elser, “Solution of the crystallographic phase problem by iterated projections,” *Acta Crystallogr. A*, vol. 59, pp. 201–209, 2003.

[27] C. C. Chen *et al.*, “Application of optimization technique to noncrystalline X-ray diffraction microscopy: Guided hybrid input–output method,” *Phys. Rev. B*, vol. 76, p. 064113, 2007.

[28] S. Marchesini, “A unified evaluation of iterative projection algorithms for phase retrieval,” *Rev. Sci. Instrum.*, vol. 78, p. 011301, 2007.

[29] H. H. Bauschke *et al.*, “Hybrid projection-reflection method for phase retrieval,” *J. Opt. Soc. Amer. A*, vol. 20, pp. 1025–1034, 2003.

[30] D. R. Luke, “Relaxed averaged alternating reflections for diffraction imaging,” *Inverse Problems*, vol. 21, pp. 37–50, 2005.

[31] D. Sayre, *Imaging Processes and Coherence in Physics*. (Springer Lecture Notes in Physics, vol. 112). New York, Berlin: Springer-Verlag, 1980, pp. 229–235.

[32] J. Miao *et al.*, “Extending the methodology of X-ray crystallography to allow imaging of micrometer-sized non-crystalline specimens,” *Nature*, vol. 400, pp. 342–344, 1999.

[33] H. Chapman and K. Nugent, Nature Photonics 4,833 (2010).

[34] M. Seibert et al., Nature, 470, 78 (2011).

[35] Williams, G. J., et al. "Fresnel coherent diffractive imaging." Physical Review Letters 97.2 (2006): 025506.

[36] Rodenburg, J. M., et al. "Hard-X-ray lensless imaging of extended objects." Physical review letters 98.3 (2007): 034801.

[37] G. K. Binnig, Phys. Scr., 19, 53 (1987).

[38] Rupali S Patil, Mangesh R Kokate, Chitra L Jambhale, Sambhaji M Pawar, Sung H Han, Sanjay S Kolekar, Adv. Nat. Sci.: Nanosci. Nanotechnol., 3, 015013 (2012).

[39] Robert Cook et al., *Concepts and Applications of Finite Element Analysis*, John Wiley & Sons (United States, 1989).

[40] Carlos A. Felippa, *Lecture Notes for the course Introduction to Finite Element Methods,* Aerospace Engineering Sciences Department of the University of Colorado (2004).

[41] H. Munekata, H. Ohno, S. Von Molnar, A. Segm̈ller, L. L. Chang, and L. Esaki, Phys. Rev. Lett. 63, 1849 (1989).

[42] H. Ohno, H. Munekata, T. Penney, S. Vonmolnar, and L. L. Chang, Phys. Rev. Lett. 68, 2664 (1992).

[43] S. Koshihara, a. Oiwa, M. Hirasawa, S. Katsumoto, Y. Iye, C. Urano, H. Takagi, and H. Munekata, Phys. Rev. Lett. 78, 4617 (1997).

[44] H. Akai, Phys. Rev. Lett. 81, 3002 (1998).

[45] J. Blinowski and P. Kacman, Phys. Rev. B 67, 121204 (2003).

[46] J. Mašek, J. Kudrnovský, and F. Máca, Phys. Rev. B 67, 153203 (2003).

[47] G. Sanders, Y. Sun, and F. Kyrychenko, Phys. Rev. B 68, 19 (2003).

[48] D. Chiba, Y. Sato, T. Kita, F. Matsukura, and H. Ohno, Phys. Rev. Lett. 93, 216602 (2004).

[49] J. Mašek and F. Máca, Phys. Rev. B 69, 165212 (2004).

[50] J. Sadowski and J. Z. Domagala, Phys. Rev. B 69, 75206 (2004).

[51] J. Wang, C. Sun, J. Kono, A. Oiwa, H. Munekata, A. Cywiński, and L. J. Sham, Phys. Rev. Lett. 95, 167401 (2005).

[52] G. A. Khodaparast, Y. H. Matsuda, D. Saha, G. D. Sanders, C. J. Stanton, H. Saito, S. Takeyama, T. R. Merritt, C. Feeser, B. W. Wessels, X. Liu, and J. Furdyna, Phys. Rev. B 88, 235204 (2013).

[53] A. H. MacDonald, P. Schiffer, and N. Samarth, Nat. Mater. 4, 195 (2005).

[54] O. V. Vikhrova, Y. A. Danilov, B. N. Zvonkov, A. V. Kudrin, V. V. Podol'Skiĭ, Y. N. Drozdov, M. V. Sapozhnikov, C. Moura, M. I. Vasilevskiy, and M. P. Temiryazeva, Phys. Solid State 50, 52 (2008).

[55] J. Novák, I. Vávra, Z. Križanová, S. Hasenöhrl, J. Šoltýs, M. Reiffers, and P. Štrichovanec, Appl. Surf. Sci. 256, 5672 (2010).

[56] J. A. Peters and B. W. Wessels, Phys. E 42, 1447 (2010).

[57] I. T. Yoon, S. Lee, Y. Shon, S. W. Lee, and T. W. Kang, J. Phys. Chem. Solids 72, 181 (2011).

[58] I. Kuryliszyn-Kudelska, J. Z. Domagala, T. Wojtowicz, X. Liu, E. Lusakowska, W. Dobrowolski, and J. K. Furdyna, J. Appl. Phys. 95, 26 (2003).

[59] V. Holý, X. Martí, L. Horák, O. Caha, V. Novák, M. Cukr, and T. U. Schülli, Appl. Phys. Lett. 97, 95 (2010).

[60] F. A. Ferri, L. N. Coelho, V. P. Kunets, G. J. Salamo, and E. Marega, J. Appl. Phys. 112, 34317 (2012).

[61] I. Frymark and G. Kowalski, J. Phys. D: Appl. Phys. 38, A160 (2005).

[62] L. Horák, Z. Sobáň, and V. Holý, J. Phys. Condens. Matter 22, 296009 (2010).

[63] P. Mahadevan and A. Zunger, Phys. Rev. B 68, 75202 (2003).

[64] K. M. Yu, W. Walukiewicz, T. Wojtowicz, I. Kuryliszyn, X. Liu, Y. Sasaki, and J. K. Furdyna, Phys. Rev. B 65, 212407 (2002).

[65] F. Máca and J. Mašek, Phys. Rev. B 65, 212407 (2002).

[66] M. Stoffel, A. Malachias, A. Rastelli, T. H. Metzger, O. G. Schmidt, Appl. Phys. Lett. 94, 253114 (2009).

[67] A. Malachias, M. Stoffel, M. Schmidbauer, T. Ü. Schulli, G. Medeiros-Ribeiro, O. G. Schmidt, R. Magalhães-paniago, and T. H. Metzger, Phys. Rev. B 82, 035307 (2010).

[68] M. Sztucki, T. U. Schülli, T. H. Metzger, E. Beham, D. Schuh and V. Chamard, Superlattices and Microstructures 36, 11 (2004).

[69] C. Lefevre, A. Thomasson, F. Roulland, V. Favre-Nicolin, Y. Joly, Y. Wakabayashi, G. Versini, S. Barre, C. Leuvrey, A. Demchenko, N. Boudet and N. Viart, J. Appl. Cryst. 49, 1308 (2016).

[70] J. Coraux, B. Amstatt, J. A. Budagoski, E. Bellet-Amalric, J. Rouvière, V. Favre-Nicolin, M. G. Proietti, H. Renevier, and B. Daudin, Phys. Rev. B 74, 195302 (2006).

[71] Letícia Coelho, Espalhamento ressonante de raios X aplicado ao estudo de nanoestruturas, Ph.D' s thesis (2008).

[72] P. Hohenberg, and W. Kohn, Phys. Rev., 136, B864 (1964).

[73] W. Kohn, and L. J. Sham, Phys. Rev., 140, A1133 (1965).

[74] J. M. Soler, E. Artacho, J. D. Gale, A. García, J. Junquera, P. Ordejón, and D. Sánchez-Portal, J. of Phys.:Cond. Matter 14, 2745 (2002).

[75] N. Troullier and J. L. Martins, Phys. Rev. B 43, 1993 (1991).

[76] L. Kleinman and D. M. Bylander, Phys. Rev. Lett. 48, 1425 (1982).

[77] Y. Zhang and W. Yang, Phys. Rev. Lett. 80, 890 (1998).

[78] J. T. Arantes, G. M. Dalpian, and A. Fazzio, Phys. Rev. B 78, 045402 (2008).

[79] M. Schmidbauer, Sh. Seydmohamadi, D. Grigoriev, Zh.M. Wang, Yu.I. Mazur, P. Schäfer, M. Hanke, R. Köhler, and G.J. Salamo, Controlling Planar and Vertical Ordering in Three-Dimensional (In,Ga)As Quantum Dot Lattices by GaAs Surface Orientation, Phys. Rev. Lett. 96 (2006) 066108-066108-4.

[80] O.G. Schmidt, N.Y. Jin-Phillipp, C. Lange, U. Denker, K. Eberl, R. Schreiner, H. Gräbeldinger, and H. Schweizer, Long-range ordered lines of self-assembled Ge islands on a flat Si (001) surface, Appl. Phys. Lett. 77 (2000) 4139-4141.

[81] G. Costantinia, A. Rastelli, C. Manzano, R. Songmuang, O.G. Schmidt, and K. Kern, Universal shapes of self-organized semiconductor quantum dots: Striking similarities between InAs⁄GaAs(001) and Ge⁄Si(001), Appl. Phys. Lett. 85 (2004) 5673-5675.

[82] L. Persichetti, A. Sgarlata, M. Fanfoni, and A. Balzarotti, Ripple-to-dome transition: The growth evolution of Ge on vicinal Si(1 1 10) surface, Phys. Rev. B 82 (2010) 121309-121309-4.

[83] L. Fazi, C. Hogan, L. Persichetti, C. Goletti, M. Palummo, A. Sgarlata, and A. Balzarotti, Intermixing and buried interfacial structure in strained Ge/Si(105) facets, Phys. Rev. B 88 (2013) 195312-195312-6.

[84] L. Persichetti, A. Sgarlata, G.Mattoni, M.Fanfoni, and A.Balzarotti, Orientational phase diagram of the epitaxially strained Si(001): Evidence of a singular (105) face, Phys. Rev. B 85 (2012) 195314-195314-6.

[85] L. Persichetti, A. Sgarlata, M. Fanfoni, and A. Balzarotti, Shaping Ge Islands on Si(001) Surfaces with Misorientation Angle, Phys. Rev. Lett. 104 (2010) 036104-036104-4.

[86] A. Sgarlata, L. Persichetti, A. Capasso, M. Fanfoni, N. Motta, and A. Balzarotti, Driving Ge island ordering on nanostructured Si surfaces, Nanoscience and Nanotechnology Lett. 3 (6) (2011) 841-849.

[87] L. Persichetti, A. Sgarlata, M. Fanfoni, and A. Balzarotti, Heteroepitaxy of Ge on singular and vicinal Si surfaces: elastic field symmetry and nanostructure growth, J. of Phys.: Condensed Matter 27 (2015) 253001-1-28.

[88] L. Persichetti, A. Sgarlata, M. Fanfoni, and A. Balzarotti, Pair interaction between Ge islands on vicinal Si(001) surfaces, Phys. Rev. B 81 (2010) 113409-113409-4.

[89] B. Yang, F. Liu, and M.G. Lagally, Local Strain-Mediated Chemical Potential Control of Quantum Dot Self-Organization in Heteroepitaxy, Phys. Rev. Lett. 92 (2004) 025502-025502-4.

[90] L.A.B. Marçal, B.L.T. Rosa, G.A.M. Safar, R.O. Freitas, O.G. Schmidt, P.S.S. Guimarães, Ch. Deneke and A. Malachias, Observation of Emission Enhancement Caused by Symmetric Carrier Depletion in III-V Nanomembrane Heterostructures, ACS Photonics 1 (2014) 863-870.

[91] L. Persichetti, R. Menditto, A. Sgarlata, M. Fanfoni, and A. Balzarotti, Hug-like island growth of Ge on strained vicinal Si(111) surfaces, Appl. Phys. Lett. 99 (2011) 161907-161907-3.

[92] J. Tersoff, C. Teichert, and M.G. Lagally, Self-Organization in Growth of Quantum Dot Superlattices, Phys. Rev. Lett. 76 (1996) 1675-1678.

[93] J. Stangl, V. Holý, and G. Bauer, Structural properties of self-organized semiconductor nanostructures, Rev. Mod. Phys. 76 (2004) 725-783.

[94] B. Voigtländer, Fundamental processes in Si/Si and Ge/Si epitaxy studied by scanning tunneling microscopy during growth, Surf. Sci. Rep. 43 (2001), 43, 127-254.

[95] I. Berbezier and A. Ronda, SiGe nanostructures, Surf. Sci. Rep. 64 (2009) 47-98.

[96] A. Vailionis, B. Cho, G. Glass, P. Desjardins, David G. Cahill, and J.E. Greene, Pathway for the Strain-Driven Two-Dimensional to Three-Dimensional Transition during Growth of Ge on Si(001), Phys. Rev. Lett. 85 (2000) 3672-3675.

[97] A. Rastelli, H. Von Känel, B.J. Spencer, and J. Tersoff, Prepyramid-to-pyramid transition of SiGe islands on Si(001), Phys. Rev. B 68 (2003) 115301-115301-6.

[98] J. Tersoff, B.J. Spencer, A. Rastelli, and H. von Känel, Barrierless Formation and Faceting of SiGe Islands on Si(001), Phys. Rev. Lett. 89 (2002) 196104-196104-4.

[99] L. Persichetti, A. Sgarlata, M. Fanfoni, and A. Balzarotti, Breaking Elastic Field Symmetry with Substrate Vicinality, Phys. Rev. Lett. 106 (2011) 055503-055503-4.

[100] A. Malachias, M. Stoffel, M. Schmidbauer, T. Schulli, G. Medeiros-Ribeiro, O.G. Schmidt, R. Magalhaes-Paniago, T.H. Metzger, Atomic ordering dependence on growth method in Ge:Si(001) islands: Influence of surface kinetic and thermodynamic interdiffusion mechanisms, Phys. Rev. B 82 (2010) 035307-035307-9.

[101] L.A.B. Marçal, M.S.C. Mazzoni, L.N. Coelho, E. Marega, G.J. Salamo, R. Magalhães-Paniago, and A. Malachias, Quantitative measurement of manganese incorporation into (In,Mn)As islands by resonant X-ray scattering, Phys. Rev. B 96 (2017) 245301-245301-7.

[102] A. Marzegalli, V.A. Zinovyev, F. Montalenti, A. Rastelli, M. Stoffel, T. Merdzhanova, O.G. Schmidt, and Leo Miglio, Critical Shape and Size for Dislocation Nucleation in $Si_{1-x}Ge_x$ Islands on Si(001), Phys. Rev. Lett. 99 (2007) 235505-235505-4.

[103] F. Montalenti, D. Scopece, and L. Miglio, One-dimensional Ge nanostructures on Si(001) and Si(1 1 10): Dominant role of surface energy, Comptes Rendus Physique 14 (7) (2013) 542-552.

[104] R. Magalhaes-Paniago, G. Medeiros-Ribeiro, A. Malachias, S. Kycia, T.I. Kamins, R. Stan Williams, Direct evaluation of composition profile, strain relaxation, and elastic energy of Ge:Si(001) self-assembled islands by anomalous X-ray scattering, Phys. Rev. B 66 (2002) 245312-245312-6.

[105] G. Medeiros-Ribeiro, A. Malachias, S. Kycia, R. Magalhães-Paniago, T.I. Kamins, R. Stanley Williams, Elastic energy mapping of epitaxial nanocrystals, Appl. Phys. A 80 (2005) 1211-1214.

[106] T.I. Kamins, G.M. Ribeiro, D.A.A. Ohlberg, and R.S. Williams, Evolution of Ge islands on Si(001) during annealing, J. Appl. Phys. 85 (1999) 1159-1171.

[107] A. Rastelli and H. von Känel, Surface evolution of faceted islands, Surf. Sci. 515 (2002) L493-L498.

[108] T. Merdzhanova, S. Kiravittaya, A. Rastelli, M. Stoffel, U. Denker, and O.G. Schmidt, Dendrochronology of Strain-Relaxed Islands, Phys. Rev. Lett. 96 (2006) 226103-226103-4.

[109] M.I. Richard, T.U. Schülli, G. Renaud, E. Wintersberger, G. Chen, G. Bauer, and V. Holý, In situ X-ray scattering study on the evolution of Ge island morphology and relaxation for low growth rate: Advanced transition to superdomes, Phys. Rev. B 80 (2009) 045313-045313-9.

[110] M.I. Richard, G. Chen, T.U. Schülli, G. Renaud, and G. Bauer, Coalescence of domes and superdomes at a low growth rate or during annealing: Towards the formation of flat-top superdomes, Surf. Sci. 602 (2008) 2157-2161.

[111] Rogers, J. A.; Lagally, M. G.; Nuzzo, R. G. Synthesis, assembly and applications of semiconductor nanomembranes. Nature, 477 (7362), 45 (2011).

[112] Rogers, J. A. Slice and dice, peel and stick: Emerging methods for nanostructure fabrication. ACS Nano, 1, 151 (2007).

[113] Scott, S. A.; Peng, W. N.; Kiefer, A. M.; Jiang, H. Q.; Knezevic, I.; Savage, D. E.; Eriksson, M. A.; Lagally, M. G. Influence of surface chemical modification on charge transport properties in ultrathin silicon membranes. ACS Nano, 3, 1683 (2009).

[114] Paskiewicz, D. M.; Tanto, B.; Savage, D. E.; Lagally, M. G. Defect-free single-crystal SiGe: A new material from nanomembrane strain engineering. ACS Nano, 5, 5814 (2011).

[115] Paskiewicz, D. M.; Scott, S. A.; Savage, D. E.; Celler, G. K.; Lagally, M. G. Symmetry in strain engineering of nanomembranes: Making new strained materials. ACS Nano, 5, 5532 (2011).

[116] Marçal, Lucas Atila Bernardes; Rosa, Barbara Luiza Teixeira; Safar, Gustavo A. M.; Freitas, Raul O.; Schmidt, Oliver G.; Guimarães, Paulo Sergio Soares; Deneke, Christoph; Malachias, Angelo. Observation of Emission Enhancement Caused by Symmetric Carrier Depletion in III-V Nanomembrane Heterostructures. ACS Photonics, 1, 863 (2014).

[117] Midolo, L.; Pregnolato, T.; Kiršanskė, G.; Stobbe, S. Soft-mask fabrication of gallium arsenide nanomembranes for integrated quantum photonics. Nanotechnology, 26, 484002 (2015).

[118] Cavallo, F.; Grierson, D. S.; Turner, K. T.; Lagally, M. G. “Soft Si”: Effective stiffness of supported crystalline nanomembranes. ACS Nano, 5, 5400 (2011).

[119] Rosa, B. L. T.; Marçal, L. A. B.; Andrade, R. R.; Pinto, L. D.; Rodrigues, W. N.; Souza, P. L.; Pires, M. P.; Nunes, R. W.; Malachias, A. Observation of partial relaxation mechanisms via anisotropic strain relief on epitaxial islands using semiconductor nanomembranes. Nanotechnology, 28, 305702 (2017).

[120] Chen, F.; Ramayya, E. B.; Euaruksakul, C.; Himpsel, F. J.; Celler, G. K.; Ding, B. J.; Knezevic, I.; Lagally, M. G. Quantum confinement, surface roughness, and the conduction band structure of ultrathin silicon membranes. ACS Nano, 4, 2466 (2010).

[121] Zaumseil, J.; Meitl, M. A.; Hsu, J. W. P.; Acharya, B. R.; Baldwin, K. W.; Loo, Y.-L.; Rogers, J. A. Three-dimensional and multilayer nanostructures formed by nanotransfer printing. Nano Lett., 3, 1223 (2003).

[122] Kim, D.-H.; Viventi, J.; Amsden, J. J.; Xiao, J.; Vigeland, L.; Kim, Y.-S.; Blanco, J. A.; Panilaitis, B.; Frechette, E. S.; Contreras, D.; Kaplan, D. L.; Omenetto, F. G.; Huang, Y.; Hwang, K.-C.; Zakin, M. R.; Litt, B.; Rogers, J. A. Dissolvable films of silk fibroin for ultrathin conformal biointegrated electronics. Nat. Mater., 9, 511 (2010).

[123] Choi, W. M.; Song, J.; Khang, D.-Y.; Jiang, H.; Huang, Y. Y.; Rogers, J. A. Biaxially stretchable “wavy” silicon nanomembranes. Nano Lett., 7, 1655 (2007).

[124] Kim, D.-H.; Rogers, J. A. Bend, buckle, and fold: Mechanical engineering with nanomembranes. ACS Nano, 3, 498 (2009).

[125] Hwang, S.-W.; Tao, H.; Kim, D.-H.; Cheng, H.; Song, J.-K.; Rill, E.; Brenckle, M. A.; Panilaitis, B.; Won, S. M.; Kim, Y.-S.; Song, Y. M.; Yu, K. J.; Ameen, A.; Li, R.; Su, Y.; Yang, M.; Kaplan, D. L.; Zakin, M. R.; Slepian, M. J.; Huang, Y.; Omenetto, F. G.; Rogers, J. A. A physically transient form of silicon electronics. Science, 337, 1640 (2012).

[126] Chanda, D.; Shigeta, K.; Gupta, S.; Cain, T.; Carlson, A.; Mihi, A.; Baca, A. J.; Bogart, G. R.; Braun, P.; Rogers, J. A. Large-area flexible 3D optical negative index metamaterial formed by nanotransfer printing. Nat. Nanotechnol., 6, 402 (2011).

[127] Malachias, A.; Mei, Y.; Annabattula, R. K.; Deneke, Ch.; Onck, P. R.; Schmidt, O. G. Wrinkled-up nanochannel networks: Long-range ordering, scalability, and X-ray investigation. ACS Nano, 2, 1715 (2008).

[128] Ding, F.; Singh, R.; Plumhof, J. D.; Zander, T.; Krapek, V.; Chen, Y. H.; Benyoucef, M.; Zwiller, V.; Dorr, K.; Bester, G.; Rastelli, A.; Schmidt, O. G. Tuning the exciton binding energies in single selfassembled InGaAs/GaAs quantum dots by piezoelectric-induced biaxial stress. Phys. Rev. Lett., 104, 067405 (2010).

[129] Rastelli, A.; Ding, F.; Plumhof, J. D.; Kumar, S.; Trotta, R.; Deneke, C.; Malachias, A.; Atkinson, P.; Zallo, E.; Zander, T.; et al. Controlling quantum dot emission by integration of semiconductor nanomembranes onto piezoelectric actuators. Phys. Status Solidi B, 249, 687 (2012).

[130] Cendula, P.; Malachias, A.; Deneke, Ch.; Kiravittaya, S.; Schmidt, O. G. Experimental realization of coexisting states of rolled-up and wrinkled nanomembranes by strain and etching control. Nanoscale, 6, 14326 (2014).

[131] Filipe Covre da Silva, S.; Lanzoni, E. M.; de Araujo Barboza, V.; Malachias, A.; Kiravittaya, S.; Deneke, Ch. InAs migration on released, wrinkled InGaAs membranes used as virtual substrate. Nanotechnology, 25, 455603 (2014).

[132] Ponchut, C.; Rigal, J. M.; Clement, J.; Papillon, E.; Homs, A.; Petitdemange, S. MAXIPIX, a fast readout photon-counting X-ray area detector for synchrotron applications. J. Instrum., 6, C01069 (2011).

[133] Chahine, G.; Richard, M. I.; Homs, A.; Tran-Caliste, T. -N.; Carbone, D.; Jacques, V. L. R; Grifone, R.; Boesecke, P.; Katzer, J.; Costina, I.; Djazouli, H.; Schroeder, T.; Schülli, T. U. Imaging of strain and lattice orientation by quick scanning X-ray microscopy combined with three-dimensional reciprocal space mapping. J. Appl. Cryst., 47, 762 (2014).

[134] Mocuta, C.; Stangl, J.; Mundboth, K.; Metzger, T. H.; Bauer, G.; Vartanyants, I. A.; Schmidbauer, M.; Boeck, T. Beyond the ensemble average: X-ray microdiffraction analysis of single SiGe islands. Phys. Rev. B, 77, 245425 (2008).

[135] Marçal, L. A. B.; Richard, M. -I.; Magalhães-Paniago, R.; Cavallo, F.; Lagally, M. G.; Schmidt, O. G.; Schülli, T. U.; Deneke, Ch.; Malachias, A. Direct evidence of strain transfer for InAs island growth on compliant Si substrates. Appl. Phys. Lett., 106, 151905 (2015).

[136] Owen, D. L.; Lackner, D.; Pitts, O. J.; Watkins, S. P.; Mooney, P. M. In-place bonding of GaAs/InGaAs/GaAs heterostructures to GaAs (001). Semicond. Sci. Technol, 24, 035011 (2009).

[137] Guo, W.; Mols, Y.; Belz, J.; Beyer, A.; Volz, K.; Schulze, A.; Langer, R.; Kunert, B. Anisotropic relaxation behavior of InGaAs/GaAs selectively grown in narrow trenches on (001) Si substrates. J. Appl. Phys., 122, 025303 (2017).

[138] Wang, L.; Li, M.; Xiong, M.; Zhao, L. Effect of interfacial bonds on the morphology of InAs QDs grown of GaAs (311) B and (100) substrates. Nanoscale Res. Lett., 4, 689 (2009).

[139] Barnett, S. J. *et al. In situ* X-ray topography studies during the molecular beam epitaxy growth of InGaAs on (001)GaAs: effects of substrate dislocation distribution on strain relaxation. J. Phys. D: Appl. Phys., 28, A17 (1995).

[140] Liu, X. W.; Hopgood, A. A.; Usher, B. F.; Wang, H.; Braithwaite, N. St. J. Formation of misfit dislocations during growth of $In_xGa_{1-x}As/GaAs$ strained-layer heterostructures. Semicond. Sci. Technol., 14, 1154 (1999).

List of publications

1. **Marçal, L. A. B.**, Rosa, B. L. T., Safar, G. A. M., Freitas, R. O., Schmidt, O. G., Guimarães, P. S. S., Deneke, Ch., Malachias, A. Observation of Emission Enhancement Caused by Symmetric Carrier Depletion in III-V Nanomembrane Heterostructures. ACS Photonics, **1**, 863 (2014).
2. Lopes-Oliveira, V., Mazur, Y. I., de Souza, L. D., **Marçal, L. A. B.**, WU, J., Teodoro, M. D., Malachias, A., Dorogan, V. G., Benemara, M., Tarasov, G. G., Marega, E., Marques, G. E., Wang, Z. M., Orlita, M., Salamo, G. J., Lopez-Richard, V. Structural and magnetic confinement of holes in the spin-polarized emission of coupled quantum ring-quantum dot chains. Physical Review B, **90**, 125315 (2014).
3. **Marçal, L. A. B.**, Richard, M.-I., Magalhães-Paniago, R., Cavallo, F., Lagally, M. G., Schmidt, O. G., Schülli, T. Ü., Deneke, Ch., Malachias, A. Direct evidence of strain transfer for InAs island growth on compliant Si substrates. Applied Physics Letters, **106**, 151905 (2015).
4. Barcelos, I. D., **Marçal, L. A. B.**, Deneke, Ch., Moura, L. G., Larceda, R. G., Malachias, A. Direct evaluation of CVD multilayer graphene elastic properties. RSC Advances: an international journal to further the chemical sciences, **6**, 103707 (2016).
5. Rosa, B. L. T., **Marçal, L. A. B.**, Andrade, R. R., Pinto, L. D., Rodrigues, W. N., Souza, P. L., Pires, M. P., Nunes, R. W., Malachias, A. Observation of partial relaxation mechanisms via anisotropic strain relief on epitaxial islands using semiconductor nanomembranes. Nanotechnology , **28**, 305702 (2017).
6. **Marçal, L. A. B.**, Mazzoni, M. S. C., Coelho, L. N., Marega, E., Salamo, G. J., Magalhães-Paniago, R., Malachias, A. Quantitative measurement of manganese incorporation into (In,Mn)As islands by resonant X-ray scattering. Physical Review B, **96**, 245301 (2017).

7. **Marçal, L. A. B.**, Richard, M.-I., Persichetti, L., Favre-Nicolin, V., Renevier, H., Fanfoni, M., Sgarlata, A., Schülli, T. U., Malachias, A. Modified strain and elastic energy behavior of Ge islands formed on high-miscut Si(001) substrates. – Applied Surface Science (2018). https://doi.org/10.1016/j.apsusc.2018.10.094